ISTANBUL TECHNICAL UNIVERSITY ★ GRADUATE SCHOOL OF SCIENCE ENGINEERING AND TECHNOLOGY

FLOW ANALYSIS IN WANKEL TYPE ROTARY ENGINE

M.Sc. THESIS

Amin FARZADI

Department of Mechanical Engineering

Automotive Program

MAY 2015

ISTANBUL TECHNICAL UNIVERSITY ★ GRADUATE SCHOOL OF SCIENCE ENGINEERING AND TECHNOLOGY

FLOW ANALYSIS IN WANKEL TYPE ROTARY ENGINE

M.Sc. THESIS

Amin FARZADI
(503121702)

Department of Mechanical Engineering

Automotive Program

Thesis Advisor: Dr. Osman Akın KUTLAR

MAY 2015

İSTANBUL TEKNİK ÜNİVERSİTESİ ★ FEN BİLİMLERİ ENSTİTÜSÜ

DÖNER PİSTONLU WANKEL MOTORUNDA HAVA AKIŞININ ANALİZİ

YÜKSEK LİSANS TEZİ

Amin FARZADI
(503121702)

Makine Mühendisliği Anabilim Dalı

Otomotiv

Tez Danışmanı: Dr. Osman Akın KUTLAR

MAYIS 2015

Amin Farzadi, a **M.Sc.** student of ITU **Graduate School of Science and Technology** student ID 503121702, successfully defended the **thesis** entitled "**Flow Analysis in Wankel Type Rotary Engine**", which he prepared after fulfilling the requirements specified in the associated legislations, before the jury whose signatures are below.

Thesis Advisor :	**Dr. Osman Akın KUTLAR** Istanbul Technical University	....
Jury Members :	**Dr. Levent Ali KAVURMACIOĞLU** Istanbul Technical University	....
	Dr. Özgür Oğuz TAŞKIRAN Turkish Naval Forces	....

Date of Submission : **4 May 2015**
Date of Defense : **29 May 2015**

To my parents, all that I have in whole of my life

FOREWORD

I would like to express my very great appreciation to my supervisor Dr.O.Akın KUTLAR. Without his helpful and constructive advices, this thesis would not have been possible. I would also like to thank Dr.L.KAVURMACIOĞLU, Dr.C. BAYKARA and Dr. Ö.TAŞKIRAN for their help and advices.
I also appreciate all the academic personnel specially the research assistants of the automotive department that always support me on any difficulties.
At last but not the least, I wish to appreciate my parents who have always supported and encouraged me on this way.

May 2015 Amin FARZADI
Mechanical Engineer

TABLE OF CONTENTS

Page

ABBREVIATIONS

aTDC	: After top dead center
Avg	: Average
bTDC	: Before top dead center
$\boldsymbol{\vartheta}$	: Characteristic kinetic viscosity
CFD	: Computational fluid dynamics
CI	: Compression ignition
CIDI	: Compression ignition direct injection
$\boldsymbol{c_p}$	: Constant pressure specific heat
$\boldsymbol{c_v}$	: Constant volume specific heat
CA	: Crank angle
$\boldsymbol{\rho}$	: Density
DISI	: Direct Injection Engine spark ignition
$\boldsymbol{\varepsilon}$	: Dissipation rate
e	: Eccentricity
GDI	: Gasoline Direct Injection
K	: Isentropic exponent
M	: Mach number
m	: Mass
$\boldsymbol{\dot{m}}$	: Mass flow rate
MDM	: Moving Dynamic Mesh
P	: Pressure
PDF	: Probability Density Function
r	: Radius
RNG	: Re-Normalisation Group method
Re	: Reynolds number
SI	: Spark ignition
c	: Speed of sound
t	: Time
$\Delta\boldsymbol{t}$	: Time step
TDC	: Top dead center
TKE	: Turbulence kinetic Energy
$\boldsymbol{\acute{u}}$	: Turbulent intensity
UDF	: User define function
V	: Volume

LIST OF TABLES

Page

LIST OF FIGURES

Page

FLOW ANALYSIS IN WANKEL TYPE ROTARY ENGINE

SUMMARY

Powerful, smooth, compact and light combined multi fuel capabilities are the main features of the rotary engines. The Wankel engine type of rotary engines has the best power-to-weight ratio and reliability make it suitable for automobile and other industry application. In comparison with reciprocating type engines, rotary engine is mechanically simple, has less vibration, and much more power to weight ratio so it could achieve much more performance at higher engine speed. On the other hand, lower fuel efficiency of rotary engines, while the gas prices increases, results in decreasing application of this engine types in automobile industries. This project seeks to introduce a way to increase fuel efficiency in rotary engines by improving the design parameters allowing it to be another efficient power source for automotive applications.

In order to design efficient rotary engine, it is necessary to have a good understanding of how engine design and operating parameters affect the engine performance. Due to complex designing process of Wankel rotary engine, it is expensive to experimentally study the effect of using different designed models on engine efficiency. Accurately designed computational analyses can reduce both the time and cost of producing the models by cutting the extra experimental tests.

Since the physics that taking place inside the Wankel engine chambers are complex, a simulation, which could solve the numerical models, is the necessity of this study. The main purpose of this computational study is to investigate the optimum design for the Wankel type rotary engine considering the fluid flow analysis inside it during the intake and compression cycles.

Computer programs developed for simulating the real conditions with the variety of adjustable and controllable values could be the good choice for this aim. For the aim of computational fluid dynamics (CFD) study, well-known ANSYS FLUENT software was used to model the rotary engine, which was designed in Solid works. FLUENT could simulate the flow field inside the combustion chamber of Wankel engine as a function of engine design and operating parameters. Meshing the geometry of the selected engine was done by using the ANSYS Meshing software. Studying the effect of rotary motion inside the engine on fluid flow, requires dynamic mesh motion so that the simulation could be done while the engine is working. By using the appropriate mesh motion methods, different models were studied to get the best results on fluid analysis. At last step, FLUENT could show the velocity paths and pressure distribution inside the Wankel engine.

For creating the engine model, many parameters have to be considered. Different methods used for creating the first model based on engine geometry. It was important to prepare a model that suits the best as real engine geometry without having any negative effect on engine working conditions especially on rotor edges. Design of the chamber contours of a rotary engine and the position of the pocket geometry also

studied and based on this design, the flow structure in each working chamber were calculated.
By considering the results of this study, it would be possible to estimate the temperature and pressure distribution inside the engine, especially for the critical geometric positions. Since our models had no combustion inside, the results were somehow differed from experimental works.
By comparing the first non-CFD model with the latest models simulated by FLUENT, the effect of rotor apex sealing could be seen. Decreasing this effect is one of the main issues in modeling the Wankel engine.
Different geometric models, effect the results obtained from this analysis. For the models with wider recess height or symmetric design recess models, we get much more symmetric distribution than other models.
Since this study was done on two-dimensional model, the compression ratio of the model differed from the real engine, and this could effected the results in comparison with the 3D studies.
In future works, simulating this model in 3D and changing the four-stroke Wankel engine to two-stroke with side port intake and exhaust, will be done.

DÖNER PİSTONLU WANKEL MOTORUNDA HAVA AKIŞININ ANALİZİ

ÖZET

Normal pistonlu motorlara göre birim hacimden alınan güç, titreşimsiz çalışma, montaj kolaylığı ve farklı yakıtların kullanılabilmesi döner pistonlu motorların öne çıkan en önemli özelliklerindir.

Dönen pistonlu motorların en bilinenlerinden olan Wankel motoru, ağırlığına göre güç çıktısının daha iyi olması ve güvenilirliği onu otomobil ve diğer endüstri alanlarında uygulanabilir kılmaktadır. Wankel motoru daha sık kullanılan eksenel pistonlu motorlara göre mekanik olarak daha basit olması, daha az titreşimli çalışması ve güç ağırlık oranının daha fazla olması yönünden öne çıkmaktadır, böylece yüksek devirlerde çalışmaktadır. Diğer yandan düşük yakıt ekonomisi artan yakıt fiyatlarıyla ve sıkılaşan emisyon standartlarıyla paralel olarak bu motorların otomotiv endüstrisindeki kullanımını düşürmüştür.

Bu tezin amacı tasarım parametreleriyle oynayarak yakıt tüketimini düşürmek ve bu motoru otomotiv endüstrisinde daha verimli bir şekilde kullanmak için yeni bir yol bulmaktır.

Döner piston krank mili (yani eksantrik) özerinde döner burada krank mili bir nokta yani merkeze göre dairesel hareketle dönmesine karşılık üzerinde hareket eden döner piston bir eşkenar üçgen olmasına rağmen silindir içinde eliptik bir hareket şekli ile döner.

Wankel motorları çalışma prensibi bakımından pistonlu motorlara göre farklılık gösterir. Motor üzerinde hareketli parça olarak rotor ve ekzantrik mil bulunmaktadır. Emme ve egzoz zamanlarında pistonlu motorlar gibi subap tertibatı bulunmamaktadır. Emme ve egzoz süreci, gövde veya yan gövdelerde bulunan portlar sayesinde gerçekleştirilir. Portların açılma ve kapanma zamanları ise rotorun hareketi ile yan yüzü sınırlamaktadır. Portlar aracılığı ile dolgu değişimi sağlanmaktadır. Aynı zamanda portun geometrisi avansı belirlemektedir.

Wankel motorlarda daha önce bahsedildiği gibi birim hacimden elde edilen güç yoğunluğu daha yüksektir. Klasik pistonlu motorlarda krank milinin iki tam devri sonucu bir çevrim tamamlanırken (720° KMA), Wankel motoru eksantrik milin her bir turunda bir çevrim tamamlamaktadır (360° EMA). Bu nedenle Wankel motorunda güç yoğunluğu iki zamanlı klasik pistonlu motora eşdeğerdir.

Motorun sızdırmazlık ve yağlama problemleri nedeniyle kullanımı fazla yaygınlaşmamasına rağmen, motoru kullanmaya devam eden alanlar mevcuttur. Havacılık sektöründe, özellikle insansız hava araçlarında, güç/ağırlık oranı yüksek tahrik sistemleri gerekmektedir. Ağırlığın düşük olması, uzun süre havada kalacak araç için, yakıt tüketimi açısından avantaj sağlamaktadır. Aynı zamanda gücün yüksek olması arzulanan bir durumdur. Otomotiv sektöründe de geçmiş yıllarda ve günümüzde bazı firmalar Wankel motoru bulunan taşıtlar üretmişlerdir. Günümüzde karayolu araçlarının hibrit araç teknolojilerinin içinde de Wankel motoruna yer verilmektedir. Elektrikli araçlarda, akü şarjı aşamasında kullanılan Wankel motorunun en önemli avantajı, aküler nedeniyle ortaya çıkan ağırlığın, ufak kütleli Wankel motorları tarafından tolere edilmesidir. Böylece elektrikli aracın aküye dayalı menzili, ağırlık artışına rağmen yüksek seviyede tutulmaktadır.

Verimli bir döner pistonlu motor tasarlamak için, motorun çalışma ve tasarım parametrelerinin motor performansını nasıl etkilediğini iyi anlamak gerekir. İçten yanmalı motorları yapısı gereği, yapılan deneysel çalışmalar çok maliyetli olmakta ve çok zaman almaktadır. Dolayısıyla gerçeğe yakın olarak tasarlanmış bilgisayar analizleri, zaman ve maliyetten kazandırmakta ve fazladan yapılabilecek deneylerin önüne geçmektedir.
Motoru yanma odası içerisinde gelişen fiziksel olaylar karmaşık olduğundan, bu çalışmada da oluşturulan modelin çözülebilmesi zahmetli olmuştur. Bu çalışmanın asıl amacı Wankel tipi döner pistonlu motorun emme ve sıkıştırma periyotu boyunca akış analizin gerçekleştirilerek, optimum dizaynın oluşturulmasıdır.
Bilgisayar programları bahsedilen bu işlerin gerçek şartlara uygunluğu göz önünde bulundurularak ve parametrelerin kolayca kontrol edilip ayarlanabilir olması nedeniyle bu tez çalışmasında kullanılmıştır. Bu amaçal kulanılan hesaplamalı akışkanlar dinamiği (CFD) programı gerek akademi çevrelerince, gerkse de endüstride sıklıkla kullanınlan ANSYS FLUENT programıdır.
FLUENT programında analizi yapılacak model SOLIDWORK programında tasarlanmış ve FLUENT'e aktarılmıştır. FLUENT yanma odası ve manifoldlardaki akış alanını, motor dizayn ve çalışma parametrelerinin fonksiyonu olarak analiz etmektedir.
Motorun akış alanı analizi pistonun zamanla dönüşünün izlenebildiği dinamik hücre yapısıyla gerçekleştirilmiştir. Uygun hücre yapısı methodları kullanılarak en iyi sonuç için farklı modeller üzerine çalışılmıştır. Son adımda FLUENT ile akış alanındaki hız vektörleri ve basınç dağılımları görülmüştür.
En uygun modeli yaratmak için bir çok parametre göz önünde bulundurulmuş, farklı methodlar kullanılmıştır. Oluşturulan modelin motor çalışma koşullarında ve özellikle rotor kenarlarında herhangi bir negatif etki yaratmayacak şekilde gerçek motoru temsil eden en iyi model olmasına özellikle dikkat edilmiştir. Aynı şekilde yanma odası sınırları ve paket geometrinin rotor uzerındekı pozisyonu, her çalışma odasındaki akış yapısı model üzerinde hassas bir şekilde oluşturulmuş hesaplanmıştır.
Tez çalışması kapsamında elde edilen veriler değerlendirildiğinde, farklı devirlerde basınç-sıcaklık dağılımı, türbülans dağılımı incelenmiştir. Bu dağılımlar yanma odası içerisinde hangi bölgelerde nasıl eğilim gösterdiği araştırılmıştır. Yapılan model çalışmasında gerçek motor şartlarındaki gibi bir yanmanın olmadığı sadece havanın motor içersinde ne tür bir davranış sergilediğine bakıldığı için elde edilen sonuçlar motorun çalışma şartlarını yansıtmaz. Fakat yapılan çalışmadaki model ve geometriye bakılarak bahsi geçen dağılımlar incelenerek gerçek motor şartları için fikir oluşturmaktadır.
Yürütülen çalışmada kullandığımız ilk metoda göre elde edilen sonuçların simülasyon sonuçları ile kıyaslandığında, rotorun gövdenin trokoid yüzey ile temas eden yerlerde kaçakların daha fazla olduğu görülmektedir. Gerçek motor şartlarına baktığımızda, motor yüksek devirlerde çalıştığı için uç segman trokoid yüzey arasında zamanla aşınma ve özellikle uç segmanların sızdırmazlığı tam olarak sağlayamadığı için komşu odalara kaçak olmaktadır. Bu durum Wankel motorları için bir dezavantajdır.
Farklı geometriler farklı modeller ile incelendiğinde, dağılımın yanma odası içersinde farklı sonuçlar göstermektedir. Kullandığımız modellerde, yanma odası oyuğunun daha derin olması oda içerisinde oluşan dağılımların daha simetrik hale

gelmesi sonucu çıkmıştır. Simetrik olmayan yanma odası oyuklarında ise dağılımlar simetrik bir şekilde gerçekleşmiştir. Elde edilen veriler gerçek motor çalışmasına da etki edeceği düşünülmektedir.
Yapılan çalışmanın 2 boyutlu olması nedeniyle yanma odası üç boyutlu olarak da çizilebilir. Wankel motor için yapılan model çalışmaları 3 boyutlu olduğundan yanma odası oyuğu rotor yüzeyinin ortasında yer alır. Oyuğun farklı olması demek motorun sıkıştırma oranının değişmesine ve sonuç olarak performansını da etkisi olmakla birlikte oyuktaki bu değişim yapılan model çalışmalarını tesir etmektedir.
Bu çalışmanın devamı olarak aynı modelin 3 boyutlu şekilde yapılması ile başlanabilir. Bir sonraki adımda Wankel motorunu iki zamanlı hale getirip bunun üzerine bir model çalışması yapılabilir.
Wankel motorunun daha verimli ve yakıt sarfiyatının daha az olması için araştırma ve geliştirme çalışmalarına devam edilerek model çalışmaları ile bir iyileştirme sağlanmalıdır.

1. INTRODUCTION

Doing research for any topic, requires the background knowledge of that topic. What has done before on the topic and the ways that experienced before for solving the issues, may help the research to get the better results. In this part, we will have a review at Wankel engine topic and the works done on this topic before us.

1.1 History

Rotary engines have a history that dates back as 1588, when Italian inventor Agostino Ramelli invented a rotary piston type water pump [1]. Almost two hundred years later in 1759, James Watt invented the first steam-powered rotary engine.

As the next step after inventing the conventional combustion engine, finding a way for saving both weight and energy consumption by changing the reciprocating action of typical piston engine to directly rotary motion was first suggested by a German inventor Felix Wankel, in 1920s. His first patent for rotary engine was granted in 1936. Between the years 1940s until 1950s, he made his effort to improve the design, when he began collaboration with German automotive and motorcycle manufacturer NSU, where Wankel rotary engine model was first developed for being useable in vehicles.

Before Dr. Wankel had conceived his idea for use in internal combustion application, he firstly used the rotary concept at NSU for a compression system. In 1951, his rotary compressor model was used as a supercharger for one of the motorcycles model, which could record break land speed record. Early Wankel engine called ``Drehkolbenmaschine" (DKM) in which the rotation housing and rotor move around a fixed central shaft, designed in 1954 and its first experimental study was done in 1957 with V_h= 250 cm^3 and 17000 rpm. It was remarkably smooth in operation, and could run at fantastic speeds. It has the problem of disassembling required for changing spark plugs. So the ``Kreiskolbenmotor" (KKM) was developed by Dr.W. FRODE in 1957 and its first experimental study was done in 1958 with V_h= 125 cm^3

and 8000 rpm. In the KKM, the rotor and output shaft rotate inside a fixed housing and the park plugs are easily accessible on the housing ports. Intake and exhaust process was done by ports on the housing, similar in principle to a two-stroke piston engine.

In Britain, Norton Motorcycles developed a Wankel rotary engine for motorcycles, which was included in their Commander; Suzuki also produced a production motorcycle with a Wankel engine, the RE-5. John Deere Inc., in the US, had a major research effort in rotary engines and designed a version, which was capable of using a variety of fuels without changing the engine.

After occasional use in automobiles, for instance by NSU with their RO-80 model, Citroen used the M35 and GS engines produced by Comotor. In addition, there are extensive attempts by General Motors and Mercedes Benz to design Wankel engine automobiles. The most extensive automotive use of the Wankel engine has been done by the Japanese company Mazda. After years of development, Mazda's first Wankel engine car- Mazda Cosmo was introduced in 1967. However, they had the very bad luck of being released in the middle of efforts to decrease emissions and increase fuel economy. However, the company continued using the Wankel rotary engine in their RX-7 sports car until 2002.

In the racing world, Mazda has had substantial success with two-rotor, three-rotor, and four rotor cars, and private racers have also had considerable success with stock and modified Mazda Wankel-engine cars. The refined Mazda HR-X is a concept car that runs on pure, renewable hydrogen**,** and emits primarily only water vapor. Mazda engineers have improved the performance and fuel efficiency of this engine, since its original debut in 1991. After many years of development, Mazda re-launched the rotary engine called RENESIS with the new RX-8 sports car. RENESIS was selected as "The international engine of the year 2003" and met EURO-4 emissions. The Mazda vehicle showed that hydrogen also could be safely use as a fuel with very high engine performance [2].

In order to realize fully these attractive features of the Wankel rotary engine, it is necessary to have a good understanding of how engine design and operating parameters affect the unsteady, multidimensional fluid flow, fuel-air mixing process, and combustion inside the engine's combustion chambers.

1.2 Wankel Rotary Engine

The Wankel rotary engine has many advantages make it suitable for automobile applications. The higher power-to-weight ratio and larger power output in higher speed conditions, parallel with its simple and compact geometry due to fewer moving parts, and also multi-fuel capability and lower noise and vibration due to non-reciprocating parts, all are the highlight points make Wankel engine as a suitable choice.

On the other hand, Wankel engine has some problems in using liquid fuels. The long and narrow combustion chamber makes the flame not to reach to far ends of combustion chamber. Also, low flame speed and as a result, high quenching distance of liquid fuels, i.e. gasoline and diesel, prevent the flame from reaching the narrow distances at rotor ends during the combustion stroke. These reasons made the Wankel engines to have high fuel consumption and hydrocarbon pollutant emissions.

1.3 Wankel Rotary Engine Application

The higher power-to-weight ratio and reliability make the Wankel engine not only suitable for automobile industries, but also well suited to aircraft engine uses. There was an interest in Wankel engine in the 1950s when the first design was becoming well known, but it was simultaneous with the time that all industries was moving to jet engines. The Wankel suffered from lack of interest, but its application for small aircraft has continued [3]. A typical compact two-rotor engine using in small aircraft shown in Fig.1.1.

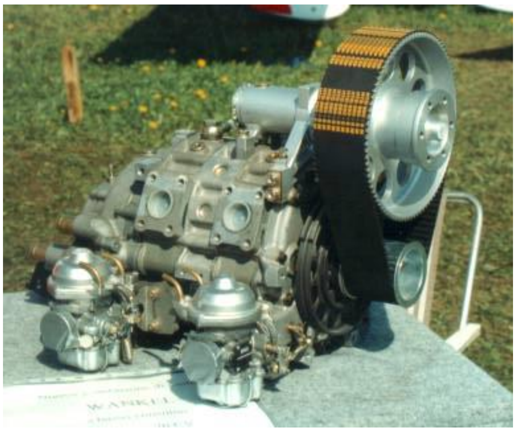

Figure 1.1 : Four strokes Wankel aircraft engine built in Canada.

Using the Wankel engine is not limited to automotive industries and could be used as a replacement for reciprocating engines in motorcycle, bouts and small power generation units.

The simplicity and less number of parts using in it makes is ideal for mini and micro engine designs. The Micro Electro Mechanical Systems (MEMS) Rotary Engine Lab at the University of California at Berkeley has been developing Wankel engines approximately the size of an American penny (4-5 mm in diameter), displacing 0.0775 cc.

The largest Wankel engine was produced by Ingersoll-Rand which has 550 horsepower with just one rotor available also in two rotor models. Its displacement was 41 liters per rotor with one-meter diameter of rotor. This model was available between 1975 and 1985.

1.4 Main Advantages of Rotary Engines

Wankel engines having a wide range of benefits specially in comparison with reciprocating conventional engines make it to become more useful. Following is some of these advantages [4,5,26].

Wankel engines, having simpler design and containing less moving parts make them smaller in size, so less construction costs compared to piston engines with the same power output [7,8].

- There are no valves and its complex valve train, which makes the engine simpler and lighter and leads to less friction in comparison with reciprocating engines especially in high speed ranges [9].
- There are no reciprocating parts such as connecting rods and conventional crankshaft. The rotor geared directly to output shaft that results in smoother and lighter engine with 100% balanced condition.
- The output shaft rotates 3 times faster than an engine rotor, so the working time of each stroke is 1.5 times slower than the reciprocating engine. This means higher performance at higher speeds.
- Multi fuel capability as a reason of separate combustion region is another advantage. The separation of combustion chamber from intake region prevents forming the localized hot spots.

- Higher power to weight ratio is also another benefit of using Wankel engine. Rotary engine makes high power for its size because of its high volumetric efficiency.
- The output power of rotary engine transferred with eccentric output shaft, so there is extremely low torque oscillation and vibration.
- Rotary engine has an intrinsic resistance to knocking due to its large surface to volume ratio, and rotation of the combustion chamber [10].

1.5 Disadvantages of Rotary Engines

Although the Wankel rotary engine has many advantages, there are some disadvantages for this kind of engine.

- Large heat transfer area due to its large surface area of chambers, which extract heat from the combustion. Good insulation for the housing and the rotor results in reducing the waste energy or cooling loss. It also helps to increase the thermal efficiency, which measures the rate of fuel consumption in the engine [11]. Heat losses reduce the thermal efficiency relative to ideal theoretical thermal efficiency. By reducing cooling loss, it is also possible to increase the burning speed. Increased burning speed can reduce the friction loss and increase power output [12].
- The rotary engine requires advanced sealing mechanisms and difficult sealing of the engine parts. Three-dimensional sealing of the rotor makes its efficiency less than reciprocating engine in high heat degrees and peak pressure points. Not only the apex sealing is required, but also it is required from chamber ends. The contact surface of apex seals and the housing is not a fixed angle while the rotor rotates. It is always changing between plus or minus 25 degree to both sides of the apex seals.
- High emissions due to burned gases carried into the combustion chamber during the overlap of exhaust and intake cycle. Also because of sweeping movement of the rotary engine, injected fuel near the edges collected where the flame front does not reach.

R&D in this area could solve these disadvantages as they explained.

1.6 Basic Operation of Rotary Engine

The Wankel rotary engine is an internal combustion (IC) engine that performs the four strokes of an Otto cycle (i.e. intake, compression, expansion, and exhaust) by the rotating of a trochoidal rotor inside an epitrochoid-shaped housing.

After the diesel, the Otto cycle is perhaps the most commonly used process in automotive and industrial engines to create internal combustion power. This cycle was first invented by Nikolaus Otto in 1876 and subjects four distinct process phases to air/fuel mixture to produce power [13].

Figure 1.2a shows the starting point of the rotor for the counter-clockwise motion. Then we can see the maximum volume during the intake process for the side 7 in figure 1.2c. Figure 1.2b shows the position in which the chamber between rotor and housing for side 5 is least, called the top dead center or TDC. We can see the maximum volume for side 3 during the exhaust in figure 1.2a. Sides 1, 4 and 7 show he intake stroke and 10, 2 and 5 show the compression stroke. At last, the exhaust stroke can be seen as sides 3, 6 and 9.

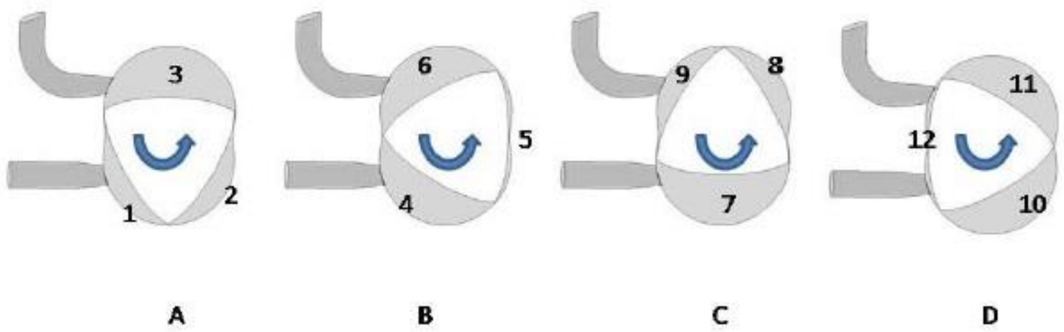

Figure 1.2 : Basic rotary positions.

The four main cycles of rotary engine are intake, compression, expansion and exhaust. Mixture of the fuel and air which is mixed outside of the rotary chamber, injected into it via intake port. Then this mixture compressed during the rotary motion of the rotor inside the combustion chamber. By using spark plug right after TDC, the pressurized air-fuel mixture ignites. For using the diesel fuels, ignition should be change because of the lower ignition delay time [10,14]. In these models, fuel directly injected into the working chamber [15].

The expansion stroke is essentially the power stroke, which is using for getting the output power.

Gear ratio between the output shaft and the rotor is 3:1, which means that when the rotor rotates one complete cycle, the output shaft rotates three cycles. Every cycle of the rotor contains twelve strokes. Since there is only one combustion on every forth stroke, for one cycle of output shaft rotation there is only one combustion process. By 270 degree of the output shaft crank angles, one complete stroke happens while in reciprocating engines it is 180 degree needed for one stroke. Therefore, a rotary stroke is 1.5 times longer than a reciprocating engine stroke. This is one of the reasons that rotary engine tends to breath well. It has more time to induct air and exhaust spent gasses. It has also more time to harness energy during the expansion phase [13].

Another main difference between the reciprocating engine and rotary engine is the way that they achieve output power from engine. Although for both of them the combustion inside combustion chamber is the main power source, the method they achieve this power is somehow different. The rotary engine does not have any connecting rod and the crankshaft directly gets its rotation by rotor rotation due to power created from combustion inside the chamber, as shown in figure bellow. The thick red arrow represent the line of action of the resultant force acting through the center of the rotor, causing the output shaft to rotate counter clockwise [16]. Figure 1.3 shows the main port and direction of the rotor rotation.

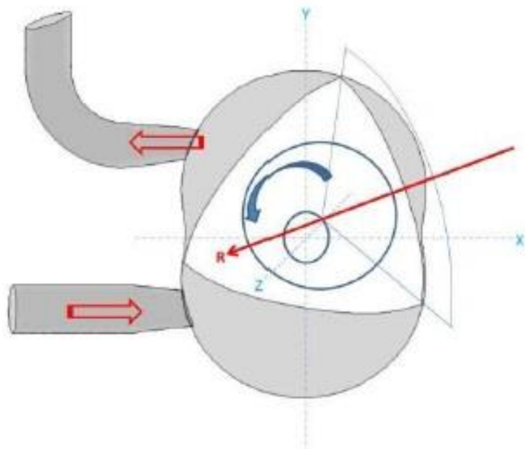

Figure 1.3 : Forces applied to the output shaft.

1.7 Rotary Engine Main Parts

Rotary engines do not have pistons and valves that move up and down. Instead, the rotor turns in steady, continuous motion that does not have to overcome inertia due to change in direction or speed. It takes energy to start and stop the pistons as they reach the top and bottom of each stroke. Instead of valves that open and close, the rotary engine has ports that are covered and uncovered by turning rotor itself [13].

1.7.1 Engine housing

The housing part of the rotary engine has two side parts with the inner epitrochoid edge profile. This is functionally similar to cylinder block and cylinder in normal engines. The housing profile designed in such a way that the rotor will always stay in contact with the wall of the chamber, forming three sealed volume. Figure 1.4 shows the main housing parts.

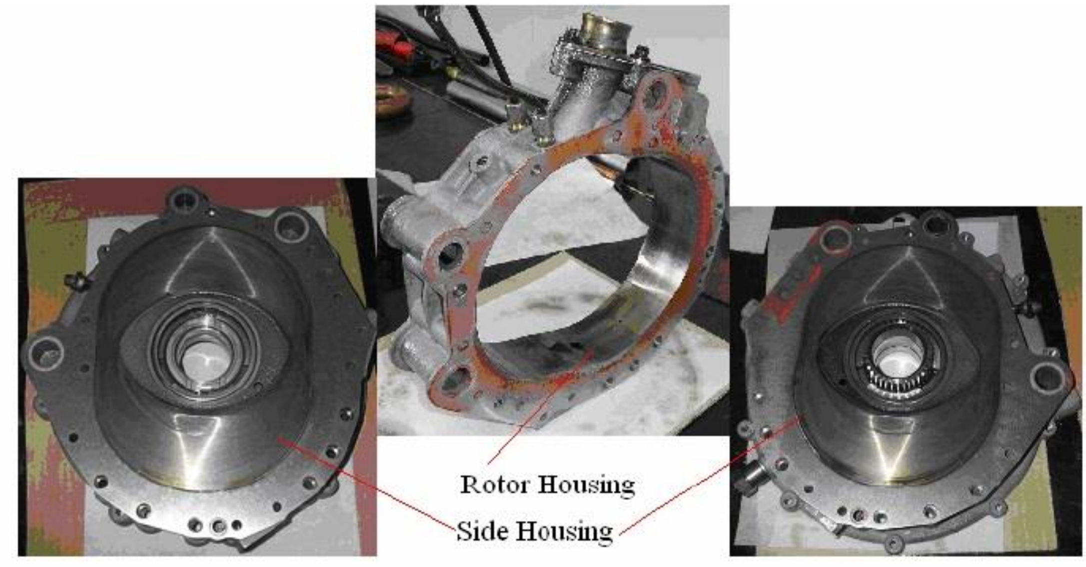

Figure 1.4 : Rotor housing and side housing of the engine block.

Main bearing of the output shaft is fitted to both side of housing. One of the side housing is fitted with rotor fixed gear. The cooling jacket and intake/exhaust ports are shaped in the housing.

The inner profile of the housing for the epitrochoid is expressed by the (x,y) coordinates seen on equation below:

$$\begin{cases} x = e\cos\alpha + (R+a)\cos\beta \\ y = e\sin\alpha + (R+a)\sin\beta \end{cases} \quad \textbf{(1.1)}$$

Where e is the eccentricity, R is the generating radius and a is the amount of parallel transfer.

1.7.2 Engine rotor

The rotor roughly equivalent to the piston in rotary engine and it is the primary moving part in rotary engine. In Mazda engines, the rotor is constructed from cast iron and is formed in the side shape of a 3-flanked hypotrochoid. The triangular rotor has the same “diameter” when measured from one side of it to the other and through the center of the rotor. The rotor is mounted on a bearing to an offset journal of an eccentric shaft, which is somewhat analogous to the crankshaft in a piston engine. As the eccentric shaft rotates about its longitudinal rotation axis, the rotor is forced to move in small circle by way of this offset journal. This movement is called the “orbit” of the rotor [13].

As it shown in figure 1.5, each face of the rotor may have a pocket (recess) in it, which increases the displacement of the engine, and allow more space for air/fuel mixture. Figure below shows a typical engine rotor.

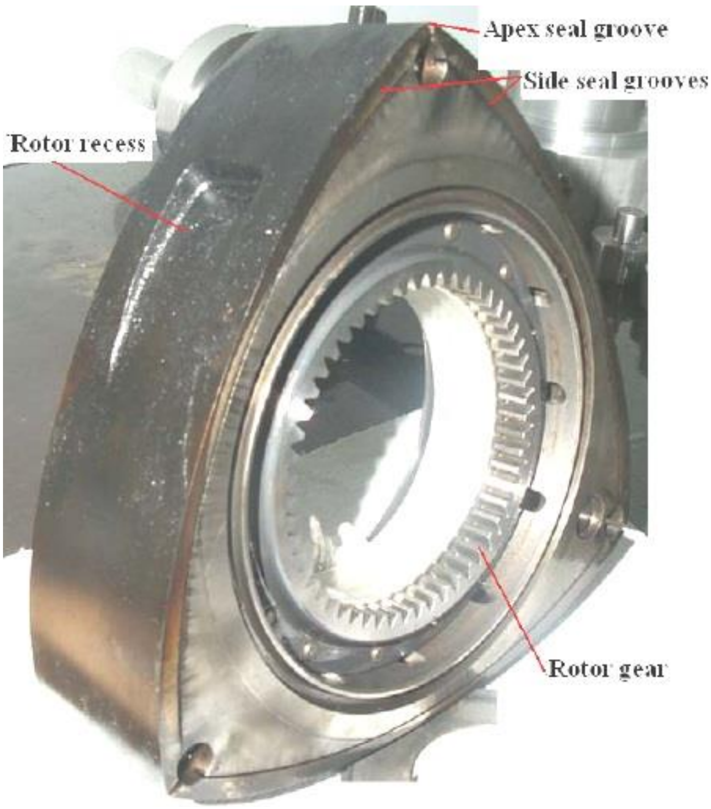

Figure 1.5 : Rotor with recess.

A groove shaped on the rotor apex is for inserting the apex sealing, which separates the three faces from each other. There is also another groove shape on the rotor side to insert the side seals preventing any side leakage. In addition to rotor´s functionality that acts like a piston, it is also working as an intake/exhaust valve when it is rotating.

The rotor is connected to output shaft eccentric part by the gears, applying the force, which comes from gas expansion and as the result, the output shaft rotate.

The equation, which generates the coordinates of the points of rotor outer edge, will be explained in chapter 4.

1.7.3 Output shaft:

The output shaft in rotary engine as shown in figure 1.6 is similar to crankshaft of the piston engine and they both have the same functionality. It generates the rotating motion by the force of combustion pressure applied on rotor journal eccentric to the center of the rotation. The output shaft rotates three times faster than the rotor. A flywheel and V-belt pulley is fitted to shafts ends.

Figure 1.6 : Engine output shaft.

1.7.4 Gears:

The rotor of the rotary engine forced to spin about its own centroid axis. This movement caused by large gear that is attached to inner diameter of the rotor. This is called the phasing gear, which is meshes with a smaller, outward-facing stationary gear that is affixed to the side housing of the engine. The stationary gear has exactly two thirds (2/3) the number teeth as the phasing gear. As the eccentric shaft rotates and the rotor begins orbiting, it is also simultaneously forced to spin about its own axis by the action of these gears. The combined motion of the rotor spins and orbit result in planetary motion of the rotor.

1.8 Literature Review

As the first works on this area, according to Sierens et al. [18], Wolter (1978) measured the gas velocities inside the combustion chamber by using an electric discharge system in rotary engine while the rotor was fixed and the housing rotates around it. The details of the intake and internal flows in general are not independent of which body is rotating and which one is stationary.

Hicks et al. [19] worked on flow patterns during intake and early compression, obtained by holographic interferometry, and stated that the primary purpose of their experiments had to been to demonstrate its viability. On the other hand, by hot wire anemometry Semenov had already established that in conventional engines turbulence near TDC is rather homogeneous and isotropic in the absence of squish, and varies linearly with engine speed [20].

In early seventies, a one-dimensional model of combustion in premixed-charge rotary engines was introduced [21]. Another interesting early modeling effort is that of Danieli et al. [22] which states the importance of gas leakage by the seals. Shin et al. [23] presented the first two dimensional computations of flow in rotary engine while the same work for the reciprocating engines was first published in 1975 [24].

F. Grasso, F.V. Bracco amd J.Abraham published their study named "three-dimensional computations of flows in a stratified-charge rotary engine" in 1987 [25]. Their model was three-dimensional rotary engine includes k-ε sub model for turbulence. The model was made up of the general conservation equations for two-phase reactive flows. A two-equation k-ε (turbulence kinetic energy – rate of dissipation of turbulence kinetic energy) sub model was used. The boundary condition for k and ε at walls were k=9 and equilibrium between generation and dissipation of turbulence. They use KIVA code [26], which was first developed, at Los Alamos National Laboratory to solve the unsteady 3-D Navier-Stokes equations for multi species reacting two-phase flows and reset for their work named REC-3D-FSC-8686 (Rotary Engine Combustion, 3-Dimensional, Flows, Sprays and Combustion, 1986 version). Both the rotor by circular arc and the housing generates by epitrochoid are divided in intervals that unequally spaced. The corresponding nodes on rotor and housing profile joined together by line. The coordinate system employed was fixed to the housing. The position of the grid nodes were re-evaluated at each time step to made the volume change due to rotor motion. The spatial differencing was based on a finite volume approach by mean value theorem, Gauss theorem and midpoint rule are used to evaluate numerically volume and surface integrals.

However, in the presence of highly skewed cells, like what happened in rotary engine, the accuracy of the numerical solution is reduced. Computational efficiency was improved by using a dynamic rezoning algorithm to remove cells in the X plane, when the cell aspect ratio falls below a certain value, and then add them back when the aspect ratio is greater than a certain value. The grid rezoning was done according to one-dimensional volume averaged Interpolation. Intake gas temperature was 300 K. As the result of their study, in rotary engines the spatial distribution of turbulence is always highly non-uniform around TDC, primarily because of squish. Also in rotary engines, near TDC, turbulence is always insensitive to the details of the turbulence generated during intake, but may depend on the initial turbulence diffusivity.

In 1988, A computer program was developed by T.Shih and H.J.Schok for studying the unsteady three dimensional flow field inside the combustion chamber of Wankel engine considering the engine design and operating conditions [27]. They present the numerical solution, which shows the velocity fields inside the engine and also mixing of nonhomogeneous fuel air mixture. In their study, the rotor pocket extends from one side housing to the other side and they assume no leakage across the apex seals exist. Therefore, they could assume that studying the only one chamber is enough since the others are the same. They use air as residual gas in combustion chamber at the pressure of P=1.5 bars and at the temperature of T=1000 K. The gas that enters the combustion chamber is either air or gaseous fuel-air mixture with the 1.2 bar pressure and 300 k temperature. For all the exhaust, intake, compression and expansion processes, the temperature for the rotor, housing, side housing and seal surfaces assumed constant. The governing equations consist of the conservation equation of mass, species, momentum and total energy. They use the numerical methods for solving the PDE equations. By using the Grid system and time levels for their finite-difference method, they could replace the continuous spatial domain by a system of grid points and duration of interests by time level. Using the minimum grid points increase the efficiency of computational modeling. The grid system that used could be move and deform with the combustion chamber movement. By using this method, they could see the fluid flow path inside the chamber. During the exhaust process, the residual gas rushes out from combustion chamber through the exhaust port due to higher pressure that is inside the combustion chamber in comparison with backpressure of exhaust port. While the both exhaust and intake ports are open, the charge rushes into the combustion chamber and the residual gases exit through exhaust port. The flow pattern between the intake and exhaust port, formed by momentum induced by rotor movement and the pressure difference between intake and exhaust ports achieved.

Comparisons of computed and measured mean velocity and turbulence intensity in a rotary engine was done by J.Abraham and F.V.Bracco, published for the first time in 1988 [28]. The computational part was done with three-dimensional model and the measurements were made at Sandia National laboratories at different locations along the rotor housing. Computed and measured chamber pressures were compared over wide range of operation conditions and they were within 12% of each other. For comparable conditions, the turbulent diffusivity around top dead center in rotary engine tends to be lower than reciprocating engine due to much more time between intakes until TDC. All the measurements were obtained by laser Doppler velocimetry (LDV). The computational model solves the general conservation equation for two-phase reactive flow. For turbulence, a two-equation k-ε sub model is used. The computational started at intake, continued on one complete cycle, and proceed through the second intake up to TDC. Boundary condition for the ε-equations is obtained by assuming that dissipation and production of kinetic energy of turbulence are equal near the wall. The measurement of the gas velocity obtained through quartz windows located near intake region. Pressure transducers were located in the housing and in the intake and exhaust manifolds. Computed mean velocities compared with measured mean velocities while computed turbulence intensities compared with measured fluctuation intensities since the origin of the difference is in the definition of turbulence. The mean velocity for measurements which achieved by simple ensemble averaging technique, and the ensemble-average of bulk velocities tend to be the same. However, the fluctuation intensity is always larger than the turbulence intensity. In any case even before the measurements, the computed mean velocity would agree with the mean velocity but the computed turbulence intensity would be smaller than the measured fluctuation intensity at least some 30%. In addition, the turbulence intensity tends to be rather homogeneous and of similar magnitude before and after TDC but significantly inhomogeneous and greater magnitude around TDC.

In year 1990, F.hamady, T. Stuecken and H.Schok worked on Airflow visualization by LDV method in motored rotary engine [29]. In their first part of publications, flow visualization was done at normal and supercharged conditions during the intake and compression strokes. They record the light scattered off the particles by high-speed camera at 5000 frames per second. The helium gas was injected with the entrained air to the single rotor peripherally ported like a Mazda 12A model so that the fringe patterns could be recorded which could allow the density variation measurement of the flow. Velocity measurement was done using laser Doppler velocimetry and optical access was provided by fabricating sapphire windows in the end housing part. Pressure results from static and dynamic tests showed the same result achieved in the central housing part with or without the Plexiglas window. The high-speed flow visualization system consists of 40-watt copper vapor laser (CVL) and the camera to electronically synchronize timing system with mirrors, lenses and particle generator. The CVL emits short pulses at rate of 4000-6000 pulse per second.

The result of this study on two different conditions with and without supercharge, indicated that the fluid is entrained by velocity field generated by the rotor toward the rotor pocket. In the intake process, the level of vorticity generated in the supercharged engine was higher than that in normal engine. In addition, the flow into the intake port at the end of the intake stroke is reduced in super charged engine. The major flow features of their study were separation at the rotor pocket, large recirculation region during intake and leakage past the apex seal. It was also concluded that the rotor motion has the controlling effect on the turbulent flow field during the intake and compression strokes.

In another research which was done by Z.Li , E. Steinthorsson and T.Shih in 1990, the numerical study on Wankel engine flow fields by using the turbulence model published [30]. They used two different turbulence models, k- Epsilon model with wall function and low Reynolds number k-Epsilon model, with several variations of numerical methods to calculate the turbulent flow field inside one combustion chamber.

Four variations of the first order upwind differences, second order upwind differencing, first order upwind differencing with Newton-Raphson iteration at each time step, and second order upwind differencing with Newton-Raphson iteration at each time selected. The conservation equation was ensemble averaged by using the Favre averaging in order to facilitate analysis. The standard k-Epsilon model is not valid in the buffer or the linear sublayer of the turbulent boundary layer because of the local low Reynolds number. By using the low Reynolds model of Chen and Patel [31], it was easier to implement numerically and required less grid points than the normal low Reynolds number model because that model does not solve the PDE for EPSILON in the wall region. The numerical method used was an implicit finite-difference method with time linearization approximate factorization. For the comparison between first order upwind or second order, the first order upwind differencing was more robust than the second order. This could be solved by adding the Newton-Raphson iteration for the second order upwind method.

Another result of their study was adding a sufficient number of grid points and using the standard k-EPSILON model with wall function in the boundary layer for simulating the recirculating flow on the right hand side of the intake jet while using the second order upwind differencing method. The turbulent flow field at TDC is dominated by the compression process and only influenced by the intake and exhaust process.

3-D Computations to improve combustion in Rotary engine was done by J.Abraham and F.V.Bracco with collaborating of P.Epstein to study geometry effects for modified geometries in continuous of their first work in 1987 [32]. They studied a three-dimensional model of direct injection rotary engine with two modifications to the pocket geometry of the engine. In one the pocket geometry was located towards the leading edge, shows the produce recirculation within the pocket and faster burning, and in another one two pocket with two injectors and two spark plugs studied. They also use the general conservation equations for two-phase flows with sub models for turbulence, heat and momentum fluxes. The gas phase equations are solved numerically by means of a fully implicit finite-volume method. In their study, two significant feature of fluid field of standard engine are low turbulence levels near top center especially within the pocket, and unidirectional flow of gas with negligible recirculation. As the result, mixing and combustion are slow and unburned fuel remained through expansion and exhaust strokes. The translation of the entire pocket itself toward the leading edge results in recirculation. In standard engine, there is an unfavorable pressure gradient which opposes the motion of the rotor as higher pressure are generally found on the back part and lower pressure on leading part. In standard pocket model, neither recirculation nor a significant increase in turbulence diffusivity is observed within the pocket as TC is approached. The lowest values for turbulence and diffusivity are within the pocket where injection and combustion occur.

In leading pocket, due to pocket placement relocation, relative timing of the events such as injection, vaporization, mixing and combustion occurs. Moving the pocket toward the trailing edge would delay the events and moving it toward leading edge would advance the events. The greater the trailing flanks area, the greater the effect of the squish in the pocket happens. The effect of placement of two pockets with two injectors and two spark plugs, results in better utilization of the air in the chamber and in high efficiency.

In year 2013, another study done by D.Jeng, C.Lee and Yu Han on the numerical investigation on the performance of rotary engine with leakage, different fuels and recess sizes [33]. The commercial CFD software FLUENT was used to simulate two dimensional models for air and fuel. Three different apex seal clearance studied with two different types of fuel CH4 and C8H18 and three different compression ratios. They use porous region modeling on small gap for simplifying rotor mesh construction. This could greatly reduce mesh size and stabilize the numerical iterations [33].

The main assumptions of their study was infinite width of the rotor, transient and periodic flow with compressible gas, No slip on wall boundaries and neglecting the effect of gravity and magnetic. Two-dimensional Favre Averaged Navier-Stokes equations and the energy equation were used to simulate the transient flow in rotary engine. Species conservation equation also used for calculating the species mass fractions. Standard k-Epsilon model was applied to calculate the turbulent flow in the chamber. All the mentioned equations were discretized with the finite volume method. The second upwind scheme was used to obtain the flux for all cells. The scheme PISO was also used for pressure velocity coupling. Unstructured mesh was used to discretize the computational domain of irregular shape of the rotor and housing profile. This mesh was adjusted by cutting and merging in accordance with the volume variation of the working chamber to simulate the rotor movement. They use a small porous region in place of gaps between rotor edge tips and housing profile to reduce the computational time. The effect of leakage on apex seal clearance was presented by calculating the flow field of porous region. This modification leads to less mesh number near clearance and making the numerical computation more stable. As the result, even at the end of compression process, there is no significant difference between pressure distributions with different clearance. The highest temperature occurred in the exhaust chamber and the area of high temperature extended with the increasing clearance size. Also at the condition that combustion happens inside the chamber, there is no obvious difference between the temperature distribution plots with different clearances. No obvious flow structure difference was found between the flow fields with the three sizes of recess. The higher pressure and temperature levels were obtained at higher compression ratio. With leakage, the high-pressure fluid in the combustion chamber went through the seal clearance into the neighbor compression chamber, and that led the flame moving toward the compression chamber. Better fuel/air mixing was reacted due to extended burning area. There was also an obvious difference between the predicted and the measured chamber pressure with close compression ratios.

1.9 Literature Review on CFD

Increases in the power of computer hardware, while the decreasing of hardware costs, and high costs of engineering experiments, have allowed CFD programs to be developed and applied to almost all the fields of engineering with the ability for simulation of the flow physics and heat transfer while saving the time and costs.

The main advantages of CFD over the experimental analysis are reduced time and cost, the ability of simulation and analyzing critical conditions and the experimentally difficult systems, unlimited optimization models and results and quickly identify the most promising design candidates for further development.

However, CFD will never replace theoretical or experimental approach and only could help to interpret and understand the results of theory and experiment.

Early modeling of the rotary engine based on thermodynamic models [34] and one-dimensional modeling of premixed-charge combustion.

Using the computer programs for the Wankel engine studies refers to years 1987. Computer programs based on multidimensional analysis developed by Shih et al and Grasso et al. [27] named as UF-LRC-2D. It was intended for studying the fluid flow inside two-dimensional Wankel engines under motored conditions. This program works based on conservation equation of mass, species, momentum and total energy.

The computer program developed by Grasso et al named REC-3D-FSC-86 was intended for studying three-dimensional flow fields based on KIVA computer program developed at Los Alamos National Laboratory. It generated solutions to the governing equations by using a conditionally stable implicit-explicit numerical method.

Further computations performed by Abraham and Bracco [35,36], led to some important design changes in the rotary engine development at Deere and co., especially in the fuel injector configuration. Their code, REC-3D-FSC-86, is a modified version of KIVA code developed at Los Alamos National laboratory [37], which was written for the modeling of reciprocating engines. KIVA makes use of a conditionally stable logarithm, the stability of KIVA scheme is improved by making use of an acoustic sub-cycling step in order to alleviate the stiffness problems arising from compressibility effects. They concluded that non-uniformity of mixing of fuel and air is attributed to the large fluid acceleration caused by the motion of the rotor. There appears to be a considerable room for improvement in the code, since it neglects the spatial gradients whenever the grid spacing becomes smaller than some predefined value and requires excessive CPU time when engine speed becomes small.

In another research, Abraham and Bracco [38], with concentration on ignition strategies in stratified charge RE engine, concluded that the use of two spark plugs would increase the engine efficiency by 7-10%. In addition, they find that the modification of the rotor pocket located towards the leading edge of the rotor would produce re-circulation results in faster fuel combustion, leads to better engine efficiency.

Shih et al. [39], presented the earliest two-dimensional computations of a motored Wankel engine in the absence of combustion. Their code, LEWIS-2D, is based on the beam-warming type of alternating-direction implicit (ADI) method. Their computations were later extended to three-dimensions in Steinthorsson et al. [40]. Linear stability analysis has shown that the ADI method is unconditionally stable in two-dimensions but it is unstable in three-dimensions. Li et al. , modified their LEWIS-3D code based on upwind schemes together with the incorporation of a k-ϵ turbulence model for better stability.

Raju et al. [41], on his study sponsored by NASA has developed a new computer code to analyze the chemically reactive flow and spray combustion processes occurring inside a stratified-charge rotary engine. They presented their results at limited operating conditions for code validation process. Typical results include, pressure and temperature, torque generated by the non-uniform pressure distribution within the chamber, energy release rates and various flow related phenomenon were reported and compared with other predictions. They concluded that the non-uniform pressure is higher near the trailing apex region than the leading apex region and mostly the rotor-induced fluid motion determines it.

The code appears to be potentially efficient compared with other schemes used in modeling Wankel engines, even its turbulence model needs to be improved.

Izweik [42], used the commercial code, AVL FIRE, to investigate the effects of recess shape on the flow fields in rotary engine.

In 2004, Padmarajan et al. [43], at Cranfield University and with the help of FLUENT-6.1 dynamic mesh, have developed a new 2-D model of rotated Wankel engine. The 2-D model simulating the three combustion chambers on the rotor faces with no combustion. The aim of this work is to study the flow fields inside the combustion chambers and to detect the rotor apex leakage between the chambers. The inlet and outlet ports were not simulated, and their effects were not reported.

Lack of experimental results reported by the authors, limited this work to be validated.

In addition, simulating the rotary engine without inlet port, omitting the inlet flow effects on the overall field inside the combustion chamber, limits the flow field to be affected only by the rotor movement. However, the inlet flow is very important for the mixture formation and has a great effect on the flow inside the engine chamber even after inlet port closed.

1.10 Thesis Motivation

The rotary engine in comparison with the reciprocating engines is a better choice for UAV (unmanned aerial vehicle) power source because of its characteristics of higher power-to-weight ratio, higher airflow capacity, and larger specific power output at higher allowable speed, smaller frontal area and multi-fuel capability. Due to its fewer moving parts, the rotary engine also has the advantage of mechanic simplicity, low vibration and noise produced. In spite of the advantages mentioned above, the rotary engine has the drawbacks of fuel consumption and pollution emission induced by longer flame propagation, which was constrained in the long and narrow combustion feature. If the drawbacks can be minimized by proper engine design, the performance of the rotary engine will be improved. In the past, the major method in analyzing the performance of rotary engine was just by experiments, and it was very difficult to measure fluid property variation such as pressure and temperature. This is time and money consuming work indeed and does not guarantee a successful design. With the improvement of computational fluid dynamics (CFD), now it is possible to solve such problems efficiently. The purpose of this thesis is to investigate the influence of engine geometry design parameters on the performance of a rotary engine by CFD. By studying the results of this cold flow analysis, it would be possible to get the optimum designed model considering the effect of its design parameter on fluid flow inside the chambers and power output of rotary engine.

2. NON CFD CALCULATION

2.1 Purpose

In this chapter, we want to estimate fluid flow velocity and direction change due to the non-CFD calculation, just by using the finite control volume method and principles of thermodynamic law for ideal gas.

For this aim, the area between rotor and housing profile simply made grid and by calculating the divided areas, while the rotor rotated inside the housing profile, and by assuming boundary conditions for each position, the velocity magnitude that transfers between the grid limits, calculated.

For initial position of the rotor and housing profile, we calculate the (x, y) of the rotor in different angles for the period of the 90-210 degrees, which 1/3 of the volume between the rotor and house rotates from maximum volume in intake position to minimum volume in compression position.

By using the calculated (x, y), we designed the models in Excel program and calculate the grid surface areas by transferring the model to ICEM CFD.

On the other hand, parallel work to this modeling approach was done and another model which designed directly by SOLID WORK program, prepared for obtaining surface areas.

For all the models and rotating angles, the length of the rotor edge and housing edge divided to 10 equal lengths.

2.2 Governing Equations

The ideal gas law is the equation of state of a hypothetical ideal gas. It is a good approximation to the behavior of many gases under many conditions, although it has several limitations. Émile Clapeyron first stated it in 1834. An ideal gas can be characterized by three state variables: absolute pressure (P), volume (V), and absolute temperature (T). The ideal gas law is often written as equation 2.1.

$$PV = nRT \tag{2.1}$$

where the P denote pressure, V as volume, n as number of moles of gas, R as universal gas constant which equals as 8.3145 J/mol.K, and T as temperature of the gas.

The state of an amount of gas is determined by its pressure, volume, and temperature. The modern form of the equation relates these simply in two main forms. The temperature used in the equation of state is an absolute temperature, in the SI system of units, Kelvin.

By replacing n = m / M in which m is the mass (grams) and M is molar mass, and subsequently introducing density ρ = m / V, we get:

$$PV = \frac{m}{M}RT \tag{2.2}$$

$$PV = \rho\frac{R}{M}T \tag{2.3}$$

For the purpose of any calculation, it is convenient to place the ideal gas law in the form of:

$$\frac{P_1V_1}{T_1} = \frac{P_2V_2}{T_2} \tag{2.4}$$

In thermodynamics, an isentropic process is a process in which entropy remains constant. In fluid dynamics, an isentropic flow is a fluid flow that is both adiabatic and reversible. That is, no heat is added to the flow, and no energy transformations occur due to friction or dissipative effects. For an isentropic flow of a perfect gas, several relations can be derived to define the pressure, density and temperature along a streamline. Note that energy can be exchanged with the flow in an isentropic transformation, as long as it does not happen as heat exchange. An example of such an exchange would be an isentropic expansion or compression that entails work done on or by the flow.

For a closed system, the total change in energy of a system is the sum of the work done and the heat added,

$$dU = \delta W + \delta Q \qquad \textbf{(2.5)}$$

The reversible work done on a system by changing the volume is,

$$dW = -pdV \qquad \textbf{(2.6)}$$

Where p is the pressure and V is the volume. The change in enthalpy (H = U + pV) is given by:

$$dH = dU + pdV + Vdp \qquad \textbf{(2.7)}$$

Then for a process that is both reversible and adiabatic (i.e. no heat transfer occurs), $\delta Q_{rev} = 0$ and so $\delta S = 0 = \delta Q_{rev} \,/\, T$. All reversible adiabatic processes are isentropic. This leads to two important observations,

$$\begin{cases} dU = \delta W + \delta Q = -pdV + 0 \\ dH = \delta W + \delta Q + pdV + Vdp = -pdV + 0 + pdV + Vdp = Vdp \end{cases} \qquad \textbf{(2.8)}$$

Next, a great deal can be computed for isentropic processes of an ideal gas. For any transformation of an ideal gas, it is always true that

$$\begin{cases} dU = nC_v dT \\ dH = nC_p dT \end{cases} \qquad \textbf{(2.9)}$$

Using the general results derived above for dU and dH.

So for an ideal gas, the heat capacity ratio can be written as,

$$k = \frac{C_p}{C_v} = -\frac{dp/p}{dV/V} \qquad \textbf{(2.10)}$$

For an ideal gas, k is constant. Hence, on integrating the above equation, assuming a perfect gas, we get

$$pV^k = constant \qquad \textbf{(2.11)}$$

Using the equation of state for an ideal gas, pV = nRT

$$\frac{P_2}{P_1} = (\frac{V_1}{V_2})^{k} \qquad \textbf{(2.12)}$$

$$P_1{V_1}^k = P_2{V_2}^k \qquad \textbf{(2.13)}$$

2.3 Modeling

As it described before, for our calculations, we need to make the control volume as small finite volumes so the governing equations could applied. As the first step in this method, we divide the control volume (here area) to ten parts with equal edge lengths on rotor and housing profile as Figure 2.1 below:

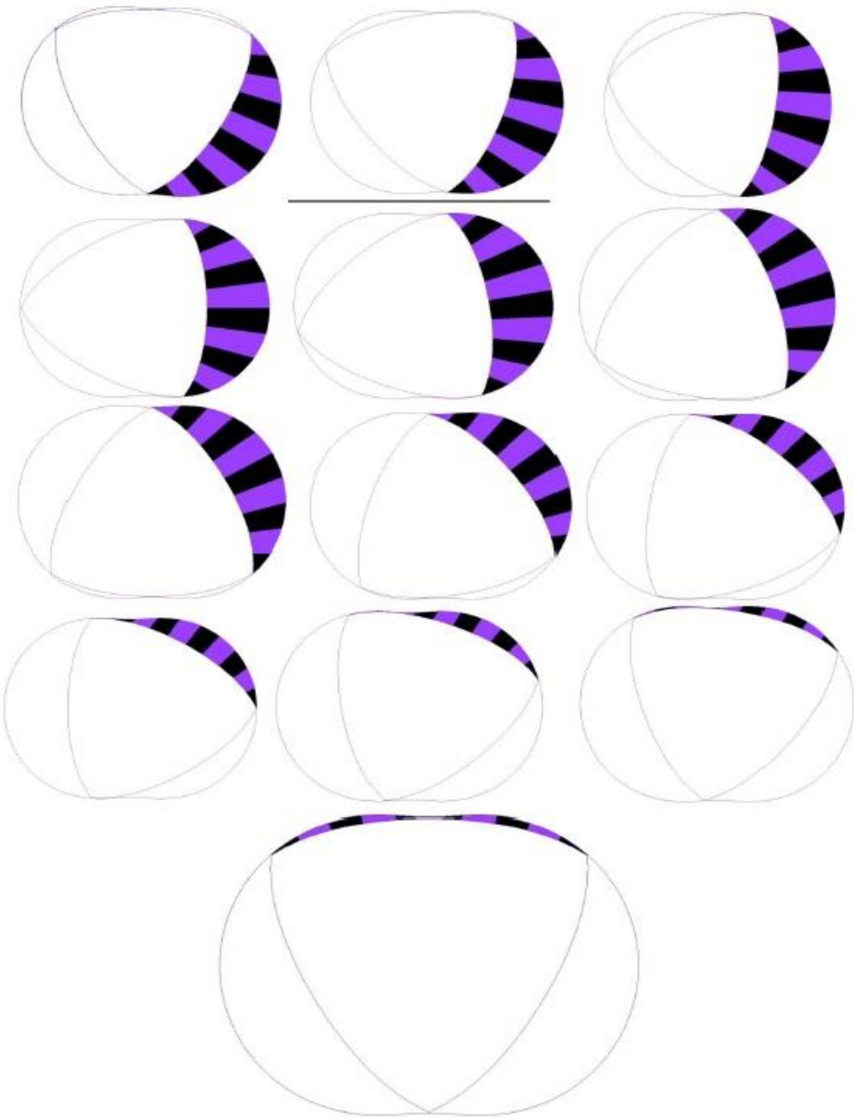

Figure 2.1: Control area rotates from 90-210 degree.

Any colored area which are numbered from 1-10 from the bottom respectively, calculated both in manual method and by applying sensors to any area in SOLIDWORK calculation method, so when the rotor rotates inside the model by inserting new angle, the sensors calculated the related area. The table shows obtained values of the area in any angle with 2.5 degree periods attach in Appendix part.

For any of the positions, the calculation for obtaining the velocity magnitude was done. Our assumption is that the gas inside the area is air as ideal gas, and the pressure and temperature distribution in any position is equal at all the grid parts. We also accept that the density is same while the mass of gas transported between to region limits. If we numbered the second position as two and the initial position as one, then we have:

$$\begin{cases} V_{1,total} = A_{1,calculated} * B \\ V_{2,total} = A_{2,calculated} * B \end{cases} \quad \textbf{(2.14)}$$

Here V is the total volume ($\boldsymbol{Cm^3}$) for the entire region between rotor and housing profile, and B is the width of the rotor. By using the equation (2.13) with k=1.35, calculating the total volume for any case and considering the initial conditions as P_1= 100000 (Pa) and R= 287, we can obtain the pressure at second position. The density of the gas is:

$$\rho_1 = \frac{m}{V} = \frac{P_1}{RT} \quad \textbf{(2.15)}$$

So the density of the gas in first position calculated as ρ_1 = 1.078 and the mass are:

$$m = \rho_1 * V_{1,\,total} = 0.755 \text{ (gram)}$$

Now for any of the divided region, we calculate the related mass inside the region:

$$m_{1,1} = \frac{A_{1,1}}{A_{1,total}} * \rho_1 \quad \textbf{(2.16)}$$

Here the index 1,1 relates to position 1 and zone 1 of this position respectively. Similarly, we obtain the mass in any of the tenth region at position 1 and 2. Again, by using the equation (2.13) to get the total pressure at second position, we calculate the temperature at second mode as equation 2.17.

$$T_2 = \frac{P_2 V_2}{m_{2,total} R} \tag{2.17}$$

It should be noticed that due to mass conservation law, the total mass in first and second position are same as $m_{1,total} = m_{2,total}$

Now the mass of gas in zone 2 of the second position calculated as:

$$m_{2,1} = \frac{P_2 V_{2,1}}{R T_{2,1}} \tag{2.18}$$

Therefore, the difference in mass between position 1 and 2 for zone 1 is as:

$$\Delta m_{zone\ 1} = m_{2,1} - m_{1,1} \tag{2.19}$$

Since we accept the density as equal in any mode, we can calculate the transferred volume of mass also as $V_{1,2}$ (Cm^3). This volume of mass passed through the boundary walls between two-divided regions. The lengths of these walls calculated in SOLIDWORK for any position and any zone.

Using the following equations, we can calculate the velocity for mass transferred between two zones wall:

$$V = \Delta x . A \Leftrightarrow \Delta x = \frac{V_{1,2}}{A_{1,2}} \tag{2.20}$$

If we assume that the engine is working with 3000 RPM, which equals to 18000 (deg/Sec), the time step to rotate as 2.5 degree, would be as:

$$\mathbf{\Delta t = \frac{2.5}{18000} = 1.38 * 10^{-4}}$$

Then the velocity magnitude for mass transferred between two regions:

$$V = \frac{1 * \Delta x}{\Delta t} \tag{2.21}$$

These methods used for three different geometry model, recess in middle of the rotor edge, recess in left side of the rotor edge and recess in right side of the rotor edge. The velocity magnitudes obtained by this method in any rotation of 2.5 degree, when the rotor rotates from maximum volume until the minimum volume on TDC, attached to Appendix part. Following graphs shows this analysis result:

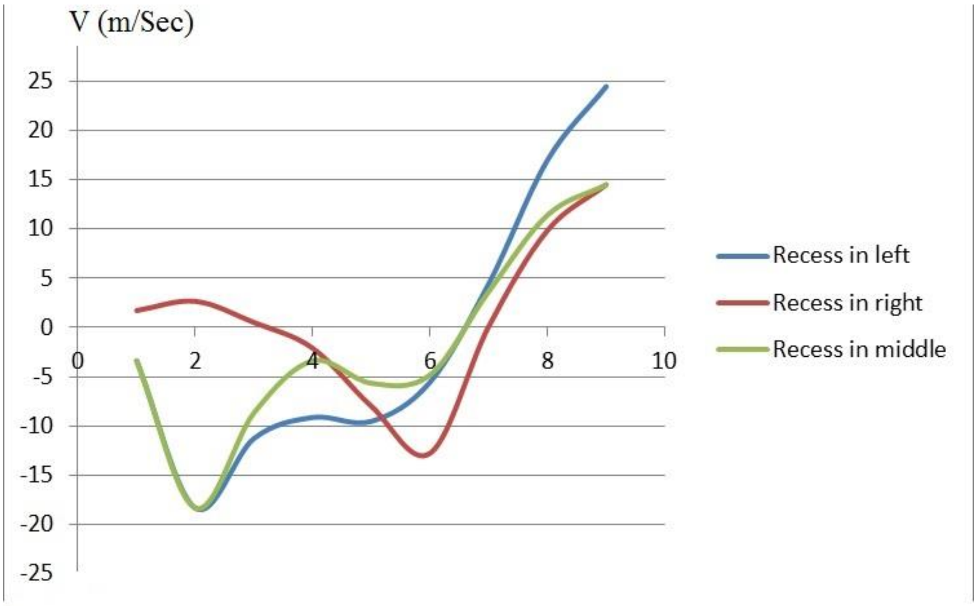

Figure 2.2 : Velocity Magnitude between grid zones at 10 degree bTDC.

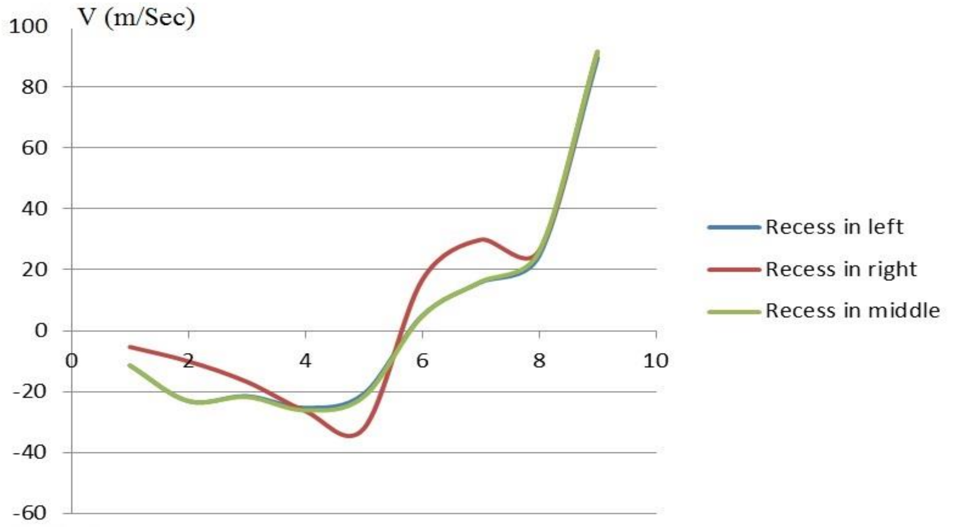

Figure 2.3 : Velocity Magnitude between grid zones at TDC.

The graphs in figure 2.2 and 2.3 show the velocity magnitude (m/s) on vertical axis based on wall numbers between different zones on horizontal axis. Positive values show the velocity vector in the same direction of passing through the lower numbered zone to higher numbered, while the negative values show the opposite form. Figure 2.4 below shows an example of zones position at 10 degree before TDC.

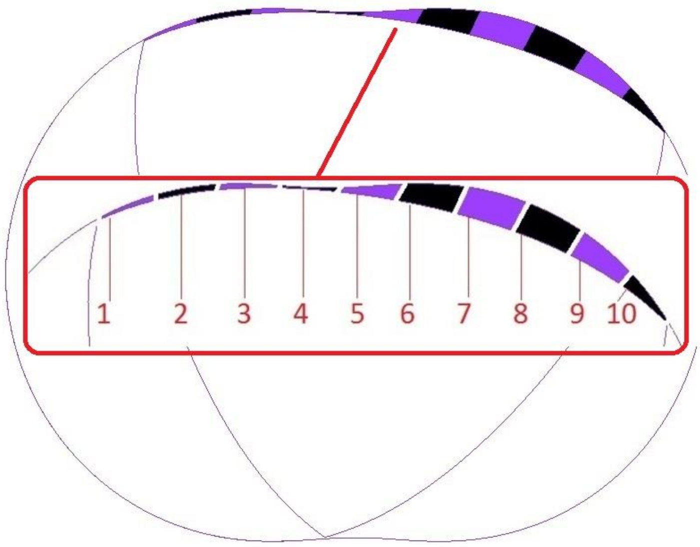

Figure 2.4 : Numbered grid zones for area calculation 10 degree bTDC.

By comparing the figure 2.2 with figure 2.3, we can conclude that for the model with recess positioned in middle of the rotor edge, the velocity vectors are in clockwise direction for the zones 1, 2, 3, 4, 5 and 6 when the rotor is rotating counter-clockwise, and for the zones numbered 7, 8, 9 and 10 these vectors are in the same direction of the rotor rotating, that is counter-clockwise. The difference between the values for the zones that are between 1 to 5 and 5 to 10, shows the different transfer velocities direction, that means the flow inside the chamber is run out from the middle part. By comparing these results with the experimental works reported by H.Schock [29], we can conclude that the apexes sealing, effected the flow pattern inside the chamber. However, for the models with sealed rotor tip, the flow was always directed from tip of the rotor to middle parts, while for our model, the flow velocity vectors are directed to rotor end tips. All calculated data and velocity magnitudes due to several rotor positions attached in Appendix part.

3. CFD THEORY AND MATHMATICAL FORMULATION

3.1 Introduction

Computational modeling enables the researcher to perform simulations that are expensive and time consuming by experiments. The computational fluid analysis (CFD) is becoming an increasingly important part of engine development.

ANSYS FLUENT commercial software provides a unique platform for performing CFD on engine models. It offers a wide selection of tools and methods for accurately simulating all the processes and phenomena of an internal combustion engine. FLUENT provides a viscous model to determine flow phenomena occurring at the wall boundaries, a turbulent model to simulate the random eddy behavior of the flow, and even a secondary break-up model to determine the atomization of fuel droplets.

For all flows, ANSYS FLUENT solves conservation equations for mass and momentum. For flows involving heat transfer or compressibility, an additional equation for energy conservation is solved. Additional transport equations are also solved when the flow is turbulent.

In this chapter, the theory and equations for mass and momentum conservation, energy equation, and turbulence equation will be briefly introduced.

3.2 The Mass Conservation Equation

The mass balance equations are based on rate of increase of mass in fluid element equals the net rate of flow of mass into element.

The rate of increase is:

$$\frac{\partial}{\partial t}(\rho\delta x\delta y\delta z) = \frac{\partial}{\partial t}\delta x\delta y\delta z \quad \textbf{(3.1)}$$

The inflow (positive) and outflows (negative) mass flows are shown at figure 3.1.

Summing all the terms and dividing by the volume $\delta x\delta y\delta z$ results in:

$$\frac{\partial \rho}{\partial t} + \frac{\partial(\rho u)}{\partial x} + \frac{\partial(pv)}{\partial y} + \frac{\partial(\rho w)}{\partial z} = 0 \quad \textbf{(3.2)}$$

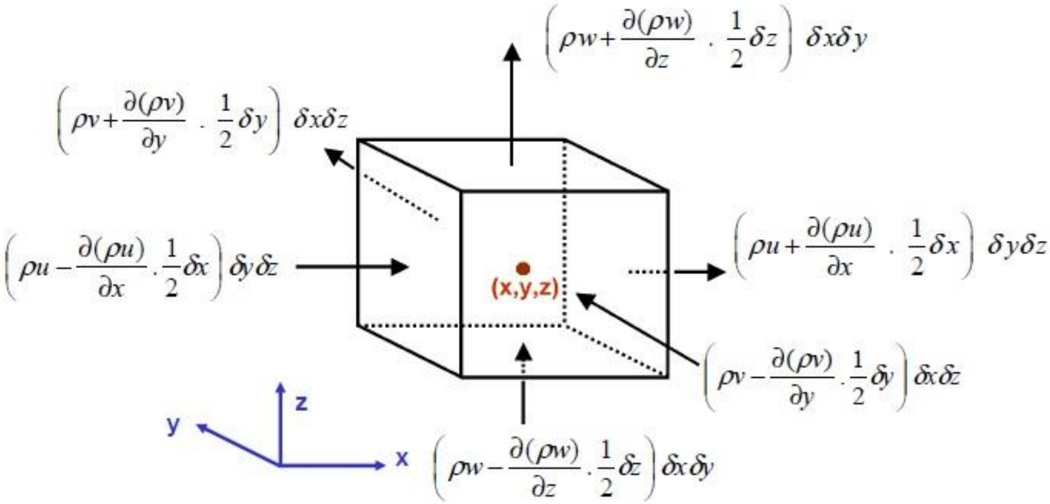

Figure 3.1 : Mass fluxes on fluid element, adapted from (FLUENT, 2012).

So, the equation for conservation of mass, or continuity equation, can be written as follows:

$$\frac{\partial \rho}{\partial t} + \nabla.(\rho v) = 0 \quad \textbf{(3.3)}$$

In vector notation:

$$\frac{\partial \rho}{\partial t} + div\,(\rho u) = 0 \quad \textbf{(3.4)}$$

The first term shows the change in density and the second term shows the net flow of mass across boundaries (Convective term).

This equation is the general form of the mass conservation equation and is valid for incompressible as well as compressible flows. For incompressible fluids $\partial\rho/\partial t = 0$. The operator ∇ referred to gradient as below:

$$\frac{\partial}{\partial x}\vec{\imath} + \frac{\partial}{\partial y}\vec{\jmath} + \frac{\partial}{\partial z}\vec{k} \quad \textbf{(3.5)}$$

The Cartesian form of the conservation equation is as equation 3.6.

$$\frac{\partial \rho}{\partial t} + \frac{\partial(\rho u_i)}{\partial x_i} = \frac{\partial \rho}{\partial t} + \frac{\partial(\rho u_x)}{\partial x} + \frac{\partial(\rho u_y)}{\partial y} + \frac{\partial(\rho u_z)}{\partial z} = 0 \quad \textbf{(3.6)}$$

Where x_i (i=1, 2, 3) or (x, y, z) are the Cartesian coordinates and u_i or (u_x, u_y, u_z) are the Cartesian components of the velocity vector v.

3.3 Lagrangian vs. Eulerian

A fluid flow can be assumed as being a large number of finite sized fluid particles that have mass, momentum and internal energy. So the mathematical laws can be written for reach fluid particle. This named as Lagrangian description of fluid motion.

On the other hand, we can consider how fluid properties change at a fluid element that is fixed in space and time (x,y,z,t) rather than following individual fluid particles. This theory named as Eulerian description of fluid.

All the governing equations can be derived for any of the descriptions and converted to other form.

By defining the total or substantive derivative $^{D}/_{Dt}$:

$$\frac{D\phi}{Dt} = \frac{\partial \phi}{\partial t} + \frac{\partial \phi}{\partial x}\frac{dx}{dt} + \frac{\partial \phi}{\partial y}\frac{dy}{dt} + \frac{\partial \phi}{\partial z}\frac{dz}{dt} \quad \textbf{(3.7)}$$

Bu assuming dx/dt=u, dy/dt=v, dz/dt=w:

$$\frac{D\phi}{Dt} = \frac{\partial \phi}{\partial t} + u.grad\phi \quad \textbf{(3.8)}$$

For some equations, it is easier to calculate them for fluid particles. For a moving particle, the total derivative per unit volume of that property ϕ is given by:

$$\rho \frac{D\phi}{Dt} = \rho \left(\frac{\partial \phi}{\partial t} + u.grad\phi\right) \quad \textbf{(3.9)}$$

The left part of this equation is for moving fluid particle and the right part is for given location in space.

Then we can derive the relationship between equations for a fluid particle (Lagrangian) or a fluid element (Eulerian) as follow:

$$\frac{\partial(\rho\phi)}{\partial t} + div(\rho\phi u) = \rho\frac{D\phi}{Dt} \qquad \textbf{(3.10)}$$

The first term shows the rate of increase of ϕ for fluid element, the second term is the net rate of flow of ϕ out of fluid element, and the last term show the rate of increase of ϕ for a fluid particle.

3.4 Momentum Conservation Equation

Due to Newton´s second law, rate of change for momentum equals sum of forces. Forces on fluid particles are surface forces such as pressure and viscous forces, and body forces that act on a volume such as gravity.

The second law of newton can be written as $F_x = ma_x$ on x direction. The effect of viscous forces on fluid element is as shown in figure 3.2.

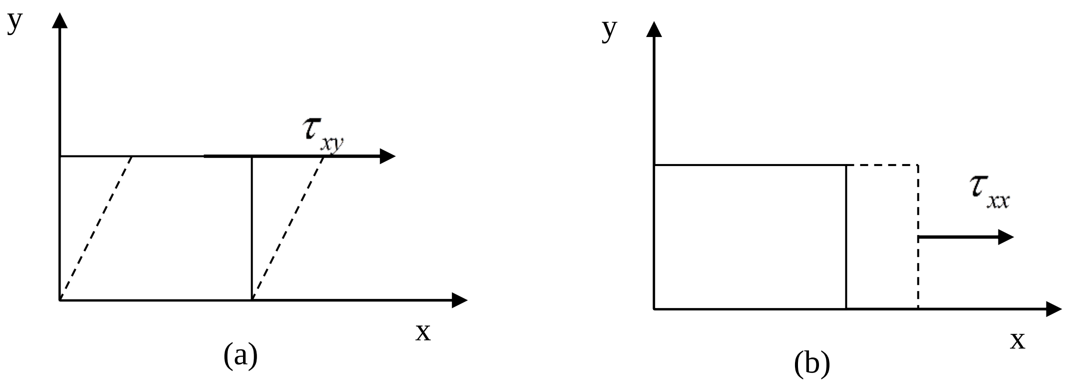

Figure 3.2 : (a) Shear stress, (b) Normal stress.

In most of fluid problems, the stresses are negligible in comparison of shear stress. Just in the cases of large velocity changes $(\partial u / \partial x)$, the normal shearing would be significant.

The body forces that affect the fluid element in x direction are shown in figure 3.3.

Forces aligned with the direction of a coordinate axis are positive. Opposite direction is negative.

The body forces on x direction are as equation 3.11.

$$\left[p-\left(p+\frac{\partial p}{\partial x}dx\right)\right]dydx+\left[\left(\tau_{xx}+\frac{\partial \tau_{xx}}{\partial x}dx\right)-\tau_{xx}\right]dydz$$
$$+\left[\left(\tau_{yx}+\frac{\partial \tau_{yx}}{\partial y}dy\right)-\tau_{yx}\right]dxdz+\left[\left(\tau_{zx}+\frac{\partial \tau_{zx}}{\partial z}dz\right)-\tau_{zx}\right]dxdy \tag{3.11}$$

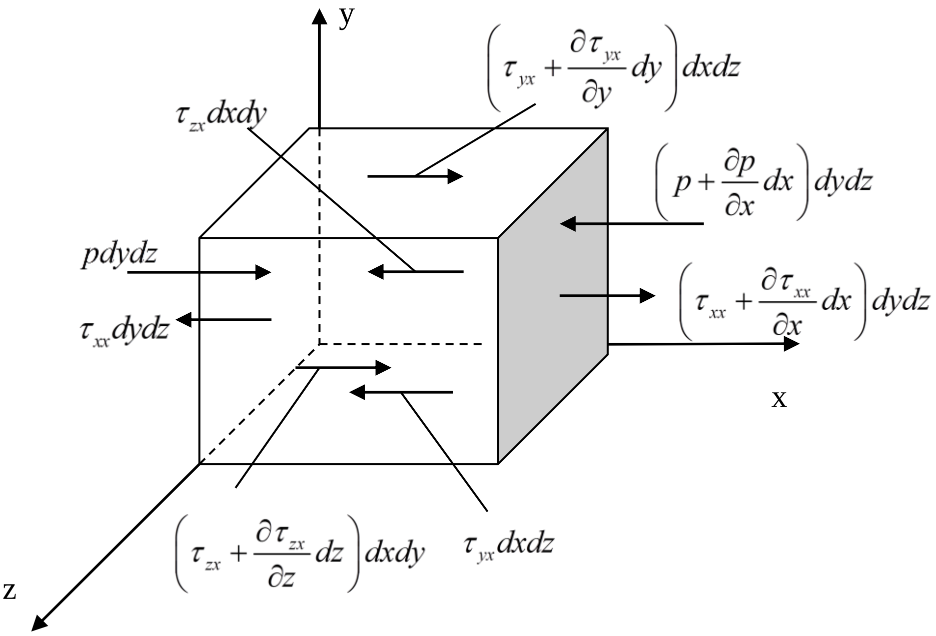

Figure 3.3 : Net forces on fluid element in the x-direction.

By assuming the body forces in x-direction as $\rho f_x(dxdydz)$, then we have the total force as:

$$F_x=\left[-\frac{\partial p}{\partial x}+\frac{\partial \tau_{xx}}{\partial x}+\frac{\partial \tau_{yx}}{\partial y}+\frac{\partial \tau_{zx}}{\partial z}\right]dxdydz+\rho f_x dxdydz \tag{3.12}$$

As we know the mass of fluid element is $m=\rho dxdydz$, and by defining the term $a_x={Du}/{Dt}$, we have:

$$\rho\frac{Du}{Dt}=-\frac{\partial p}{\partial x}+\frac{\partial \tau_{xx}}{\partial x}+\frac{\partial \tau_{yx}}{\partial y}+\frac{\partial \tau_{zx}}{\partial z}+\rho f_x \tag{3.13}$$

Here p is compressive stress and τ is tensile stress.

Similarly, for y and z momentum, we have:

$$\rho \frac{Dv}{Dt} = -\frac{\partial p}{\partial y} + \frac{\partial \tau_{xy}}{\partial x} + \frac{\partial \tau_{yy}}{\partial y} + \frac{\partial \tau_{zy}}{\partial z} + \rho f_y \quad \textbf{(3.14)}$$

$$\rho \frac{Dw}{Dt} = -\frac{\partial p}{\partial z} + \frac{\partial \tau_{xz}}{\partial x} + \frac{\partial \tau_{yz}}{\partial y} + \frac{\partial \tau_{zz}}{\partial z} + \rho f_z \quad \textbf{(3.15)}$$

Conservation of momentum in an inertial (non-accelerating) reference frame is described by equation 3.16.

$$\frac{\partial}{\partial x} (\rho \vec{v}) + \nabla . (\rho \vec{v} \vec{v}) = -\nabla p + \nabla . (\bar{\bar{\tau}}) + \rho \vec{g} + \vec{F} \quad \textbf{(3.16)}$$

Where ρ is the static pressure, $\bar{\bar{\tau}}$ is the stress tensor (described below), and $\rho\vec{g}$ and $\vec{F}$ are the gravitational body force and external body forces.

The stress tensor $\bar{\bar{\tau}}$ is given by:

$$\bar{\bar{\tau}} = \mu . [(\nabla \vec{v} + \nabla \vec{v}^T) - \frac{2}{3} \nabla . \vec{v} I] \quad \textbf{(3.17)}$$

Where μ is the molecular viscosity, I is the unit tensor, and the second term on the right hand side is the effect of volume dilation.

3.5 Compressible Flows

Compressible flows can be characterized by the value of the Mach number as equation3.18.

$$M \equiv \frac{u}{c} \quad \textbf{(3.18)}$$

Here c is the speed of sound in the gas:

$$c = \sqrt{\gamma R T} \quad \textbf{(3.19)}$$

And γ is the ratio of specific heats (c_p/c_v)

When the Mach number is less than 1.0, the flow is termed subsonic. At Mach numbers much less than 1.0 ($M < 0.1$ or so), compressibility effects are negligible and the variation of the gas density with pressure can safely be ignored in your flow modeling. As the Mach number approaches 1.0 (which is referred to as the transonic flow regime), compressibility effects become important. When the Mach number exceeds 1.0, the flow is termed supersonic, and may contain shocks and expansion fans which can influence the flow pattern significantly.

For compressible flows, the ideal gas law is written in the following form:

$$\rho = \frac{p_{op} + p}{\frac{R}{M_w} T} \tag{3.20}$$

Where p_{op} is the operating pressure defined in the Operating Conditions dialog box, p is the local static pressure relative to the operating pressure, R is the universal gas constant, and M_w is the molecular weight. The temperature, T, will be computed from the energy equation.

3.6 Energy Conservation Equation

Due to the first law of the thermodynamic, rate of change of energy of a fluid element is equal to the rate of heat addition plus the rate of work done. Therefore, the energy equation for fluid element is described as net energy change inside the fluid element (A), that equals to net heat transfer of the element (B) plus the work done by surfaces and mass forces on element (C).

The work done by the term C in the unit of time on the fluid which is moving with the speed of u is as below:

$$\rho \mathbf{f} \bullet \mathbf{u}(dxdydz) \tag{3.21}$$

The work done by surface forces is the total of pressure forces and shearing stress forces. As shown in figure 3.3, the work done by pressure forces on left and right surfaces are:

$$\left[up - \left(up + \frac{\partial (up)}{\partial x} dx \right) \right] dydz = -\frac{\partial (up)}{\partial x} dxdydz \tag{3.22}$$

For the upper and downer surfaces, the work done by viscous stress is:

$$\left[\left(u\tau_{yx}+\frac{\partial(u\tau_{yx})}{\partial y}dy\right)-u\tau_{yx}\right]dxdz=\frac{\partial(u\tau_{yx})}{\partial y}dxdydz \tag{3.23}$$

By the same way, if we write the total work done by shearing stress and pressure forces for all the surfaces, the work done by surface forces is:

$$\left[-\frac{\partial(up)}{\partial x}+\frac{\partial(u\tau_{xx})}{\partial x}+\frac{\partial(u\tau_{yx})}{\partial y}+\frac{\partial(u\tau_{zx})}{\partial z}\right]dxdydz \tag{3.24}$$

If we write this equation for all the x,y,z directions and then add to equation (3.21), we can have the equation below named C:

$$C=\begin{bmatrix} -\left(\frac{\partial(up)}{\partial x}+\frac{\partial(vp)}{\partial y}+\frac{\partial(vp)}{\partial z}\right) \\ +\frac{\partial(u\tau_{xx})}{\partial x}+\frac{\partial(u\tau_{yx})}{\partial y}+\frac{\partial(u\tau_{zx})}{\partial z} \\ +\frac{\partial(v\tau_{xy})}{\partial x}+\frac{\partial(v\tau_{yy})}{\partial y}+\frac{\partial(v\tau_{zy})}{\partial z} \\ +\frac{\partial(w\tau_{xz})}{\partial x}+\frac{\partial(w\tau_{yz})}{\partial y}+\frac{\partial(w\tau_{zz})}{\partial z} \end{bmatrix}dxdydz+\rho\mathbf{f}\bullet\mathbf{u}(dxdydz) \tag{3.25}$$

The term B in energy equation states the heat transfer done by radiation or heat transfer in unit volume. If we consider the volume heat flow by $\dot{q}$, heating of fluid element by radiation is as:

$$\rho\dot{q}dxdydz \tag{3.26}$$

For the left surface, the heat transfer is:

$$\dot{q}_x dydz \tag{3.27a}$$

In addition, for the right surface the heat transfer is:

$$\left[\dot{q}_x+\left(\frac{\partial\dot{q}_x}{\partial x}\right)dx\right]dydz \tag{3.27b}$$

The heat transfer in X direction is the total of the equations, shown in equation 3.28.

$$\left[\dot{q}_x - \left(\dot{q}_x + \frac{\partial \dot{q}_x}{\partial x}\right)dx\right]dydz = -\frac{\partial \dot{q}_x}{\partial x}dxdydz \qquad \textbf{(3.28)}$$

As same as this, if we write the total heat transfer for x, y and z directions,

$$-\left(\frac{\partial \dot{q}_x}{\partial x} + \frac{\partial \dot{q}_y}{\partial y} + \frac{\partial \dot{q}_z}{\partial z}\right)dxdydz \qquad \textbf{(3.29)}$$

Now, if we add equation 3.29 to equation qdxdydz, we obtain the following equation for term B in first equation of this chapter:

$$B = \left[\rho\dot{q} - \left(\frac{\partial \dot{q}_x}{\partial x} + \frac{\partial \dot{q}_y}{\partial y} + \frac{\partial \dot{q}_z}{\partial z}\right)\right]dxdydz \qquad \textbf{(3.30)}$$

As we know, ƙ is the coefficient of heat transfer. Due to Fourier heat transfer law:

$$\dot{q}_x = -\kappa\frac{\partial T}{\partial x} \qquad \dot{q}_y = -\kappa\frac{\partial T}{\partial y} \qquad \dot{q}_y = -\kappa\frac{\partial T}{\partial y}$$

By subtitling these equations in (3.30) term:

$$B = \left[\rho\dot{q} + \frac{\partial}{\partial x}\left(\kappa\frac{\partial T}{\partial x}\right) + \frac{\partial}{\partial y}\left(\kappa\frac{\partial T}{\partial y}\right) + \frac{\partial}{\partial z}\left(\kappa\frac{\partial T}{\partial z}\right)\right]dxdydz \qquad \textbf{(3.31)}$$

If we assume that the total energy of the element is sum of kinetic energy and internal energy, then we have the following equation for term A:

$$A = \rho\frac{D}{Dt}\left(e + \frac{1}{2}(u^2 + v^2 + w^2)\right)dxdydz \qquad \textbf{(3.32)}$$

If we rewrite the general energy equation by the terms of A, B and C we obtain, the energy equation achieved as equation 3.33.

$$\rho \frac{D}{Dt}\left(e + \frac{1}{2}(u^2 + v^2 + w^2) \right) =$$

$$\left[\begin{array}{l} \rho \dot{q} + \frac{\partial}{\partial x}\left(\kappa \frac{\partial T}{\partial x} \right) + \frac{\partial}{\partial y}\left(\kappa \frac{\partial T}{\partial y} \right) + \frac{\partial}{\partial z}\left(\kappa \frac{\partial T}{\partial z} \right) \\ -\frac{\partial (up)}{\partial x} - \frac{\partial (vp)}{\partial y} - \frac{\partial (vp)}{\partial z} \\ +\frac{\partial (u\tau_{xx})}{\partial x} + \frac{\partial (u\tau_{yx})}{\partial y} + \frac{\partial (u\tau_{zx})}{\partial z} \\ +\frac{\partial (v\tau_{xy})}{\partial x} + \frac{\partial (v\tau_{yy})}{\partial y} + \frac{\partial (v\tau_{zy})}{\partial z} \\ +\frac{\partial (w\tau_{xz})}{\partial x} + \frac{\partial (w\tau_{yz})}{\partial y} + \frac{\partial (w\tau_{zz})}{\partial z} \end{array} \right] + \rho \mathbf{f} \bullet \mathbf{u} \qquad \textbf{(3.33)}$$

For achieving the kinetic energy equation, we use the momentum equations (3.13) as:

$$\rho \frac{D(u^2/2)}{Dt} = -u\frac{\partial p}{\partial x} + u\frac{\partial \tau_{xx}}{\partial x} + u\frac{\partial \tau_{yx}}{\partial y} + u\frac{\partial \tau_{zx}}{\partial z} + \rho u f_x \qquad \textbf{(3.34a)}$$

$$\rho \frac{D(v^2/2)}{Dt} = -v\frac{\partial p}{\partial y} + v\frac{\partial \tau_{xy}}{\partial x} + v\frac{\partial \tau_{yy}}{\partial y} + v\frac{\partial \tau_{zy}}{\partial z} + \rho v f_y \qquad \textbf{(3.34b)}$$

$$\rho \frac{D(w^2/2)}{Dt} = -w\frac{\partial p}{\partial z} + w\frac{\partial \tau_{xz}}{\partial x} + w\frac{\partial \tau_{yz}}{\partial y} + w\frac{\partial \tau_{zz}}{\partial z} + \rho w f_z \qquad \textbf{(3.34c)}$$

If we add these three equations, we have:

$$\begin{array}{l} \rho \frac{1}{2}\frac{D(u^2 + v^2 + w^2)}{Dt} = -u\frac{\partial p}{\partial x} - v\frac{\partial p}{\partial y} - w\frac{\partial p}{\partial z} + \\ u\left(\frac{\partial \tau_{xx}}{\partial x} + \frac{\partial \tau_{yx}}{\partial y} + \frac{\partial \tau_{zx}}{\partial z} \right) + v\left(\frac{\partial \tau_{xy}}{\partial x} + \frac{\partial \tau_{yy}}{\partial y} + \frac{\partial \tau_{zy}}{\partial z} \right) + \\ w\left(\frac{\partial \tau_{xz}}{\partial x} + \frac{\partial \tau_{yz}}{\partial y} + \frac{\partial \tau_{zz}}{\partial z} \right) + \rho\left(u f_x + v f_y + w f_z \right) \end{array} \qquad \textbf{(3.35)}$$

By rewriting the internal energy equation using these equations:

$$\rho\frac{De}{Dt}=\begin{bmatrix}\rho\dot{q}+\dfrac{\partial}{\partial x}\left(k\dfrac{\partial T}{\partial x}\right)+\dfrac{\partial}{\partial y}\left(k\dfrac{\partial T}{\partial y}\right)+\dfrac{\partial}{\partial z}\left(k\dfrac{\partial T}{\partial z}\right)\\ -p\left(\dfrac{\partial u}{\partial x}+\dfrac{\partial v}{\partial y}+\dfrac{\partial v}{\partial z}\right)+\tau_{xx}\dfrac{\partial u}{\partial x}+\tau_{yy}\dfrac{\partial v}{\partial y}+\tau_{zz}\dfrac{\partial w}{\partial z}\\ +\tau_{yx}\left(\dfrac{\partial u}{\partial y}+\dfrac{\partial v}{\partial x}\right)+\tau_{zx}\left(\dfrac{\partial u}{\partial z}+\dfrac{\partial w}{\partial x}\right)+\tau_{xz}\left(\dfrac{\partial v}{\partial z}+\dfrac{\partial w}{\partial y}\right)\end{bmatrix} \quad \textbf{(3.36)}$$

For the left part of this equation, by using the equation (3.20), and equation (3.22) for surface stresses, the energy equation become as:

$$\frac{\partial(\rho e)}{\partial t}+\nabla\bullet(\rho e\mathbf{u})=\rho\dot{q}+\nabla\bullet(\kappa\nabla T)-p\nabla\bullet\mathbf{u}+M \quad \textbf{(3.37)}$$

Moreover, the term M is:

$$M=\lambda\left(\frac{\partial u}{\partial x}+\frac{\partial v}{\partial y}+\frac{\partial w}{\partial z}\right)^2+\mu\left[2\left(\frac{\partial u}{\partial x}\right)^2+2\left(\frac{\partial v}{\partial y}\right)^2+2\left(\frac{\partial w}{\partial z}\right)^2\right.$$
$$\left.+\left(\frac{\partial u}{\partial y}+\frac{\partial v}{\partial x}\right)^2+\left(\frac{\partial u}{\partial z}+\frac{\partial w}{\partial x}\right)^2+\left(\frac{\partial v}{\partial z}+\frac{\partial w}{\partial y}\right)^2\right] \quad \textbf{(3.38)}$$

3.7 Turbulence Modeling

The choice of turbulence model depends upon considerations such as physics encompassed in the flow, the established practice for a class of problem, level of accuracy required and available computation resource and time.

The instantaneous value of some dependent variables of flow, denoted Φ, can be represented mathematically by an average value, $\overline{\Phi}$, upon which fluctuating component, Φ', has been superimposed.

$$\Phi=\overline{\Phi}+\Phi' \quad \textbf{(3.39)}$$

For a statistically or "steady" flow, it is usual to define $\overline{\Phi}$ as being a time-averaged value as:

$$\bar{\phi}(x_0, t) = \lim_{t_0 \xrightarrow{yields} \infty} \frac{1}{2t_0} \int_{t=-t_0}^{t=t_0} \phi(x_0, t)dt \qquad \textbf{(3.40)}$$

If the flow is non-stationary or unsteady, an ensemble-averaged value is defined as:

$$\bar{\phi}(x_0, t) = \lim_{t_m \xrightarrow{yields} \infty} \frac{1}{2m+1} \sum_{n=-m}^{n=m} \phi(x_0, nt_0 + t) \qquad \textbf{(3.41)}$$

Here, n stands for the number of identical experimental repeat or number of cyclically repeat and t is the time after the start of each experiment or cycle of period t_0 and x_0 is some fixed point in space.

Substituting expression of (3.39) for the flow variables into the instantaneous continuity and momentum equations and taking a time average yields the ensemble-averaged momentum equations. They can be written in Cartesian tensor form as:

$$\frac{\partial \rho}{\partial t} + \frac{\partial y}{\partial x_i}(\rho u_i) = 0 \qquad \textbf{(3.42)}$$

$$\begin{aligned} \frac{\partial}{\partial t}(\rho u_i) + \frac{\partial}{\partial x_j}(\rho u_i u_j) \\ = -\frac{\partial p}{\partial x_i} + \frac{\partial}{\partial x_j}\left[\mu\left(\frac{\partial u_i}{\partial x_j} + \frac{\partial u_j}{\partial x_i} - \frac{2}{3}\delta_{ij}\frac{\partial u_l}{\partial x_l}\right)\right] \\ + \frac{\partial}{\partial x_j}(-\overline{u_i u_j}) \end{aligned} \qquad \textbf{(3.43)}$$

Equations (3.42) and (3.43) are called Reynolds-averaged Navier-Stokes (RANS) equations.

There are different turbulence models that can be used for simulation in FLUENT. The following models are the most popular model that uses in engine simulations.

3.7.1 Standard k-ε model

This is one of the simplest two-equation turbulence model in which the solution of two transport equations determines the turbulent velocity and length scales independently. This model was originally proposed by Harlow and Nakayama. It is a semi-empirical model that is based on model transport equations for the turbulent kinetic energy (k) and its dissipation rate (ε). The model equation for k was derived from the exact equation whereas the model equation for ε was obtained using physical reasoning. It is well known for its robustness, economy and reasonable accuracy for a wide range of turbulent flows. The assumptions made in this model are fully turbulent flow and ignoring the molecular viscosity. The turbulence kinetic energy and its rate of dissipation are obtained from the following transport equations (5):

$$\frac{\partial}{\partial t}(\rho k) + \frac{\partial}{\partial x_i}(\rho k u_i) = \frac{\partial}{\partial x_j}\left[\left(\mu + \frac{\mu_t}{\sigma_k}\right)\frac{\partial k}{\partial x_j}\right] + G_k + G_b - \rho\varepsilon - Y_m + S_k \qquad \textbf{(3.44)}$$

$$\frac{\partial}{\partial t}(\rho \varepsilon) + \frac{\partial}{\partial x_i}(\rho \varepsilon u_i) = \frac{\partial}{\partial x_j}\left[\left(\mu + \frac{\mu_t}{\sigma_\varepsilon}\right)\frac{\partial \epsilon}{\partial x_j}\right] + C_{1\epsilon}\frac{\varepsilon}{k}(G_k + C_{3\epsilon}G_b) - C_{2\varepsilon}\rho\frac{\varepsilon^2}{k} + S_\epsilon \qquad \textbf{(3.45)}$$

Where

$$C_1 = \max\left[0.43, \frac{\eta}{\eta + 5}\right] \qquad \textbf{(3.46)}$$

$$\eta = S\frac{k}{\varepsilon} \qquad \textbf{(3.47)}$$

$$S = \sqrt{2S_{ij}S_{ij}} \qquad \textbf{(3.48)}$$

In these equations, G_k represent the generation of turbulence kinetic energy due to the mean velocity gradients. G_b is the generation of turbulence kinetic energy due to buoyancy. Y_m represent the contribution of the fluctuation dilatation in compressible turbulence to the overall dissipation rate. C_2 and $C_{1\varepsilon}$ are constants. σ_k *and* σ_ε are the turbulent Prandtl numbers for k and Ɛ, respectively. S_k and S_ε are user-defined source terms.

The model constants C_2 , σ_k *and* σ_ε have been established to ensure that the model performs well for certain canonical flow. The model constants are:

$C_{1\varepsilon} = 1.44$, $C_2 = 1.9$, $\sigma_k = 1.0$, $\sigma_\varepsilon = 1.2$

The turbulent kinetic energy k in this model is defined by:

$$k = \frac{\overline{\acute{u}_\iota^{\,2}}}{2} \qquad \textbf{(3.49)}$$

Moreover, its dissipation:

$$\varepsilon = C_\mu^{\,3/4} \frac{k^{3/2}}{l_t} \qquad \textbf{(3.50)}$$

Where l_t is the turbulence scale and C_μ is an empirical coefficient.

3.7.2 RNG k-ε model

This model is derived using a rigorous statistical technique called the renormalization group theory. It is similar in form to the standard k- ε models. The following refinements are included in RNG k- ε models:

- It has an additional term in its equation for ε that significantly improves the accuracy for rapidly strained flows.
- The effect of swirl on turbulence is included in RNG model enhancing accuracy for swirling flows.
- The RNG theory provides an analytical formula for turbulent Prandtl numbers, while the standard model uses user-specified, constant values.
- While the standard model is a high Reynolds number model, the RNG theory provides an analytically derived differential formula for effective viscosity that accounts for low Re-effects.

3.7.3 Realizable k- ε model

The realizable k-ε model includes new formulation for the turbulent viscosity and the dissipation rate. The term realizable means that the model satisfies certain mathematical constraints on the Reynolds stresses, consistent with the physics of turbulent flows. Realizable k- ε model gives a more accurate prediction of the spreading rate of both planar and round jets than the standard k-ε model. In addition, it is likely to provide superior performance for flows involving rotation, boundary layers under strong adverse pressure gradients, separation, and recirculation.

This model differs from the standard model in two important ways. First is that the realizable model contains new formulation for the turbulent viscosity, and secondly new transport equation for the dissipation rate, ε, has been derived from an exact equation for the transport of the mean-square vortices fluctuation.

3.8 Dynamic Mesh

In this chapter, a brief introduction and different methods for moving and deforming mesh will be introduced in summary.

Moving and Deforming Mesh named as MDM and dynamic mesh, is an approach that allow the shape of the CFD domain to change during a simulation, so at each time step some cells are added or removed or stretched to accommodate the motion. This has done from an initial mesh and the solver handles mesh update during the simulation. The main advantageous of MDM method are better predict the interaction between parts, giving the influence of parts motion on the flow, or flow on the part motions, and at last mesh motion is function of the solution.

The MDM model can be used to move rigidly boundaries or zones due to its translational or rotation motion, or deforming and deflecting boundaries.

The theory of MDM is based on conservation equation. With respect to dynamic meshes, the integral form of the conservation equation for a general scalar, Ø, on an arbitrary control of volume V, whose boundary is moving can be written as:

$$\frac{d}{dx}\int_{v} \rho\emptyset dV + \int_{\partial v} \rho\emptyset(\bar{u} - \bar{u}_g).dA = \int_{\partial v} \Gamma\nabla\emptyset.d\bar{A} + \int_{V} S_{\emptyset} dv \quad \textbf{(3.51)}$$

Where $\bar{u}$ is the flow velocity vector, $\bar{u}_g$ is the mesh velocity of the moving mesh, Γ is the diffusion coefficient, $S_Ø$ is the source term of Ø, ðV is the used to represent the boundary of the control volume V, and ρ is the fluid density.

By using the 1st order backward difference formula: time derivative

$$\frac{d}{dt}\int_{V} \rho\emptyset dV = \frac{(\rho\emptyset V)^{n+1} - (\rho\emptyset V)^{n}}{\Delta t} \quad \textbf{(3.52)}$$

By using the 2nd order backward difference formula: time derivative

$$\frac{d}{dt}\int_V \rho\emptyset dV = \frac{3(\rho\emptyset V)^{n+1} - 4(\rho\emptyset V)^{n} + (\rho\emptyset V)^{n-1}}{2\Delta t} \quad \textbf{(3.53)}$$

MDM does not allow for topology change during the simulation. It means that objects may not move from one fluid zone into another. Another limitation is that polyhedral cells in general are not compatible with MDM.

For the aim of the simulation for dynamic zone, it is required to ensure the motion of boundary and cell zone with respect to others, so a dynamic zone motion must be defined.

There are five different types of dynamic zones, stationary, rigid body, deforming, user defined and system coupling. For any of each, the options of motion attribution, geometry definition, meshing option and solve option could be defined.

By default if no motion (moving or deforming) is assigned to boundary or cell zone, this zone is not considered during the mesh update.

When there is motion of both the cells zone as well as the boundary zone, it is necessary to apply a stationary condition.

A rigid body condition does not deform as it moves in the domain. Its shape remains unchanged along the motion and it can apply on boundary zone and cell zones. The motion of the rigid body is either defined by profile, in cylinder motion, 6 DOF motion or motion with user defined function (UDF).

Selecting the deforming condition makes it possible to define the zones in which the shape of the zone changes during the simulation. It is important to know that FLUENT does not know the shape of the underlying geometry; it only knows the node position. Therefore, if nodes are to slide along a boundary, FLUENT needs to be told the shape of that boundary (curve / plane / cylinder). There are also user define motion to select the motion of the zone with UDF and system coupling method to link the two different application of the zone motion (one fluid and one mechanical).

After defining the zones motion, it is necessary to select the suitable method for dynamic mesh. There are three different dynamic mesh methods, which are briefly, introduce in following section:

3.8.1 Smoothing method

The smoothing method moves interior nodes to absorb the motion of moving or deforming boundaries. The number of nodes and their connectivity does not change. This method is available for triangular, tetra, quad, hexa, prism and poly (cut cell) meshes. Two different smoothing methods are available for interior zones, spring based smoothing and diffusion based smoothing.

3.8.1.1 Spring based smoothing

The edges between any two nodes are idealized as a network of springs. A displacement at a boundary node will generate a "spring force". Using Hooke's Law, this force on a node, can be written as:

$$\overline{F_i} = \sum_{j}^{n_i} k_{ij} \left(\Delta\overline{x_j} - \Delta\overline{x_i}\right) \quad \textbf{(3.54)}$$

Where $\Delta\overline{x_i}$, $\Delta\overline{x_j}$ are the displacements of node i and its neighbor j, n_i is the number of nodes connected to i. k_{ij} is the spring constant.

$$k_{ij} = \frac{k_{fac}}{\sqrt{\left|\overline{x_i} - \overline{x_j}\right|}} \quad \textbf{(3.55)}$$

K_{fac} is the value you enter as spring constant factor (between 0 and 1).

At equilibrium, the net force from all the springs connected to the node must be zero. This condition results in an iterative equation such that:

$$\Delta\bar{x}_i^{m+1} = \frac{\sum_j^{n_i} k_{ij}\Delta\bar{x}_j^m}{\sum_j^{n_i} k_{ij}} \quad \textbf{(3.56)}$$

At convergence, the positions are updated such that:

$$\bar{x}_i^{n+1} = \bar{x}_i^n + \Delta\bar{x}_i^{converged} \quad \textbf{(3.57)}$$

One can control the solution of the above iterative equation by convergence tolerance and number of iterations. The iterative solutions stop when any of these conditions are met.

It is important to define the accurate number of iterations. The iterative solution of the smoothing either stops when converged or at maximum number of iterations. The effect of the spring constant factor will decrease as the smoothing converges. The default value of 20 is often not sufficient to reach convergence in any condition.

3.8.1.2 Spring based smoothing, Laplace smoothing

Laplace Smoothing is the simplest mesh smoothing method available for deforming face zones. This method adjusts the location of each mesh node to the geometric center of its neighboring nodes. It is a computationally inexpensive method but it does not guarantee an improvement on mesh quality, repositioning a vertex by Laplacian smoothing can result in poor quality elements. To overcome this problem, ANSYS FLUENT only relocates the nodes if and only if there is an improvement in the mesh quality. Laplace smoothing is the default smoothing method used for 2.5D re-meshing but it can also be applied in other cases such as deforming face zones with triangular elements (3D) or deforming “edge zones” with linear elements (2D).

Spring Based Smoothing is a quick and effective way to smooth any cell or face zone whose boundary is moving or deforming. For non-tetrahedral cell zones (non-triangular in 2D), the spring-based method can be used when the following conditions are met:

- The boundary of the cell zone moves predominantly in one direction
- The motion is predominantly normal to the boundary zone

Polyhedral cells are particularly likely to become highly skewed with spring-based smoothing. For cases with conditions as the ones listed above or with large motion or deformation, the user should use the Diffusion Based Smoothing.

3.8.1.3 Spring based smoothing, Diffusion

For diffusion-based smoothing, the mesh motion is governed by the diffusion equation:

$$\nabla.(\gamma\nabla\vec{u}) = 0 \quad \textbf{(3.58)}$$

Where $\vec{u}$ is the mesh displacement velocity and γ is the diffusion coefficient.

FLUENT has two different formulation of the diffusion coefficient

Boundary distance formulation:

$$\gamma = \frac{1}{d^{\alpha}} \tag{3.59}$$

Where d is the normalized boundary and α is a user input parameter.

Cell volume formulation:

$$\gamma = \frac{1}{V^{\alpha}} \tag{3.60}$$

Where V is the normalized cell volume and α is a user input parameter.

The flow field must be initialized for obtaining values of d & V before previewing the mesh smoothing.

α ≥0 yields for both formulation. Recommended range is between 0 and 2.

The vector equation above is discretized using standard finite volume method, and the resulting matrix is solved iteratively using the algebraic multigrid (AMG) solver. The cell-centered solution for the displacement velocity is interpolated onto the nodes using inverse distance weighted averaging, and the node positions are updated according to:

$$\bar{x}_{new} = \bar{x}_{old} + \bar{u}\Delta t \tag{3.61}$$

Diffusion based smoothing is generally more computationally costly than spring based smoothing but tends to generate better quality meshes, but allows larger deformations than spring based smoothing.

About the diffusion parameters, α = 0 gives γ = 1 and a uniform diffusion of the boundary motion into the interior of the mesh, while A higher value of α will cause preserve the mesh close the moving boundary better. A value of 1-1.5 often works well if one wishes to let the “far field” Mesh absorbs the motion.

The iterative solution of the Diffusion - Based smoothing either stops when converged or at maximum number of iterations.

3.8.2 Layering Method

Layering method requires the cell shapes of quad elements in 2D and wedge or hexa elements in 3D analysis and it could not be used for triangular meshes. It is most useful for linear motion bud also can be used for pure rotational motion.

Layering involves the creation and destruction of cells, cells are added as the zone grows, deleted as the zone shrinks, and their connectivity change. There is an option for layering method, which divided to two separate modes, height based layering mode that is based on constant height, and ratio based layering mode. In height based mode every new cell layer created has the same height. In ratio based mode, layering maintains a constant ratio of cell heights between layers with linear growth. The split factor and collapse factor use for defining these ratio.

The layering method is much faster and more accurate than unstructured remeshing.

3.8.3 Remeshing method

The remeshing method makes it possible to simulate problems with large relative motion of boundaries. Cells and faces are remeshed when skewness or size exceeds specified limits. The number of nodes and their connectivity changes as cells or faces are added or deleted. This method is available for triangular tetra meshes (with or without prism layers), 2.5D Prism zones and cut cell.

Remeshing and smoothing are typically used together so they could produce better quality mesh and allows larger time steps.

Some cases only require remeshing of interior cells while other also needs to remesh boundary faces. There are different remeshing methods as local cell, zone remeshing, local face, region face, 2.5D and cut cell zone. Except the local face remeshing method, the others could be used for both 2D and 3D meshes. Local cell remesh just interior cells, while zone remeshing remesh he complete cell zone if the local mesh fails. Region face remeshes face adjacent to a moving boundary. The cut cell method remeshes cells and faces of a complete zone.

In local cell remeshing method, the interior cells that exceed the user specified skewness or size criteria has been marked and locally remeshed. The marking of cells based on skewness is done every time step while the marking of cells based on length scale is performed with the user specified “Size Remeshing Interval”. The mesh is updated if the new cells improve the skewness. The solution is interpolated from the old cells. All criteria are used to mark cells for remeshing. There is no guarantee that the remeshed cells will fulfill the criteria though. The global size and skewness parameters specified under “Mesh Method Settings” applies to all deforming zones if not other criteria are defined locally for each zone. The local length scales are set to 0 by default and skewness is set to 1. If these defaults are kept, the global parameters will be used.

In local face remeshing methods, it allows local remeshing at deforming boundaries for 3D cases and marks the faces (and adjacent cells) on deforming boundaries based on skewness.

In zone remeshing method, it re-generates cells for a complete cell zone. It could be enabled by default when local cell remeshing is activated and will be triggered if local cell fails to create an acceptable mesh .Zone remeshing will be invoked if skewness be more than 0.98. It remeshes both interior cells, faces on adjacent deforming boundaries, and can reproduce prism layers in 3D meshes.

Zone remeshing automatically detects prism layers height and distribution number of layers. It is available for triangular cells in 2D also. The zone remeshing looks at local size criteria when remeshing face boundaries. It uses relevant local size to control the remeshing of face.

The region face remeshing is also like zone remeshing and provides additional remeshing controls for deforming boundaries adjacent to a moving boundary. It marks the faces and adjacent cells on deforming boundaries based on maximum and minimum length scales.

Face region can remesh across multiple face zones also. The face zone remeshing needs relevant local size criteria to work as intended. The global parameters will not be used if the local parameters are kept as default. In 3D simulations, the face zone method can be used on prism layer meshes.

Size remeshing interval (SRI) is the most important parameter in adjusting the remeshing parameters. It controls how frequently cells are marked for remeshing based on the cell size.

- If SRI is large, then remeshing interval is dominating by skewness.
- If SRI is small, then remeshing interval is strongly affecting by both cell size and skewness.

Setting SRI to one is often necessary for larger time steps. It is common that the time step size is limited by the remeshing rather than the flow solution.

It should be noted that cells are marked for remeshing based on size and skewness criteria prior to the movement of the boundary. During remeshing, FLUENT reports skewness and cell size data. These values are from before the movement of any boundary. There is no direct control over skewness and size criteria of the remeshed cells. Therefore, you can only indirectly control these criteria of the deformed mesh. For the above reason, it is often worth using rather tight criteria for both skewness and size.

3.9 Defining the Time Step Size

Time step size chosen based on the length of the smallest cell on initial mesh, and by global and local mesh parameters defined during the set up. By estimating the maximum expected velocity of the bodies which are in motion,

$$\Delta t = \frac{\Delta s}{V} \tag{3.62}$$

S is the minimum height of the mesh, and V is the speed.

A good expectation of time step could guarantee the successes of the dynamic mesh simulation.

3.10 User Defıned Functıon (UDF)

A UDF is a custom routine (or Macro) which extends FLUENT capabilities for different simulations. The UDFs are written in ‘C’ language by the users depending on their applications and they can be dynamically linked with FLUENT solver. UDF allows the user to define their own specific problem, going beyond features available in the FLUENT graphical user interface.

Dynamic Mesh makes use of 3 types of macros generally:

- Rigid Body Motion (DEFINE_CG_MOTION)
- DEFORMING (DEFINE_GEOM) (DEFINE_GRID_MOTION)
- PROPERTY (DEFINE_DYNAMIC_ZONE_PROPERTY) (DEFINE_CONTACT)

3.10.1 DEFINE_CG_MOTION UDF Macro

This macro allows object motion as a function of time during the simulation and could be devided to three different methods:

- Translational motion
- Rotational motion
- Combination of Translation and Rotation motion

In each case with respect to the CG (Center of Gravity) of the body which is specified by the user (not calculated by the code), the UDF runs. CG is continually updated as the body moves.

This macro defines a prescribed motion and the object moves as a rigid body. The object which move with this code could be both the boundary(ies) or fluid zone(s). In both cases all nodes associated with it move as one, without any relative motion (deformation).

This macro has the following defining command:

DEFINE_CG_MOTION(name, dt, vel, omega, time, dtime)

Input parameters of this command are "Name", which is the name of the UDF to hook it up, "dt" as the deformed thread, "time" as current time, and "dtime" as current time step.

Output parameters are "vel" as translational velocity, and "omega" as rotational velocity.

There are also some Time-Dependent Variables, which uses as solver macros for Time-Dependent Variables. These variables are "CURRENT_TIME" which returns to real current flow time (in second), "CURRENT_TIMESTEP" which returns to real current physical time step size (in second), and "N_TIME" which return integer number of time steps.

4. MODELING

This chapter is devoted to getting a general idea about Wankel rotary engine modeling, geometry creation, meshing the model, and preparing the model for FLUENT computational program for fluid analysis. In order to set up the CFD model, several conditions must be defined. These include basic dimensions of the model, approximations done during the geometry modeling, boundary conditions, meshing techniques, dynamic mesh setup and FLUENT user defined functions.

The simulations present in this chapter consider both 2D and 3D modeling for the geometry while considering all the three chambers simultaneously. The fluid simulation will only apply just for 2D model because of some limitations on processing time and available computer memories. In this simulation, any sealing on end edges of the rotor ignored so if there were any leakage between the housing and rotor edges, it could also observed during the simulation. The model used in this study does not include any injector or spark plug holes.

4.1 Housing

The housing inner surface has a mathematical form known as a trochoid or epitrochoid. This epitrochoid is the locus of the tip point of an arm fixed on the revolving circle B in radius q when it rolls along the periphery of the base circle A in radius q as inscribed. [9]

Therefore the equation of this profile can be expressed by the coordinates of Point P(x,y) in the coordinate system of (x,y) of the center of base circle, as equation 4.1 shows:

$$\begin{cases} x = e\cos\alpha + (R+a)\cos\beta \\ y = e\sin\alpha + (R+a)\sin\beta \end{cases} \tag{4.1}$$

Here, e is the center distance between base circle A and rolling circle B, which named as Eccentricity, R is the length of arm fixed on rolling circle B or generation radius or rotor center-to-tip distance, and β is angle of rotation of revolving circle B on its axis. The reason of using 3 as multiply factor for α in first term is that the rotary engine in practical application presently uses the trochoid with coefficient of 3. So in our calculations $\alpha/3 = \beta$. Figure 4.1 shows the main parameters for trochoid generation.

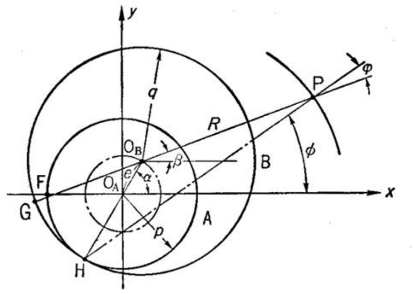

Figure 4.1 : Generation of trochoid (Yamamoto, 1981).

We use two separate ways for solving these equations from 0 to 360 degree and creation of the points with (x,y) coordinates. The first approach is based on formula used as parameter description in MICROSOFT EXCELL program to create the points and connect them with spline as shown in figure 4.2. The second approach is to create the profile in SOLIDWORK, directly by spline drawing tool using the parametric formula. Values for e and R are given in table 4.1 rotary characteristics. By extending this epitrochoid shape by the width of the real housing, we can obtain a three dimensional solid housing model. It is important to use the exact shape of housing in order to construct the dynamic mesh motion inside the FLUENT. Additionally, these equations are used also in the dynamic mesh user defined code explained in UDF related chapter.

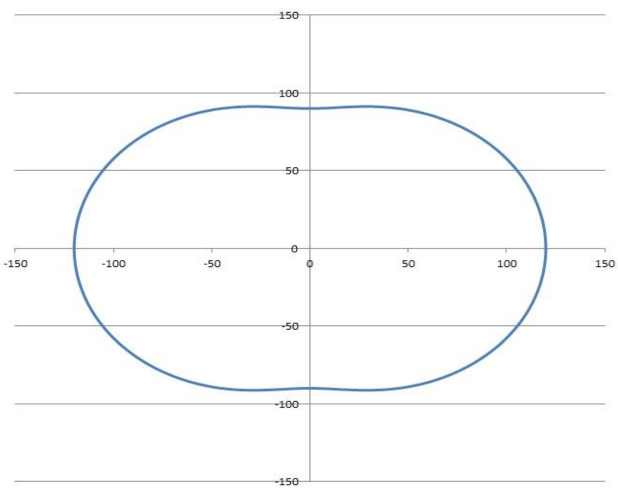

Figure 4.2 : Single trochoid (Modeled in EXCELL).

4.2 Rotor Geometry

The envelope of peritrochoid is a pattern drawn by the peritrochoid fixed on circle. The inner line of this trochoid is a basic curve forming the contour of the rotor. The rotor contour equation is as below [9]:

$$\begin{cases} X = A + B + C \\ Y = D + E + F \end{cases} \quad \textbf{(4.2)}$$

Where:

$$\begin{cases} A = Rcos(2\alpha) \\ B = 3e^2[\cos(8\alpha) - \cos(4\alpha)]/2R \\ C = e(cos5\alpha + cos\alpha)(1 - \dfrac{9e^2}{R^2}(sin3\alpha)^2)^{1/2} \\ D = Rsin(2\alpha) \\ E = 3e^2(\sin(8\alpha) + \sin(4\alpha))/2R \\ F = e(sin5\alpha - sin\alpha)(1 - \dfrac{9e^2}{R^2}(sin3\alpha)^2)^{1/2} \end{cases} \quad \textbf{(4.3)}$$

These functions are cyclic functions with the period of 2π. The inner envelope corresponds to α between π/6 until π/2, 5π/6 until 7π/6 and 3π/2 until 11π/6. By Using this equations between these periods, several coordinates of points (x,y) achieved so the edges profile of the rotor obtained. In our study, due to the simplified model, the rotor's edges do not contain any designed model for sealing parts, so the curves joined directly.

As like the housing profile, the rotor profile is also calculated using relative equations in both MICROSOFT EXCELL and SOLIDWORK. Figure 4.3 shows the base profile for the rotor.

The position of the pocket geometry on rotor´s edges, modeled by real Wankel engine model for the Mazda. This chamber has many advantages for the engine performance. Expansion and compression process, turbulence inside the chamber, mixing and combustion are highly influenced by the rotary pocket design.

The rotor edge length on real model is 187 cm, where the combustion chamber placed between 43 cm until 144 cm. Maximum depth of the combustion chamber on rotor is in middle part of it with 6 mm height. The rotor combustion chamber followed almost the same profile of the rotor. For different analyzing models, we will place the combustion chamber in three different positions on middle, left and right. Figure 4.4 shows the position of combustion chamber in middle of the rotor edge.

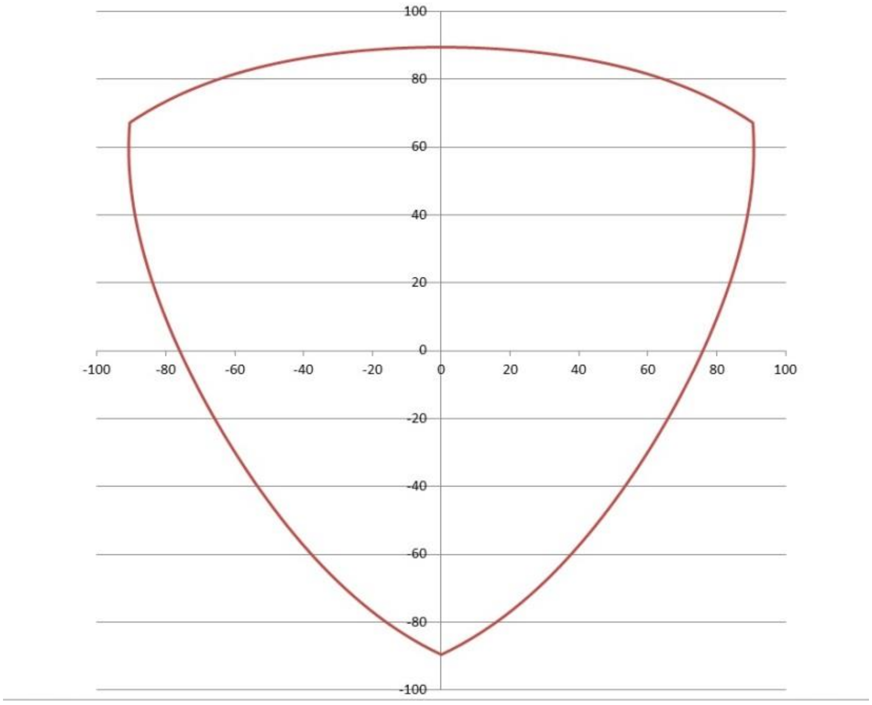

Figure 4.3 : Rotor Geometry (Modeled in EXCELL).

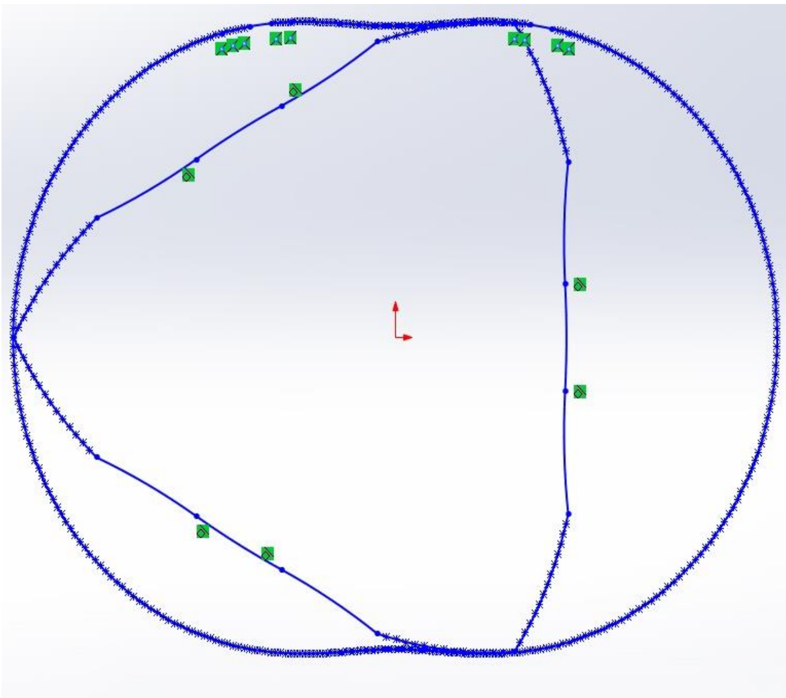

Figure 4.4 : 2D model of engine geometry.

4.3 Rotor and Housıng Montage

Placing the rotor inside the housing profile without using the gears on shaft, is one of the challenging issues. Since the rotor has eccentricity rotation, it was not possible to place a rotor inside the housing directly. In any effort, although by merging the rotor edges on housing profile, while the rotor rotates inside housing, it exited from the profile. The reason of this relates to self-rotating of the rotor while if rotates due to its center of rotation.

In year 1977, P.Philipps in his thesis, obtained two transfer equations so the rotor equation, could use as new (x,y) transferred coordinates due to the same center of the housing profile (10). Without using these equations, if we model both the housing and rotor profiles, the rotor placed out of the housing profile, normally downer of housing.

The transfer equations are:

$$\begin{cases} X_k = x.\cos(\alpha/n) - y.\sin(\alpha/n) + ecos(\alpha+\pi) \\ Y_k = x.\sin(\alpha/n) + y.\cos(\alpha/n) + e.\sin(\alpha+\pi) \end{cases} \quad \textbf{(4.4)}$$

In our calculations, we assume n=3.

Another significant point for placing the rotor inside the housing profile was the distance between rotor edge and housing. Because of some limitations that will explain in mesh motion part, there should be small gap between rotor edge and housing. Several values tested for this gap size and the gap size of 0.2 mm gives the acceptable results.

4.4 Rotary Engine Model Characteristics

The parameters used in this modelling are obtained from Mazda RX-7 engine. The locations of the intake and exhaust ports are obtained from NSU Model KKM 502 (9). Table 4.1 shows the main characteristics of engine design parameter and table 4.2 shows the port timing of NSU engine.

All the parameters in table 4.1 obtained for the case in which combustion chamber is in middle of rotor edges.

Table 4.1 : Rotary engine model characteristics.

Generating Radius (R) (mm)	104.8
Eccentricity (e) (mm)	15
Gap (a) (mm)	0.2
Displacement (Cm^3)	654
Engine Speed (rpm)	3000 – 9000
Minimum Volume (mm^3)	81144
Maximum Volume (mm^3)	734400
Geometric Compression Ratio	9.05

Table 4.2 : Rotary engine model ports timing.

Condition	Degree
Intake Open	108 (B.T.D.C)
Intake Closed	40 (A.B.D.C)
Exhaust Open	63 (B.B.D.C)
Exhaust Closed	71 (A.T.D.C)

Intake and exhaust ports opening and closing time have a great effect on the overall engine performance. To get high performance, a longer open and a greater opening area is required for intake. Also at low speeds, for getting better performance, a minimum possible overlap of intake and exhaust ports is required.

4.5 Preparing the CAD Model

As mentioned before, the cad model for this study obtained by two different approaches. The first approach was by calculating the different coordinates of (x, y) for several points on rotor and housing profile, using MICROSOFT EXCELL software. This program then could connect these points by spline together. By using the different values for the angle α, R, e and a, it was possible to schematically study the rotation of the rotor inside the housing and the different gap dimensions between the rotor and housing profile. Figure 4.5 shows the different positions of the rotor inside the housing by changing the value for α.

After creation of the base profiles, by using the AUTOCAD software, several splines which created by EXCELL, converted to four main lines for three rotor edges and one housing profile. The importance of this convert is to have a smooth and semi-arc profile on edges for getting the better result on meshing the edges. Importing this model directly to CAD program gives us a 2D model for base profile of the rotor and housing.

Another approach was to use the spline drawing option of SOLIDWORK software, so it could draw the 2D model using the parametric equations between defined periods of angles, and the extrude the profile for about 80mm to obtain a 3D model, as shown in figure 4.6.

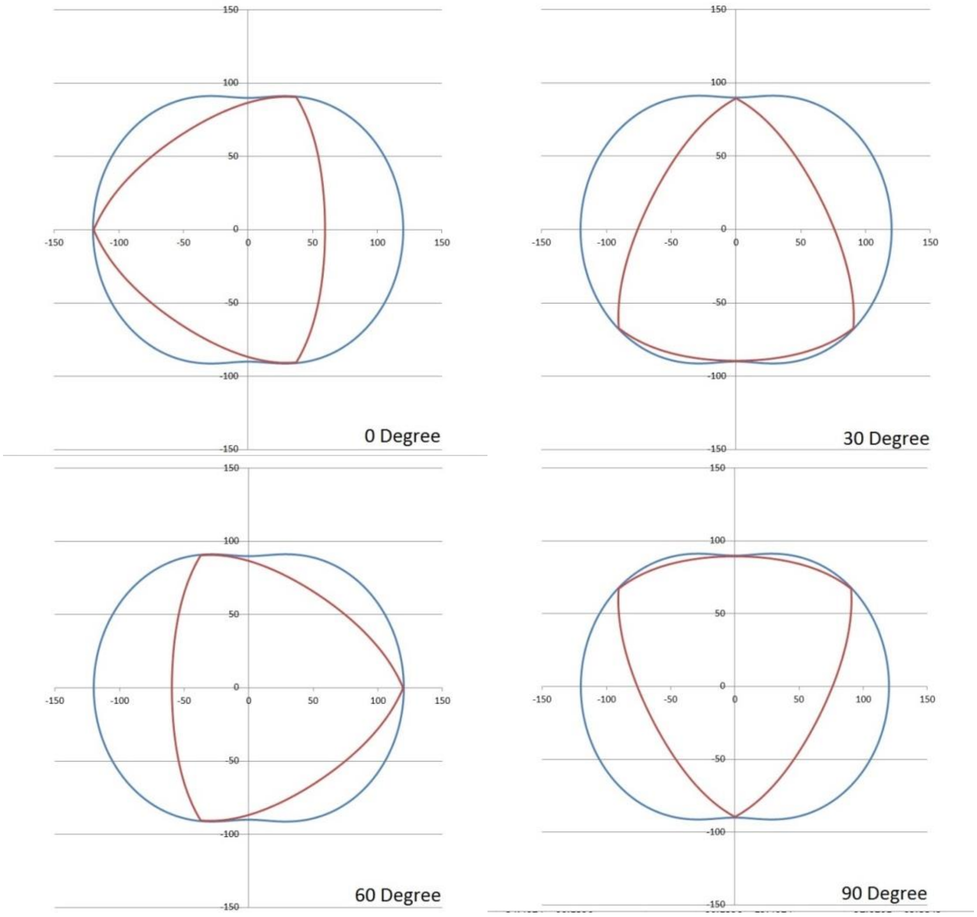

Figure 4.5 : Different positions of the rotor inside the housing profile for α.

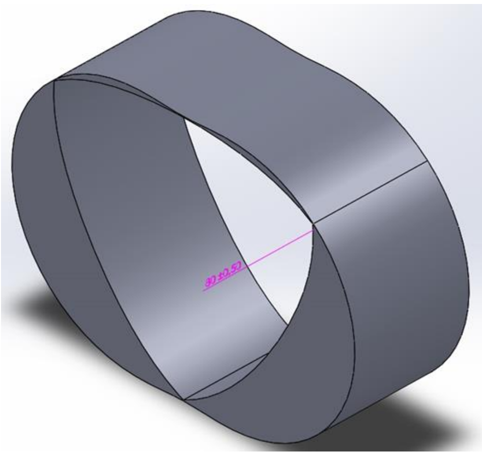

Figure 4.6 : 3D model of engine geometry.

The model that will be imported to ANSYS program should contains the volume in which the fluid flow exists. Positioning of the intake and exhaust ports has done considering the table 4.2, as figure 4.7 below. Also before making the grids on any surfaces or area of the model, it is important to define the boundary conditions for any surface and wall on geometry. It means that any edges or area should have its own name and be separated from other parts so that we could apply boundary conditions for it in FLUENT. Figure 4.7 below shows the boundary conditions for any wall of the geometry.

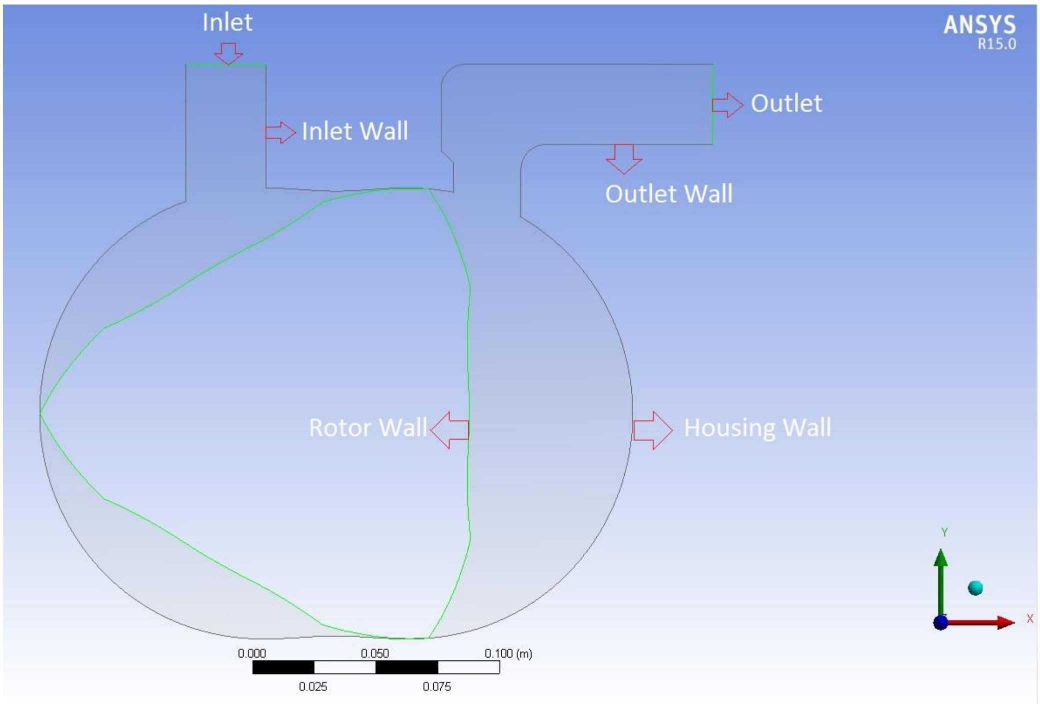

Figure 4.7 : 2D model of engine with intake and exhaust ports.

For comparison between grid quality of the model in different meshing methods, the geometry of the model in 3D also prepare in ICEM CFD program as shown in figure 4.8.

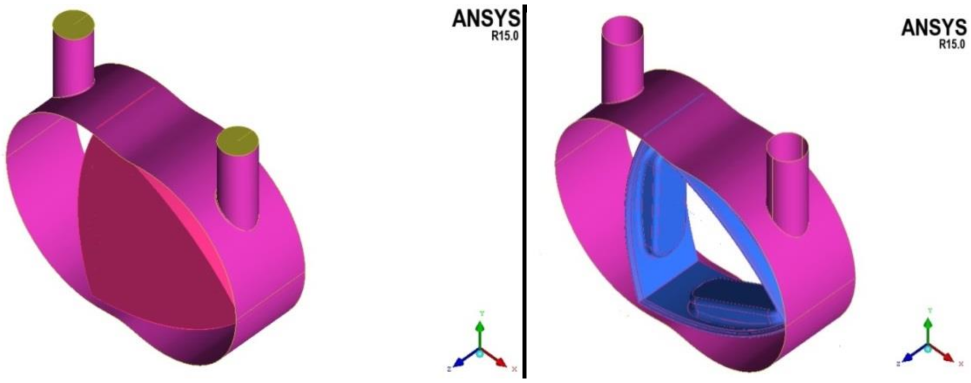

Figure 4.8 : 3D model of engine with and without combustion chamber.

4.6 Grid Generation

Accuracy and duration of the simulation to solve the fluid flow analysis depend on the number and quality of the grid generation. Computational fluid dynamics (CFD) simulations require the computational domain to be discretized into cells so that in each cell, transported quantities are solved with continuity, momentum and energy equations. The optimum mesh size and quality depends on geometry of the model and the method that will be used for simulation.

Meshing the model was done both by ANSYS ICEM CFD meshing program, and also by ANSYS MESHING program under the ANSYS WORKBENCH software. Although using ICEM CFD meshing program gives better results in details and especially in 3D model but the best result was obtained by using the ANSYS MESHING program due to the fast adaptation with model for dynamic mesh. As a result of using dynamic mesh method in this simulation, getting the best suited grid model for having the less skewness and aspect ratio was important. Figure 4.9 shows the grid model generated by ICEM CFD for just one combustion chamber, and figure 4.10 shows the mesh used as the main mesh for simulation.

the gaps. The gap means the area between two different edges on planar surface (10). As it shown in figure 4.11, the number of elements between two edges should be enough for correct calculation while it does not limit the dynamic mesh motion and remeshing intervals. The mesh which applied has maximum of 2 elements between the critical edges.

Because of limitations on dynamic mesh method, our model should have triangular or tetrahedral elements so we could use the remeshing dynamic mesh method. The size of mesh elements are another challenging issue, because both the aspect ratio and skewness factors are important in dynamic mesh through updating the mesh elements. On the other hand, because of the small gap between the rotor end edges and the housing profile, the mesh elements should fill this gap while they could help the simulation of the turbulence fluid flow inside this gap. Adjusting the proximity factor in ANSYS MESHING program controls the number of element layers inside.

The mesh which used in this study has about 23308 node and 44690 triangular elements, with the 0.62 and 2.54 maximum values for skewness and aspect ratio respectively.

The highest value for mesh element skewness stated by FLUENT so it could be used in dynamic mesh method, is 0.9. Skewness that exceeds this limit can result in inaccurate solution and slow convergence.

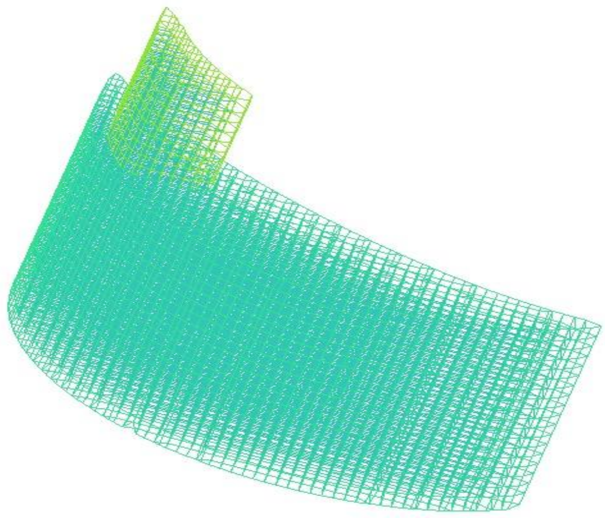

Figure 4.9 : Grid generated for 3D model and intake port using ICEM CFD.

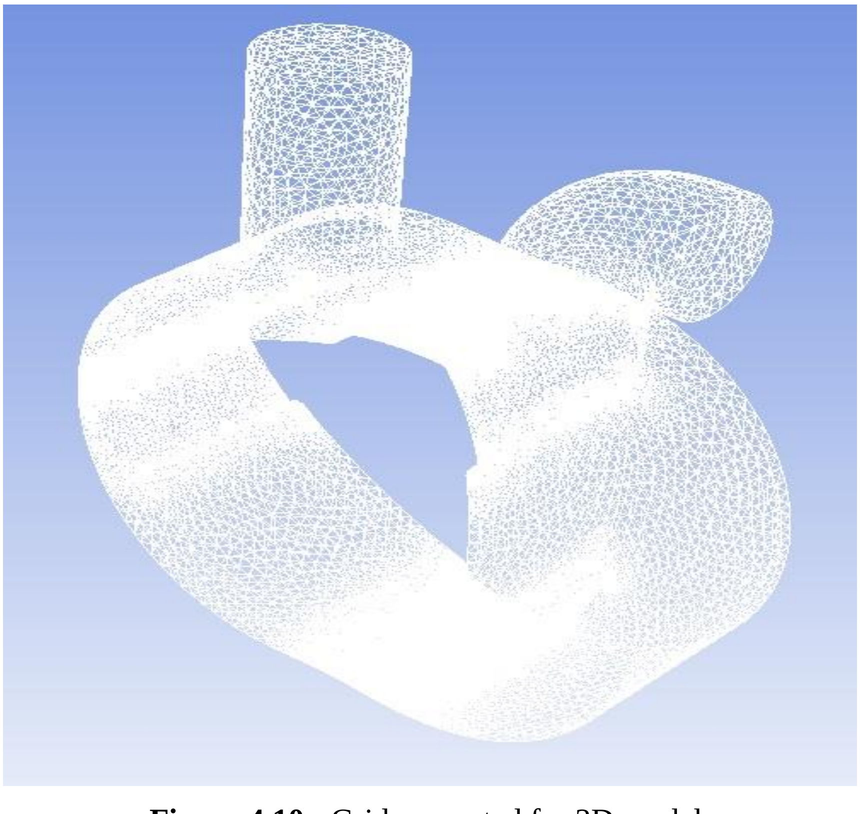

Figure 4.10 : Grid generated for 3D model**.**

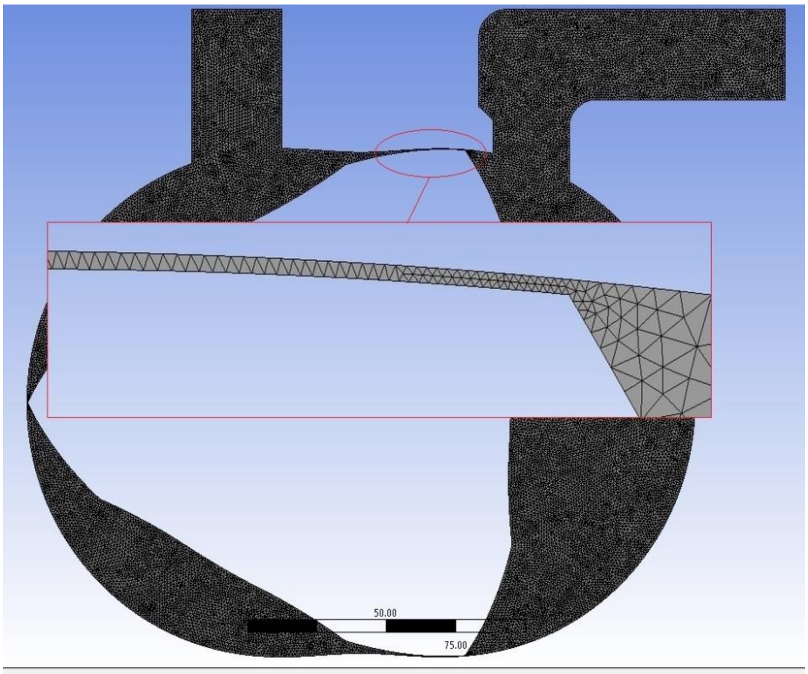

Figure 4.11 : Grid generated for 2D model.

4.7 Mesh Motion

Before starting the fluid simulation, it is necessary to prepare the model for dynamic mesh motion. Mesh motion should check together with the UDF motion profile. Simultaneously, the rotor movement mesh should update and the maximum element skewness should not go beyond one for each mesh element and every time step.

Using the dynamic mesh means that the dynamic parts of the engine that are assigned with meshes, allowed for the boundaries of the cell zones to move relative to other boundaries.

The motion of the cell zone boundaries were governed by a user defined function (UDF). As the cell boundaries move, the interior mesh and adjacent boundary meshes deformed to maintain a consistent grid. The nodes corresponding to the dynamic mesh cells were therefore updated with respect to time.

The rotary engine modeled before, consists of four dynamic mesh zones. The cell zone boundaries that were governed by the UDF included the three rotor faces. The interior volume of each combustion chamber, along with the front and back faces of the housing, deformed according to the pre-scribed motion of the user-defined zones. The inlet and exhaust were stationary zones and thus did not deform.

The meshes in each of the deforming zones were updated using two methods; smoothing and remeshing. The smoothing scheme used to treat the dynamic mesh as spring-based. The spring-based smoothing method treats the edges between mesh nodes as a network of coupled springs with a specified spring constant factor. When the mesh nodes on the dynamic boundaries deform according to the prescribed motion, their edges expand or compresses generating a fictitious spring force on the adjacent mesh nodes. The force generated is proportional to the updated displacement of the boundary nodes along the spring edges. The interior mesh node positions are updated using iterative methods in order to satisfy equilibrium of all the interconnected springs in that zone. The spring constant factor used for this study was 1 with a boundary node relaxation of 1 and convergence tolerance of 0.001. The number of iteration for this method defined as 100.

The spring-based smoothing method is ideal for small boundary displacements relative to cell size. For large boundary displacements however, a local remeshing process is often necessary to achieve a quality mesh. The distinct motion of the rotary engine requires expansion and compression of the interior cell-zones as well as translation and rotation. Spring-based smoothing alone cannot accommodate this elaborate behavior of the dynamic zones, therefore a remeshing method was used in conjunction with the spring-based smoother for updating the mesh. The remeshing process involves examining all the cells in the zone, marking the cells that fail to meet the mesh criteria established by the user, and patching a new mesh over the local area of the marked cell. If the local remeshing fails to generate a better mesh, the entire zone is remeshed. The following parameters listed in table 4.3 were used for the remeshing process of each dynamic zone and indicate the size criteria and desired skewness of the mesh.

Table 4.3 : Dynamic mesh parameters.

Spring Constant Factor	1
Convergence tolerant	0.001
Minimum Length Scale (m) for Remeshing	0.000271
Maximum Length Scale (m) for Remeshing	0.00164
Maximum Cell Skewness	0.7
Maximum Face Skewness	0.7
Size Remeshing interval	1

Dynamic mesh motion requires defining the boundary conditions for any edge or surface. Sınce we use remeshing method, the fluid zone that is defined as deforming dynamic zone, has grid that will be updated in any time step. On the other hand, the edge of the rotor also rotates while the simulation runs and the nodes on the rotor edges, update their position in any time step. The reason of putting small gap between rotor and housing profile is explained due to this. Since the rotor edge is deforming rigid body, while the hosing boundary condition is stationary, then the rotor points cannot lay on housing profile simultaneously. It means that one node cannot be as the stationary point while it should be updated during simulation. As it explained in literature review part [34], for the cases in which we want to simulate whole the combustion chamber without leakage while it is in contact with housing profile, at least we should define another region for fluid that has high viscosity or porous region with laminar fluid flow, at the back of housing profile.

The UDF file that used for dynamic mesh motion in our study has two different formats. In any of them, the rotor rotation speed is different from the other one so we could simulate the rotor motion with two speeds. In the first UDF, the rotor is rotating with 1000 RPM, while in second one the rotor is rotating with 3000 RPM.

4.8 3D Model Study

As the first aim of this study, the Wankel rotary engine assumed as 3D as like as its real model. All the modeling and grid generation works done also on 3D model parallel to its 2D model. The modeling of this study on 3D has done by extruding the 2D model at first. The base profile of the rotor and housing extruded as 80 mm at first. Applying the grid generation on this model also had done using ANSYS MESHING program successfully. Mesh motion and UDF method applied and the initially meshed model could successfully run while the FLUENT program runs the simulation. The only problem was the time required by the computer to simulate this model. Although the computer used for this simulation has core i8 motherboard system with 4GB base RAM, but the simulation takes about 24 hours for just about 30 degree of rotation. Furthermore, the model does not have any port yet and runs with laminar fluid method. Other models also tried for 3D simulation.

By attaching the intake and exhaust ports to the geometry, the simulation became much more complicated. When the rotor edges reach the ports geometry, due to huge differences in pressure gradients, the program needs much more memory to analyze the model. Designing the ports on side part also tried in this study. Due to the continuity principle of the program, the fluid flow was not able to cut the fluid while the rotor passed through the ports designed on side part. Another approach tried so the thin layer of the fluid always exist between the rotor side and housing side part, in this case the continuity problem was solved but on the other hand, when the rotor passed through the ports, the high pressure gradient requires higher memory for calculations.

Figure 4.12 – 4.14 shows different approaches tried during this study to solve the mesh motion problem while the rotor rotates inside the housing. As seen in figure 4.12, in this model the ports attached to side surface of the housing with the real position of Mazda engine.

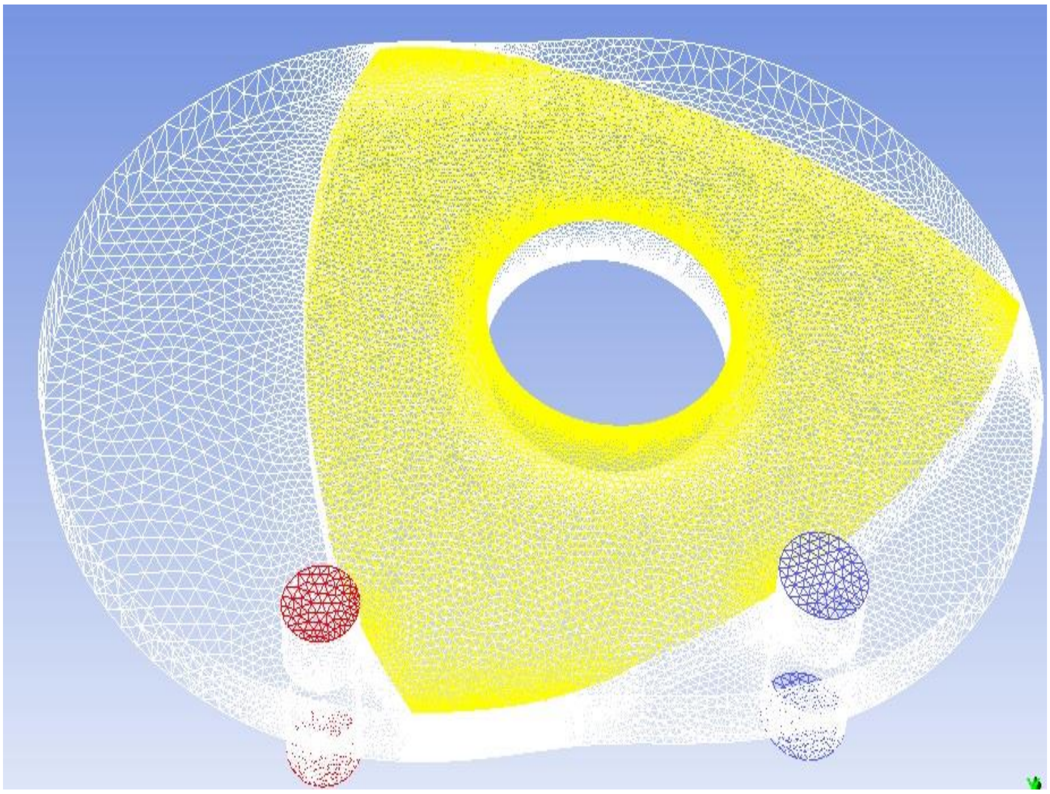

Figure 4.12 : 3D model with thin layer of fluid on side.

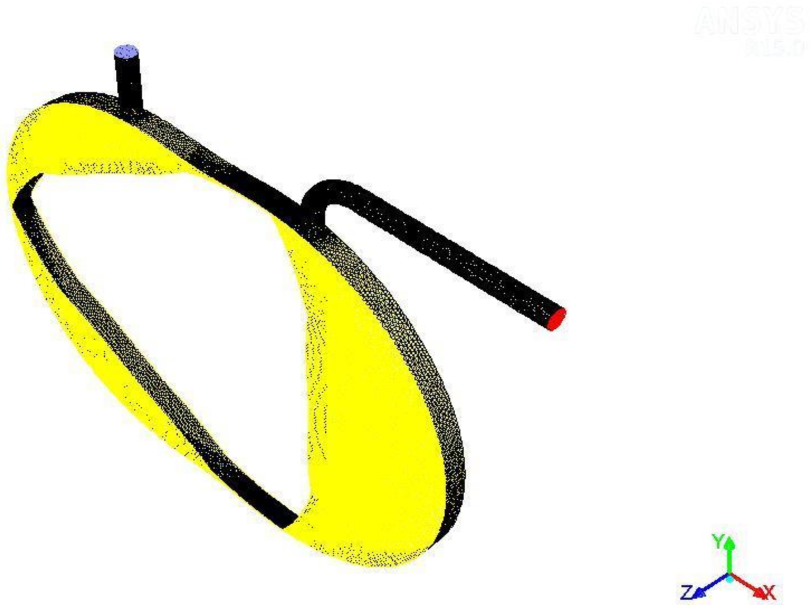

Figure 4.13 : 3D model with ports installed on housing profile.

4.9 Numerical Methods

As it stated before, the FLUENT uses finite volume method for solving the physical equations of continuity, momentum and energy. There are two different methods for solving these equations in FLUENT, i.e. pressure base and density base. Since in pressure base method, FLUENT uses the pressure correction equations that obtained from momentum and continuity equations, we use pressure base for our method. This method is well known for incompressible and compressible flows. Pressure base method based on two algorithms, segregated and coupled methods that are different on solving the equations separately or simultaneously. Solving with coupled algorithm results in better and earlier convergence than segregated method.

There are different parameters for discretization in FLUENT solver. Using pressure base method requires defining averaging parameters for pressure and density also. As a general, if the fluid flow be in the same direction of the grid system, using the first order upwind is better, while for the other cases that grid system is not in same direction, i.e. triangular meshes, using the second order gives better results. First order upwind method has better convergence than second order, but less accuracy than second order.

For the conditions that the flow has high Mach number, it is better to start the simulation with first order method and after obtaining the convergence, switch the method to second order.

For pressure interpolation, in most cases the standard method gives good results. For the cases with higher volume forces, the method of body-force-weighted is better and for the cases with high swirl numbers, rotational flows or flows in porous regions, using the PRESTO method for pressure interpolation recommended.

For density interpolation, we can use four different methods. In most of the cases, the first order upwind method could give acceptable results. It also gives good results for pressure correction equations. Nevertheless, for the flows with shocking, it is better to use second order method so the effect of shocking does not ignored. Using the QUICK method also gives good results for these cases. The method MUSCL is also usable in any of the cases.

There are also different methods for coupling the pressure and velocity in pressure based solving method. The methods SIMPLE and SIMPLEC are most often chosen for steady conditions, while for the unsteady or transient conditions, PISO gives better results. Furthermore, for steady or transient conditions with diagonal grids, PISO may give the best results.

By using the PISO method, there are two options, neighbor correction and skewness correction. Using the PISO method with neighbor correction is best suited for transient flows with large time steps. Using the PISO method with under relaxation factors of 1 for pressure and momentum, gives good results. For the conditions with diagonal grids or high skewed grid systems, using the PISO method together with skewness correction option, for both the steady and transient flows is recommended. If we use skewness correction option without using the neighbor correction one, it should be noticed that the total of under relaxation factor for pressure and momentum should be equal as one.

For the gradient option, there are three different methods, Green gauss cell based, which calculate the derivatives from the averaging the related value from adjacent cells, Green gauss node based which calculate the derivatives from averaging the related value of the nodes on one cell, and it has much more detailed results than the first method specially in triangular elements, and the last method named least square cell based which uses the linear definition of derivative due to least square method.

There are also some under relaxation factors that should be defined before the simulation starts. These factors are defined due to comparison of calculated values of any parameter with its previous calculated amount. In most of the cases, there is no need for changing the default values, but for the cases with turbulent fluid flows, it would be better to adjust these parameters. If the solution with default values does not converge after some iterations, the under relaxation factors should be reduced for pressure, momentum, k and Ɛ.

Initializing the solution before the simulation estimates the initial values before the simulation runs. As much as the initializing becomes more and more accurate, the simulations give us detailed and correct results.

Simulating the turbulence fluid flows requires estimating the parameters for the k and Ɛ if we use the model k-Ɛ. In this model, the solution should not depend on the first estimated values of k and ε. So it is always recommended to start the calculation after the flow became turbulence and using the enhanced wall treatment. It is normally consider the 5% - 10% of turbulence intensity.

4.10 Setting the Solver

Setting the solver for our simulation was done considering the critical geometry and fluid flow inside it since the dynamic mesh motion has lots of limitations such as lower time step for mesh updating.

The following boundary conditions and initial conditions in Table 4.4 were used to setup the engine simulation. For intake, normal room temperature was used to represent the cold air into the chamber.

FLUENT program runs in 2D mode, since we would like to do our simulation with 2D model. General mesh checking process done without any negative volume detected. The solver runs in Pressure based type with transient mode. Because of the gravity acceleration, we define the Y direction gravity as -9.81 (m/s^2).

Table 4.4 : Boundary and Initial conditions used in FLUENT.

Boundary Conditions		
Intake	Pressure	101325 (Pascal)
	Turbulence method	Intensity and Hydraulic diameter
	Turbulent intensity	1%
	Hydraulic diameter	0.032
	Total temperature	300 (k)
Exhaust	Pressure	101325 (Pascal)
	Turbulence method	Intensity and Viscosity Ratio
	Turbulent intensity	5%
	Backflow Ratio	10
	Total temperature	300 (k)
Wall	Housing wall	Stationary Wall – No Slip
	Rotor Wall	Rigid body Wall with movement
	Inlet wall	Stationary Wall – No Slip
	Outlet wall	Stationary Wall – No Slip
Initialization	Operating pressure	0
	Temperature	288.16

The models that we use in our study are both laminar and turbulent models. For turbulent one, energy equation activated and the viscus model, chosen as K- ε with 2 equations. Because of the more accuracy, the realizable method selected for this turbulent model. Fluid flow treatment near the wall is analyzed with standard wall function. The material that we use as fluid is air as an ideal gas. Operation conditions defined as zero pressure with 288(k) temperature and zero operating density.

Solution method that used in this study is PISO scheme for pressure-velocity coupling, without any correction. The discretization methods for momentum, turbulent energy and turbulent dissipation rate is first order upwind, while for momentum and energy, second order upwind chosen. Solution initialization done with hybrid method so the pressure distributed as in whole the combustion chamber in static mode before the simulation starts. Our calculations done with 2e-6 (sec) for time step size since the dynamic mesh is sensitive to higher time steps and could not update the mesh correctly.

4.11 Applying the UDF

As it explained before this in theory part, for updating the mesh grids the dynamic mesh should use UDF. The UDF, which used in this study is DEFINE_CG_MOTION, which is standard MACRO of the FLUENT. The UDF file should prepare for the model before it compiled to FLUENT. UDF files written in C language, and can edited with VISUAL STUDIO programs. The standard format of the UDF we use is as below:

```
"DEFINE_CG_MOTION(rotor, dt, vel, omega,time, dtime)

{

NV_S(vel, =, 0.0);

NV_S(omega, =, 0.0);

vel[0] = -beta*r*sin(beta*time);

vel[1] = beta*r*cos(beta*time);

vel[2]= 0;

}"
```

Each of the rows here is in standard form of the DEFINE_CG_MOTION UDF. First row of the code is to call the MACRO from FLUENT library. It means that this UDF will use for the motion of the center of the gravity with the linear velocity in dt of time. Second and third rows are used to restart the MACRO in any time step. Linear velocities here defined by vel[1], vel[2] and vel[3] as the velocity in x, y, and z directions. As it seen here, due to the 2D rotation of the rotor, velocity in z direction is zero. For velocities in x and y direction, as we know, the point on rotor edges are moving as 3α while the CG of the rotor moves as α. Due to this, the angular velocity of the rotor edges are defined as beta. If we assume that after the time of dt, new location of the points are defined as:

$$\begin{cases} x = r.Cos\ (beta * time) \\ y = r.Sin\ (beta * time) \end{cases} \quad \textbf{(4.5)}$$

Then the velocity of the point, which moves during the time, dt, calculated as:

$$\begin{cases} \dot{x} = -beta.r.Sin\,(\,beta * time) \\ \dot{y} = beta.r.Cos\,(beta * time) \end{cases} \tag{4.5}$$

These equations could be used as linear velocity for any points on rotor edge with the coordinates of (x, y).

The only point that should be noticed is to define the value of eccentricity by the following command, so the code could recognize the CG of the rotor:

```
#define r /*eccentricity*/
```

4.12 Model Validation

As it explained before this, we use different 2D models for comparing the simulation results. Validation of these models should be done to see if there is any change needed for model change or not.

The models that we use in our study are 2D Wankel engine without any recess, with recess in middle of the rotor edge, recess in left and right part of the rotor, and also new designed recess by author. Figure 4.14 shows different models we used:

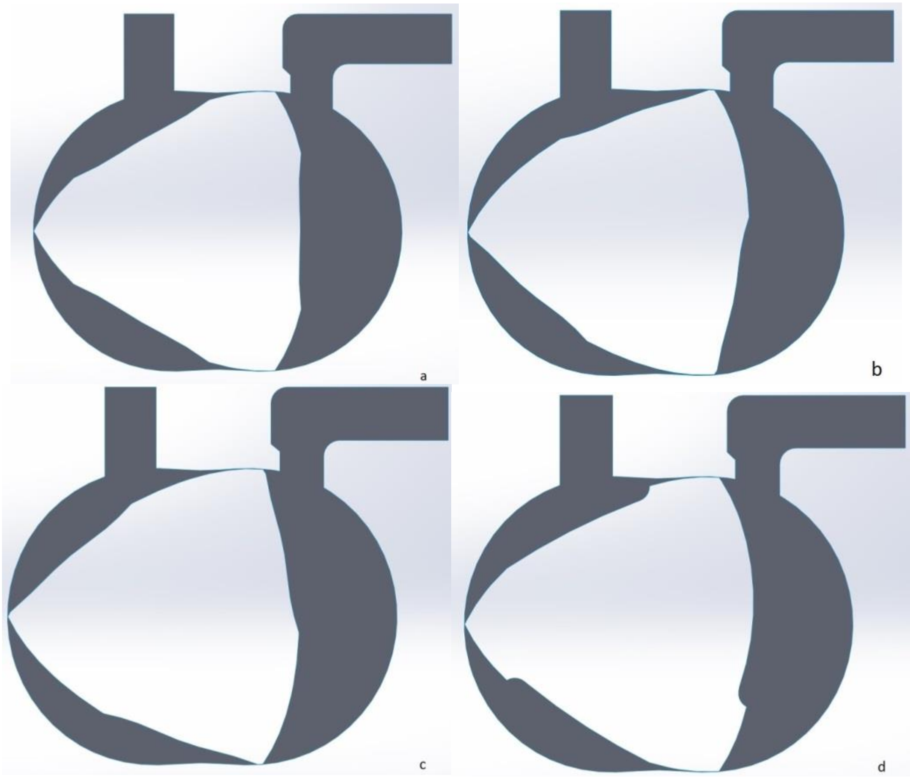

Figure 4.14 : Models with different recess positioned geometry.

For validating these models with our references, the best parameter is to compare them with compression ratio. The significant factors in designing the rotary engine are eccentricity, radius and the maximum and minimum values for rotor inside the housing. According to the Ansdale (11), the relationship between R, e and Ø as the angle of sealing part, is given by:

$$Sin\, \emptyset = 3\frac{e}{R} \quad \textbf{(4.6)}$$

The number 3 shows the number of corners or contacts between the rotor and the respective bore or the number of chambers. The complications arise because Ø has also determining effects on the highest possible compression ratio. Figure 4.15 shows the relationship between maximum angle of leaning angleØ, swept surface area and maximum compression ratio respectively.

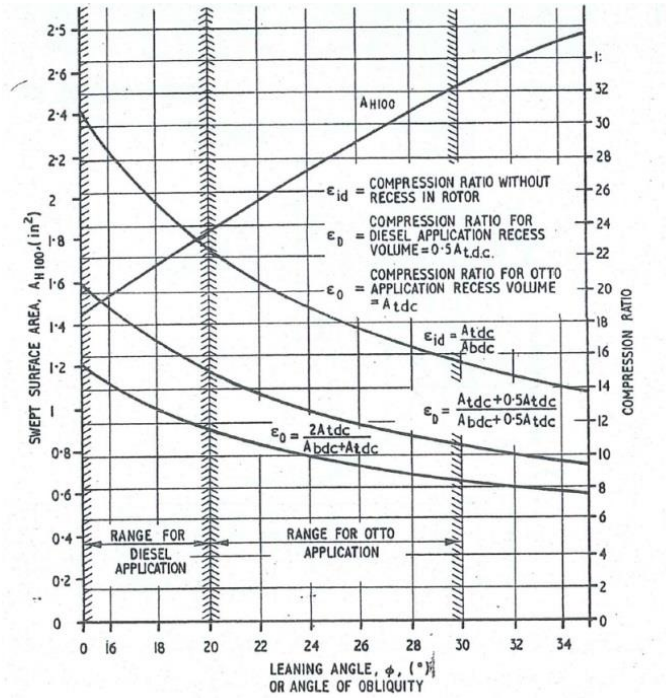

Figure 4.15 : Compression ratio vs. leaning angle (Ansdale,1981).

The following table 4.5 shows the critical parameters for our models:

Table 4.5 : Main parameters for the models used.

Model\Parameter	Maximum Vol. (mm^3)	Minimum Vol. (mm^3)	Compression Ratio
Without Recess	695460	41922	16.59
Recess in middle	734400	81130	9.05
New designed Recess	735561	82022	8.96

According to Ansdale graphic, for our models with $\emptyset = 25.3724$, the compression ratio for the model without recess should be about 18.

The reason of this small difference is due to the small gap we use between rotor and housing profile. This value of 0.2 mm for gap is like shifting the profile as 0.2 mm. As we know the rotor edge is about 187 mm, the area of 187*0.2= 36.2 mm is the area which was ignored due to the shifting. If we add this value for both the minimum and maximum volumes, the compression ratio would be the same as graphic value that is eighteen.

5. RESULTS AND DISCUSSION

Cold flow study helps to understand the tumble motion of air inside the chamber and therefore we can estimate the mixture formation. In cold flow study, the following aspects are considered.

1. Fluid flow paths and velocity magnitudes inside chamber

1. Turbulence of air in the chamber

2. Maximum temperature and pressure at TDC and detecting critical points

Estimating the highest pressure and temperature zones inside combustion chamber will help the engine designer to get the best performance of the injection and ignition. The fluid path and velocity vectors are both important for mixture formation and mixture distribution. Furthermore, as we know, turbulence kinetic energy (TKE) is the mean kinetic energy per unit mass associated with eddies in turbulent flow and Turbulence Intensity is measurement scale characterizing turbulence expressed as a percent. An idealized flow of air with absolutely no fluctuations in air speed or direction would have a Turbulence Intensity value of 0%. Therefore, turbulence of the air in the cylinder is a very crucial for formation of fuel and air mixture. The study of turbulence in the cylinder will explain the behavior of air charge in the cylinder and the starting time and positions of the turbulence flow, which could be a good estimate for starting the ignition. This aspect is very important as it decides the injection duration and injection start for the next studies that will change the four-stroke engine to two-stroke diesel engine.

The results obtained from this study divide to different parts, concluding the comparison of the results for the models working with lower speed, comparison between the same geometry models with different engine speed, and results obtained for different geometry models simulated under the same engine speed of 3000 RPM.

5.1 Modeling the engine working at 3000 RPM

When the engine is working on 3000 RPM, the engine is not under full load. In our study, this results in slower rotational speed of the rotor, so the fluid inside the chamber has much more time flowing inside the chamber in comparison with the 9000-RPM model.

5.1.1 Different Recess Position effect on Pressure Distribution

When the rotor is at its TDC position, for the model that recess is positioned in middle of the rotor edge, the pressure distribution is homogenous, and reaches at maximum twelve bars. For the models that have recess on any edge end of the rotor, the pressure distribution is not homogenous. For the model with recess on its right side, since there is a narrow area for the fluid to passes through, the pressure difference about eight bars could be seen between two regions inside chamber, which is due to the lower velocity while the fluid passes through that narrow area and lower velocity magnitudes in the front area. For the model with recess on its left end, the pressure distribution divided into two different zones, in second region, due to the wider area in middle of the recess, and lower pressures on its end zones due to the lower speeds. Figure 5.1 shows the pressure distribution for various recess models at 3000 RPM.

5.1.2 Different Recess Position effect on Temperature Distribution

Temperature distribution is also under the effect of the recess position when the engine is under 3000 RPM load. As like as the pressure, recess positioned in middle results in homogeneous temperature distribution in combustion chamber when the rotor is at its TDC. On the other hand, for the cases that have recess on any end, it is not homogeneous and in some regions, the temperature increases considerably. This happens almost at the zones that have wider area between rotor edge and housing and for the regions that is too much narrow. This high temperature zones could help to have the early combustion zones in this chamber, and could be a good candidate for injection considering the other important factors. Figure 5-2 shows the temperature distribution at TDC. As it seen, symmetric recess model has homogenous temperature distribution. The temperature range for all the models are between 600 and 700 degree of kelvin, while for the models that recess positioned on any end edge of the rotor, there is a zone inside the chamber that temperature reaches to its highest value. The effect of the fluid flow that passes through the rotor end tips could be seen here obviously. As the result of lower rotational speed, temperature distribution for the next chamber that is at compression phase, is under the effect of this fluid flow and there is difference on temperature inside the chamber between 290 and 550 degree of Kelvin. Another significant point is the vacuum flow that is from outlet of the model, which is also due to the rotor tips non-sealed model. For the symmetric middle recess, this vacuum effect could be seen obviously.

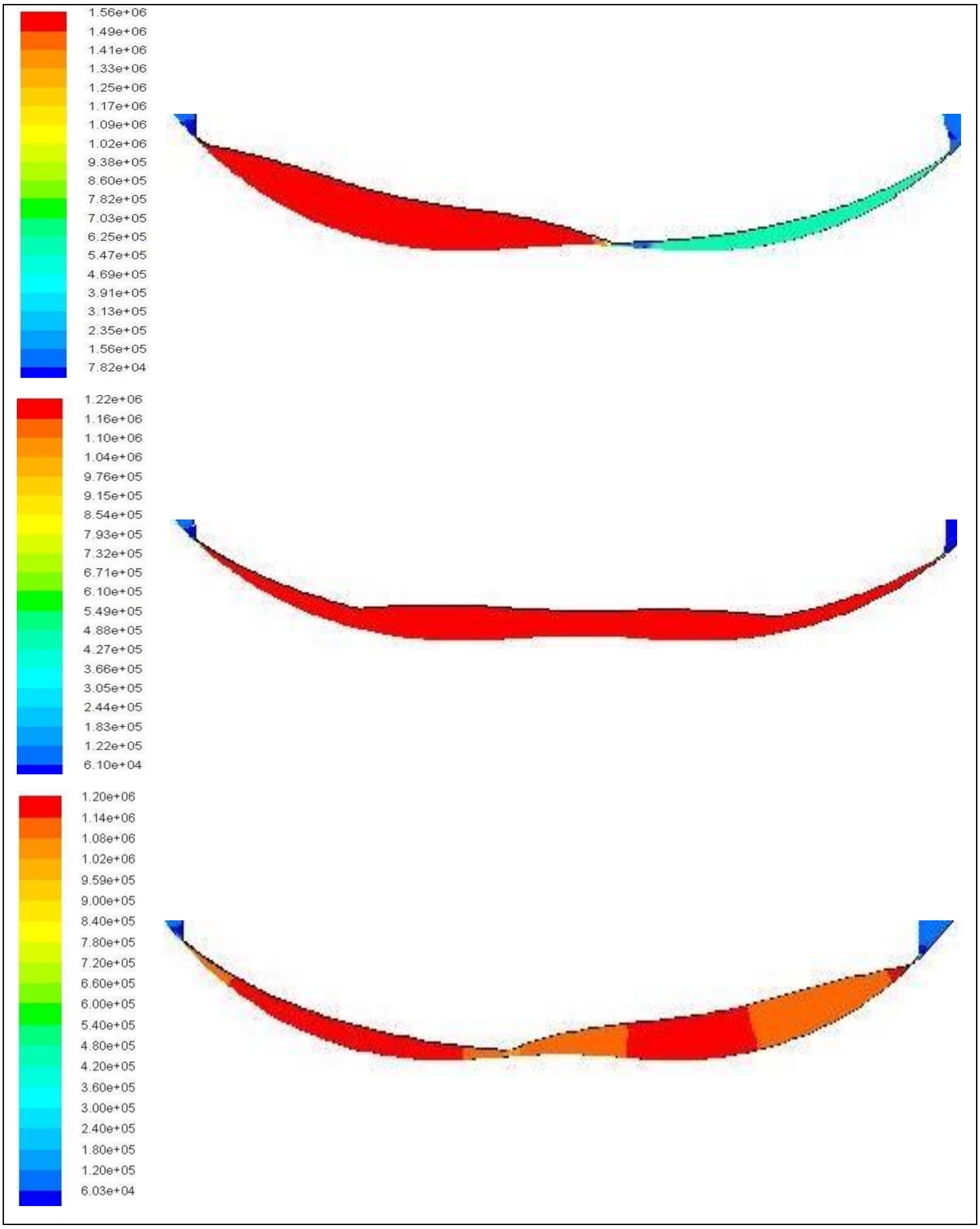

Figure 5.1 : Effect of recess positions on pressure (Pa) distribution, TDC.

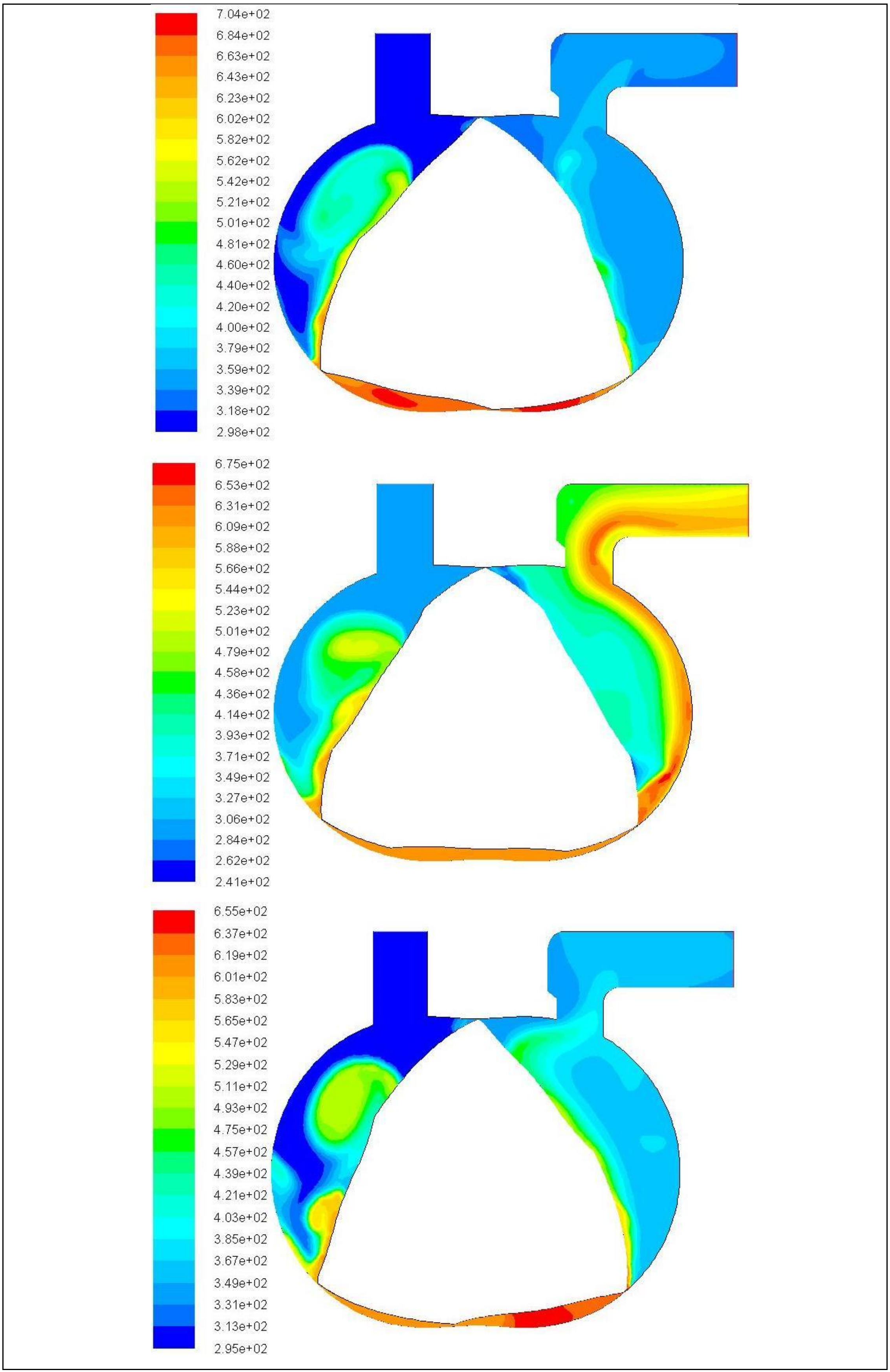

Figure 5.2 : Temperature (k) distribution, TDC, 3000 RPM models.

5.1.3 Different Recess Position Effect on Turbulence Energy

Turbulence energy is not that much affected with the recess position while the rotor is at TDC, but the fluid flow which ran out of the combustion chamber, has different attitude for these models as it seen from figure 5.3.

As it seen, turbulence kinetic energy has very low values when the rotor is become more and more near to TDC. For the first picture that has the recess on its right side, the empty zones in this picture referred to higher energy values that are out of the scale. For the right positioned model, the empty zones in front of the recess has kinetic energy of 60 m^2/s^2 and for the zone just beside the narrowest area, this value reaches to 2500 m2/s2, that is due to the high velocity magnitudes. For the model that has recess on its middle, on rotor end tips, we have turbulence kinetic energy around 1900 m2/s2 that is also because of fluid flow ran out of the main chamber to other combustion chambers. Figure 5.3 shows the turbulence energy distribution at TDC.

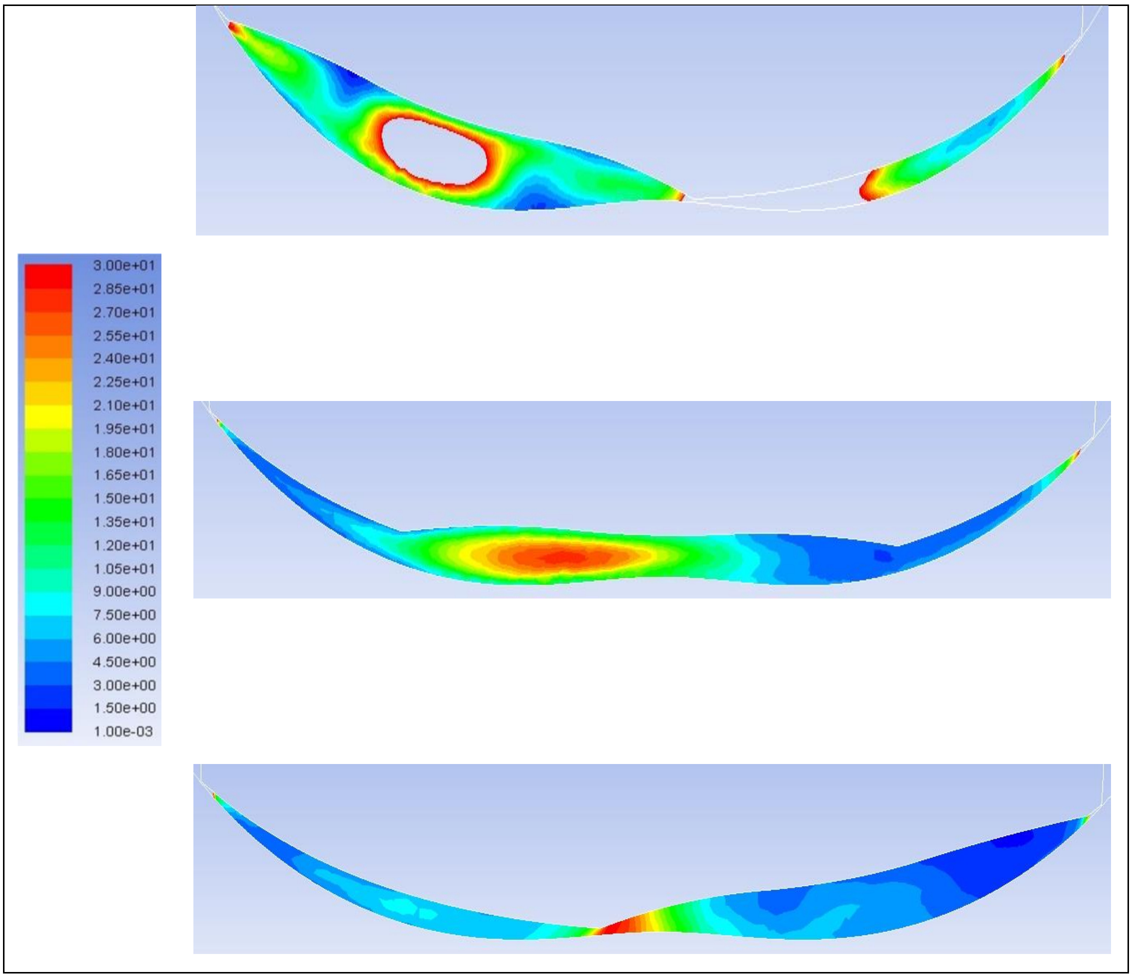

Figure 5.3 : Turbulence energy (m^2/s^2), TDC, 3000 RPM models.

5.2 Modeling the Engine Working at 9000 RPM

For our study, due to the non-sealed rotor end parts, there is always fluid flow that ran out of the chamber with higher pressure to the chamber that has lower pressure. Increasing the rotational speed for the rotor results in less time remain for the flow to ran out of the chamber and this effect the simulation results. In this part, we will study the results for the model that is rotating with 9000 RPM.

5.2.1 Velocity Analysis

In this part, velocity magnitude and velocity direction of the flow inside the chamber will be studied.

5.2.1.1 Flow path comparison between the models

As it seen from the figure 5.4, the circulation flow starts near the recess edge start point and rotates clockwise upward near the fixed sidewall. This circulation starts from the early time steps and shrinks as the rotor tip become closer to inlet port end. Under the effect of these circulations, the flow directed again to first half of the room, while when the swirling does not happen, the inlet flow directed towards the other edge of the rotor where due to a non-sealing effect, the flow passes to other combustion chamber. The effect of designing the recess on left end edge of the rotor while the engine is working under 9000RPM has the result of reverse flow in inlet port, as it seen in figure above.

The recess geometry has not much affected the inlet flow velocity, but for the non-symmetric recess design and also recess positioned in any end of the rotor edge, the velocity is a bit higher than the other models. Figure 5.4 shows the inlet flow paths.

5.2.1.2 Velocity analysis during the compression phase

Figure 5.5 shows the flow velocity after the tip passed the inlet port, which means that the inlet port is closed and the compression cycle started. All what can be seen on this is that the flow vectors are in most cases have two swirling area. Near the rotor tip end, the flow is still moves directly in the same engine rotation direction, taking the flow coming from the chamber with it.

Except the model that has standard recess in middle, for other models there are two rotational areas for velocity vectors. For the case with deeper non-symmetric recess, there is also small swirling area in recess deepest part. This swirl flow continued during the compression cycle until the distance between the rotor and the engine housing become very small, before the engine TDC, and then the flow will take the same engine rotation direction.

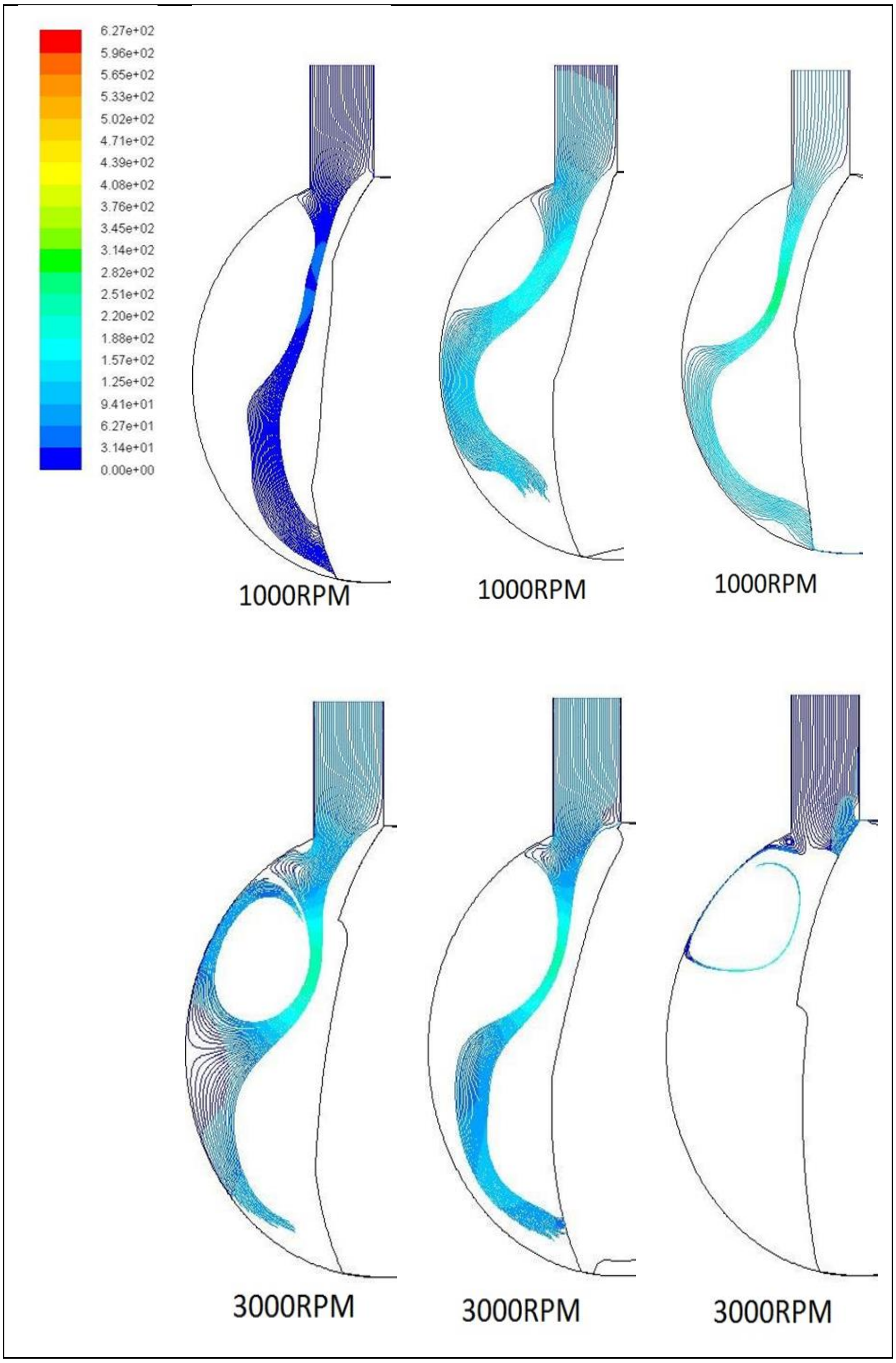

Figure 5.4 : Inlet flow paths comparison.

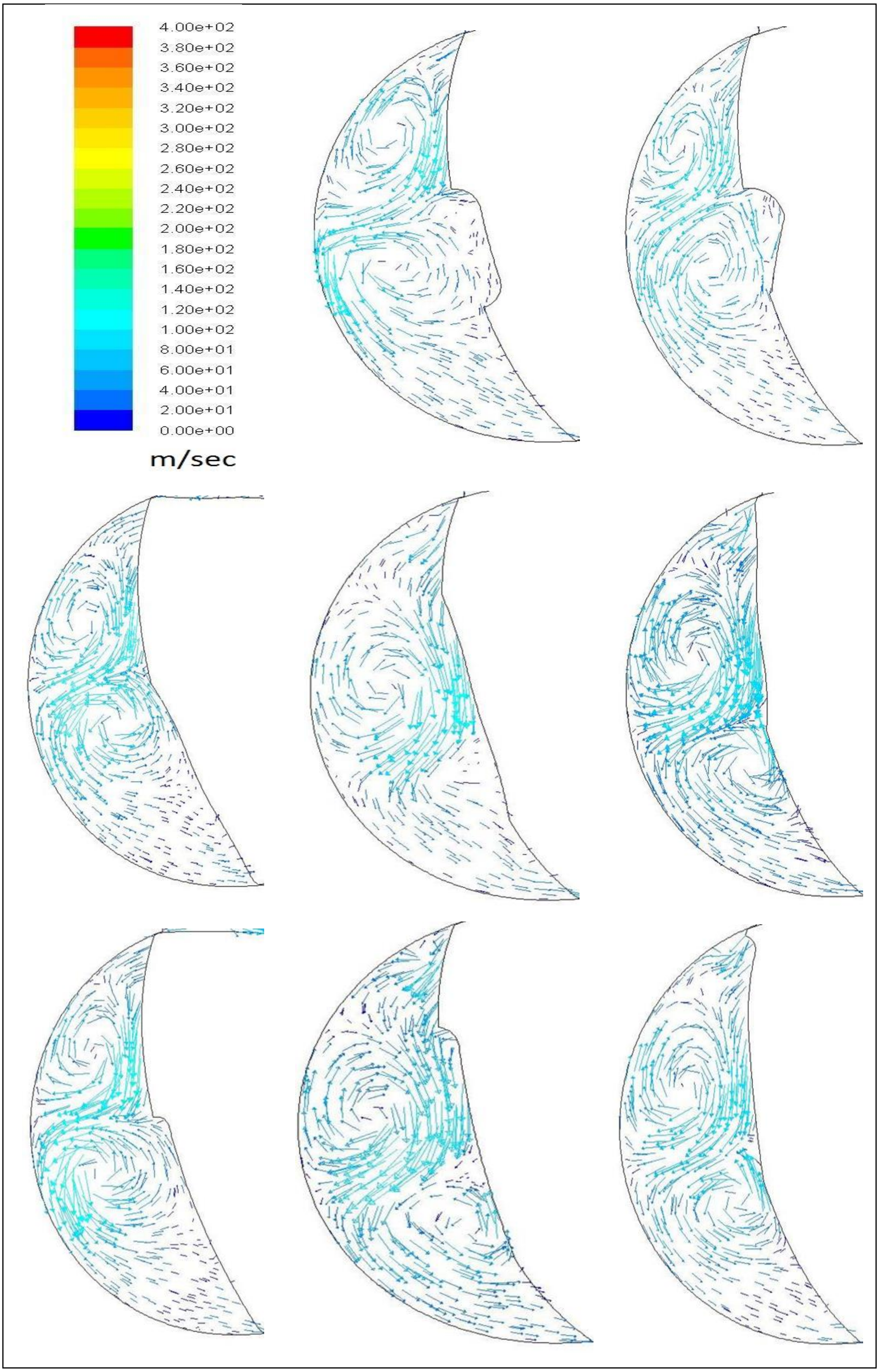

Figure 5.5 : Velocity vector directions, compression phase, 9000 RPM.

The velocity magnitude for compression stroke starting is as shown in figure 5.6.

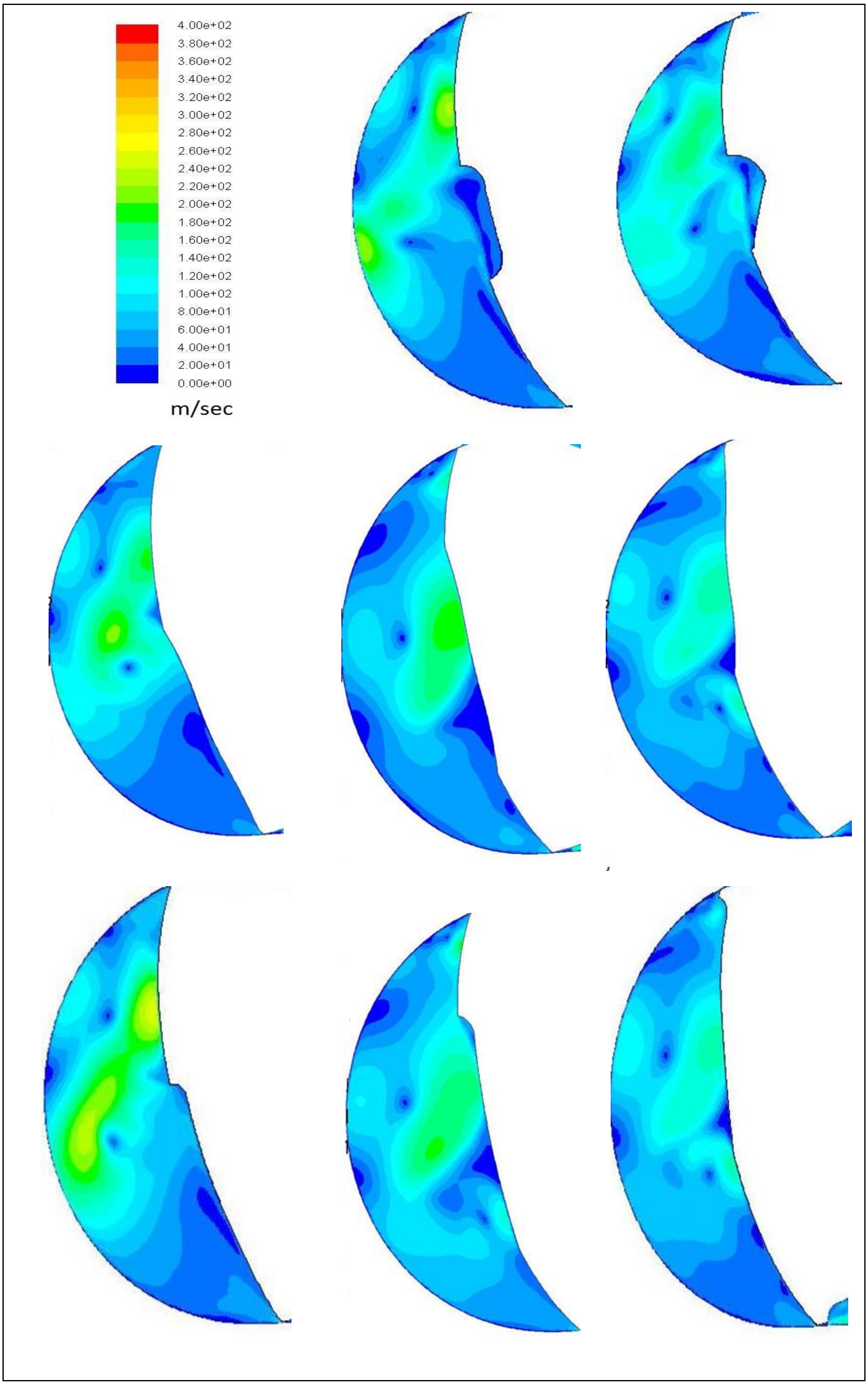

Figure 5.6 : Velocity magnitudes, compression phase, 9000 RPM**.**

The maximum velocity during the inlet phase is for the condition that non-symmetric recess is located on left end of the rotor and the rotor tip passed from port, that velocity reaches 120m/s.

During the compression phase, the fluid flow velocity is about 100 m/s in some zones of the whole domain, as only the rotor movement drives it and there is no inlet flow accelerated the flow velocity.

Port or low-pressure fuel injection has more time for mixture preparation, and the creation of swirl or tumble inside combustion chamber will give a better chance for fuel to be mixed properly with air and gives better or complete fuel combustion, and hence less pollutant products.

5.2.1.3 Velocity analysis at TDC

When the rotor becomes closer to the end of compression phase, the rotor divides the flow domain into two chambers. The leading chamber zone is at the leading part of the rotor (the chamber after the housing tip, short axis) and tailing chamber zone at the tailing part of the rotor (before housing short axis). The tailing chamber has a relatively higher pressure and hence the flow velocity between these two chambers becomes high depending on the rotor recess depth and engine speed. Figure 5.7 shows the velocity magnitudes at TDC for various models.

The difference on velocity vectors while the rotor is in its TDC position is shown on figure 5.8.

The swirl flow has less effect on high-pressure fuel injection when the fuel is injecting near the engine TDC as the ignition is normally start shortly after fuel injection, but the swirl that can affect and improve the turbulent combustion was not clearly noticed at TDC.

These simulation results shows that the Wankel rotary engine develops a swirl or tumble vortex inside the combustion chamber along the flow domain during inlet and compression periods and that will very useful for port or low-pressure injection if the fuel is injected directly into the swirl vortex. A good mixture concentration distribution expected, if the fuel injected directly to the swirl vortex just above inlet.

Due to these results, we can say that in Wankel engine, even if the air/fuel mixtures is well prepared, there is another factors drawback the combustion process, such as the long and narrow combustion chamber.

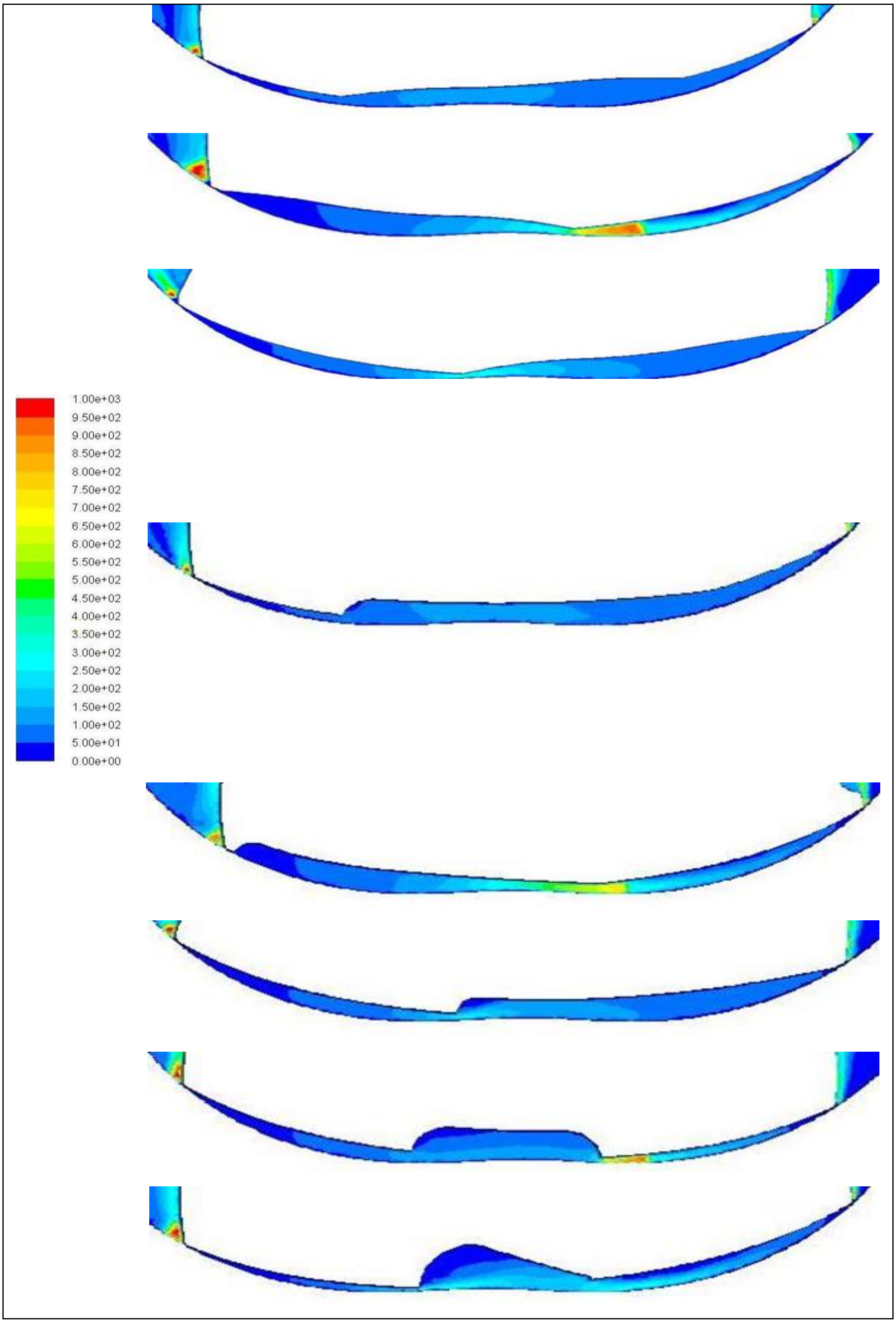

Figure 5.7 : Velocity magnitudes, TDC, 9000 RPM.

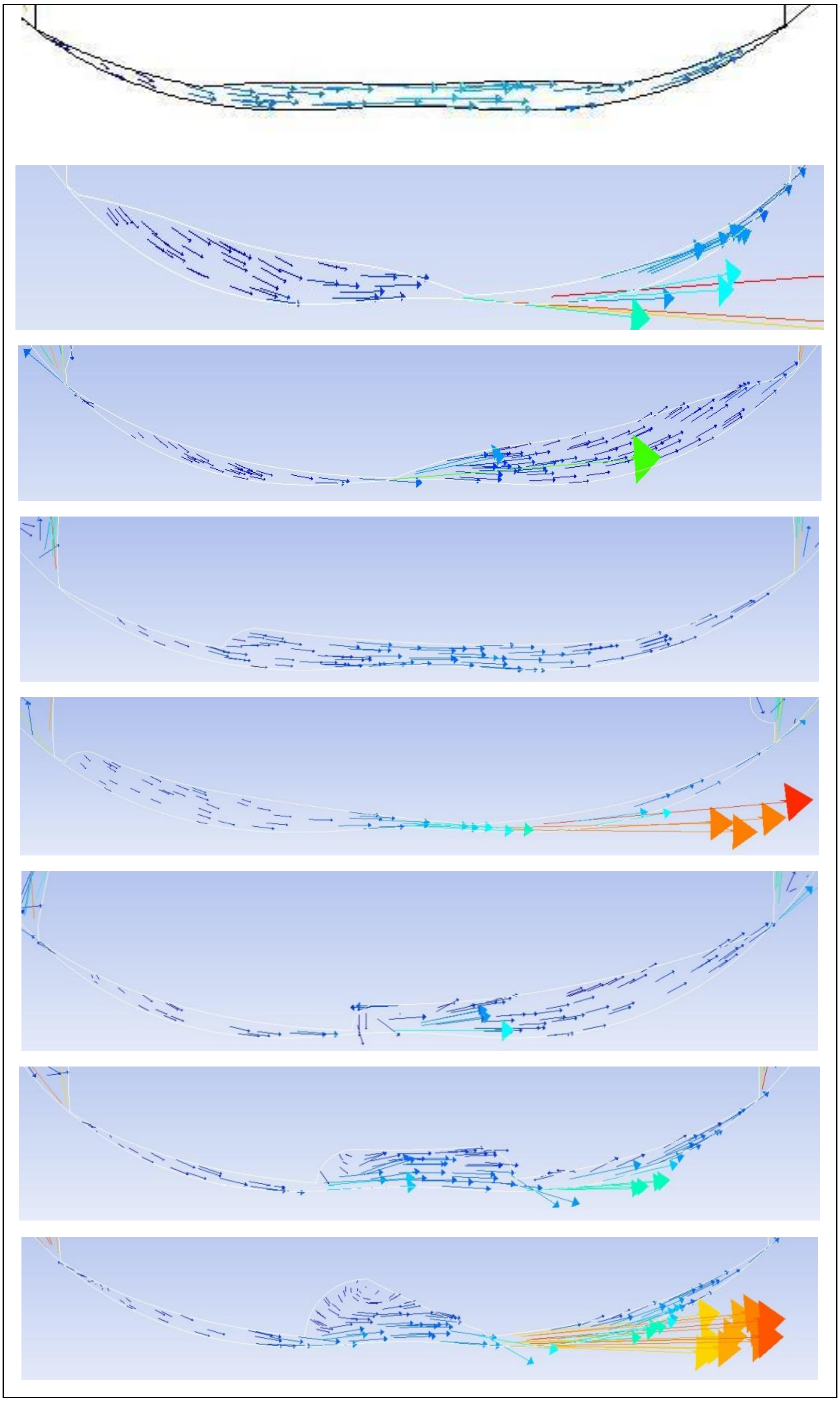
Figure 5.8 : Velocity vector directions, TDC, 9000 RPM.

The CFD simulation shows that, the swirl vortex become smaller and smaller until the flow takes rotation direction near TDC with higher flow velocity at the housing mid-point, where the distance between the rotor and housing is very close. Normally when fuel is injected at engine high pressure, the fuel injector is fitted at the housing mid-point, (short axis), and inject fuel at this point where the flow velocity is very high, that will accelerate fuel to one side of combustion chamber or to the narrow end. To avoid such action, it is necessary to reduce flow velocity at this point by increasing the recess size.

5.2.2 Pressure Analysis

5.2.2.1 Pressure analysis during the compression phase

According to results obtained, the pressure distribution on compression does not change that much when the recess geometry change. The only significant difference refers back to the model that recess positioned on end edge of the rotor. For this model the, maximum pressure reaches at about 2 bars in inlet port. Figure 5-9 shows this difference, and the difference with non-symmetric deep model.

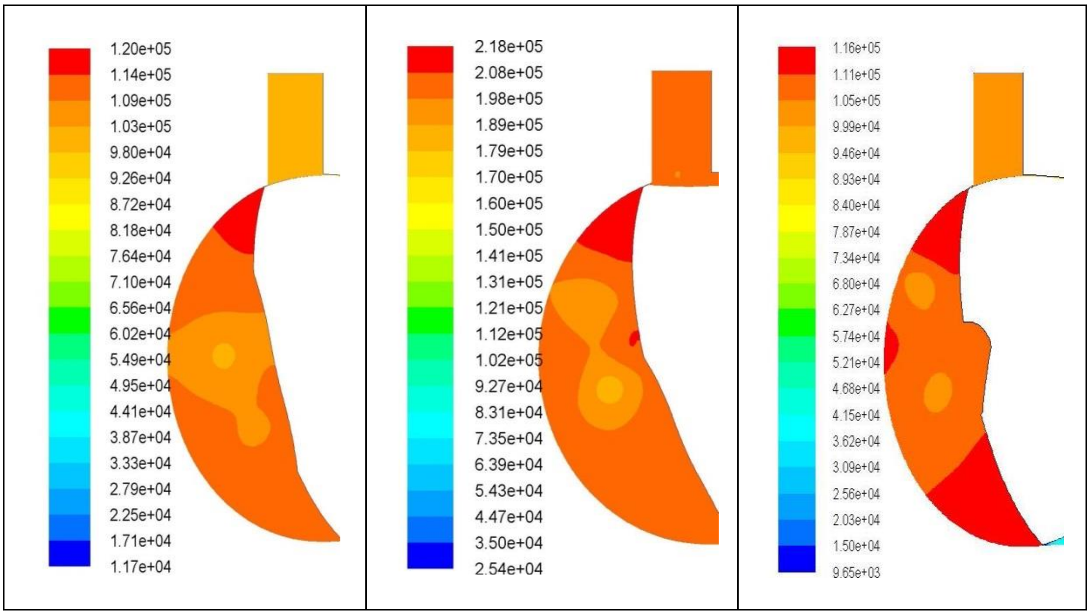

Figure 5.9 : Pressure (Pa) distribution, compression phase, 9000 RPM models.

5.2.2.2 Pressure analysis at TDC

The total pressure is displaying in figures 5-10 for different engine models. However, a different scale is used to make the display more clear. The total pressure difference between the leading region and the tailing region is higher on the rotor with recess positioned in middle than that with recess on any end edge of the rotor. The rotor with non-symmetric recess in end edge of the rotor has reach the highest pressure about 40 bars due to the narrow path for fluid passing through the recess end edge and housing profile, that is due to the high value of velocity. It should be noted that this value is just because of the geometric model and is just in few time steps that rotor passes from TDC.

By comparing the models with symmetric standard recess and non-symmetric model, the difference between the two regions and the pressure concluded. This is clearly, because this rotor model has a difference in area distribution along the rotor edge. Another significant point on this analysis is for the deeper recess models. For the model for the non-symmetric recess, there is difference between two regions as seen in figure below. The pressure distribution on end edge of the rotor is about 12 bars while for the symmetric deep rotor it is much higher about 20 bars on the same region.

The rotor movement and the pressure difference at this position create the flow velocity and the lower pressure difference creates a lower velocity at the housing tip separating the two regions. In order to reduce the flow velocity at this position, it is important to increase the rotor recess width and/or depth on the penalty of compression ratio reduction and absolutely in symmetric mode.

The region that has lower pressure distribution on front end of the chamber for all the models has different pressure distribution that effects the total pressure distribution. Since in these models, it would not be possible to divide the chambers to separate parts, estimating the average pressure inside the chamber was not possible. By sealing the rotor end tips, both these issues could be solved. In that case, fluid flow inside the chamber just remained in closed area and pressure distribution would be much more homogeneous than the current model. On the other hand, the pressure distribution in front area also would be much more than the current values.

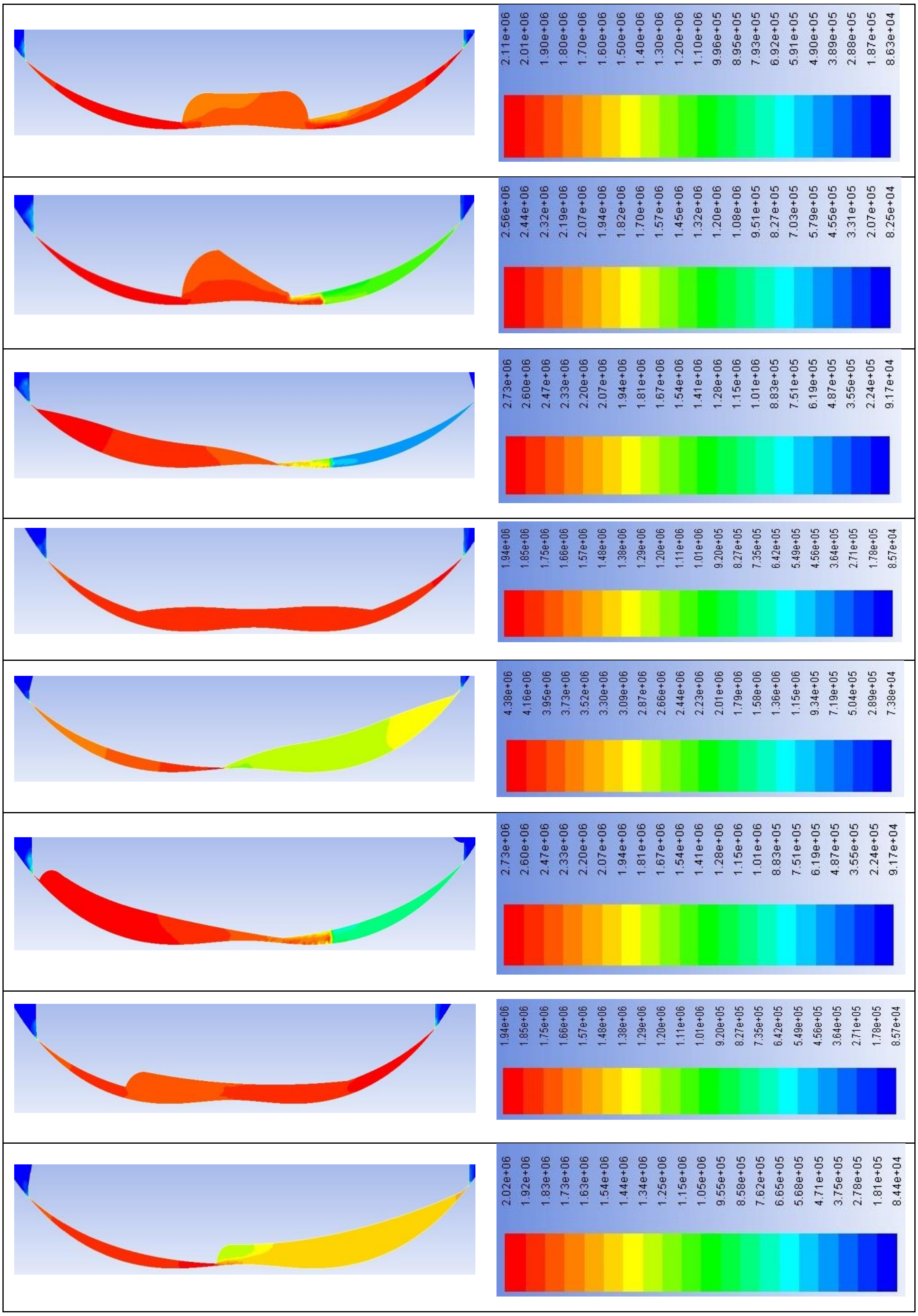

Figure 5.10 : Pressure (Pa), TDC, Various models.

5.2.3 Temperature Analysis

In this part, we will study temperature distribution for different models and different strokes while the engine is working at 9000 RPM.

5.2.3.1 Temperature analysis during the compression phase

Figure 5.11 shows the temperature distribution for different models at compression stroke. The effect of open rotor end tips could be seen here.

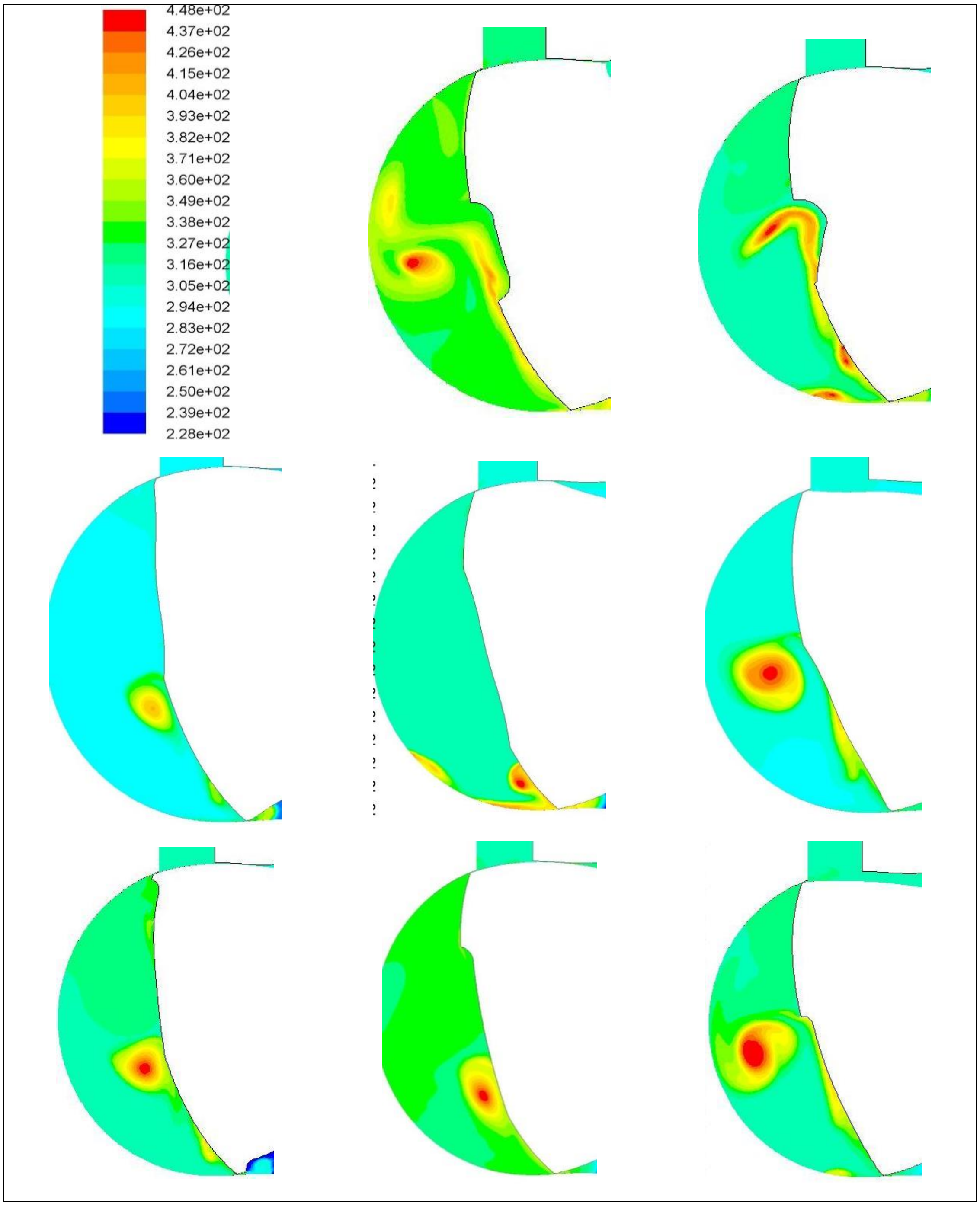

Figure 5.11 : Temperature (k) distribution for combustion chamber, compression.

5.2.3.2 Temperature analysis at TDC

The mean temperature at the end of compression and without combustion is displayed and presented in figures 5-12. It can be seen clearly that the temperature distribution also is under the effect of the geometry, but the differences are not that much. For most of the cases, the temperature differences inside the chamber at TDC is just about 40 degree of Kelvin, and this difference is due to the geometric shape of the model. For the regions with wide area, especially on the middle of the recess edge, the temperature reaches to 750 degree of kelvin. For other parts, it distributed homogeneously about 700 degree of Kelvin. The regions with higher temperature are important due to this point that for auto-ignition of the mixture, region with high temperature could be a good candidate.

As it seen from the results, the effect of the rotor tips non-sealed area results in temperature difference for the combustion chambers beside the main chamber. This difference is significant for the chamber that reaches TDC after the main chamber. For previous chamber, flow fluid from rotor tip does not influence that much, but the position of the recess also affected this.

Figure 5.13 shows the temperature distribution for the deep models. Temperature distribution for the models with deep recesses, in general has higher value than the normal recess models. Furthermore, in some regions, temperature reaches to about 900 degree of Kelvin, while the maximum value for normal recesses was just about 750 degree. This could be happen due to the wider area between rotor and housing without recess, since for these models, the rotor edge without recess is more than the previous models.

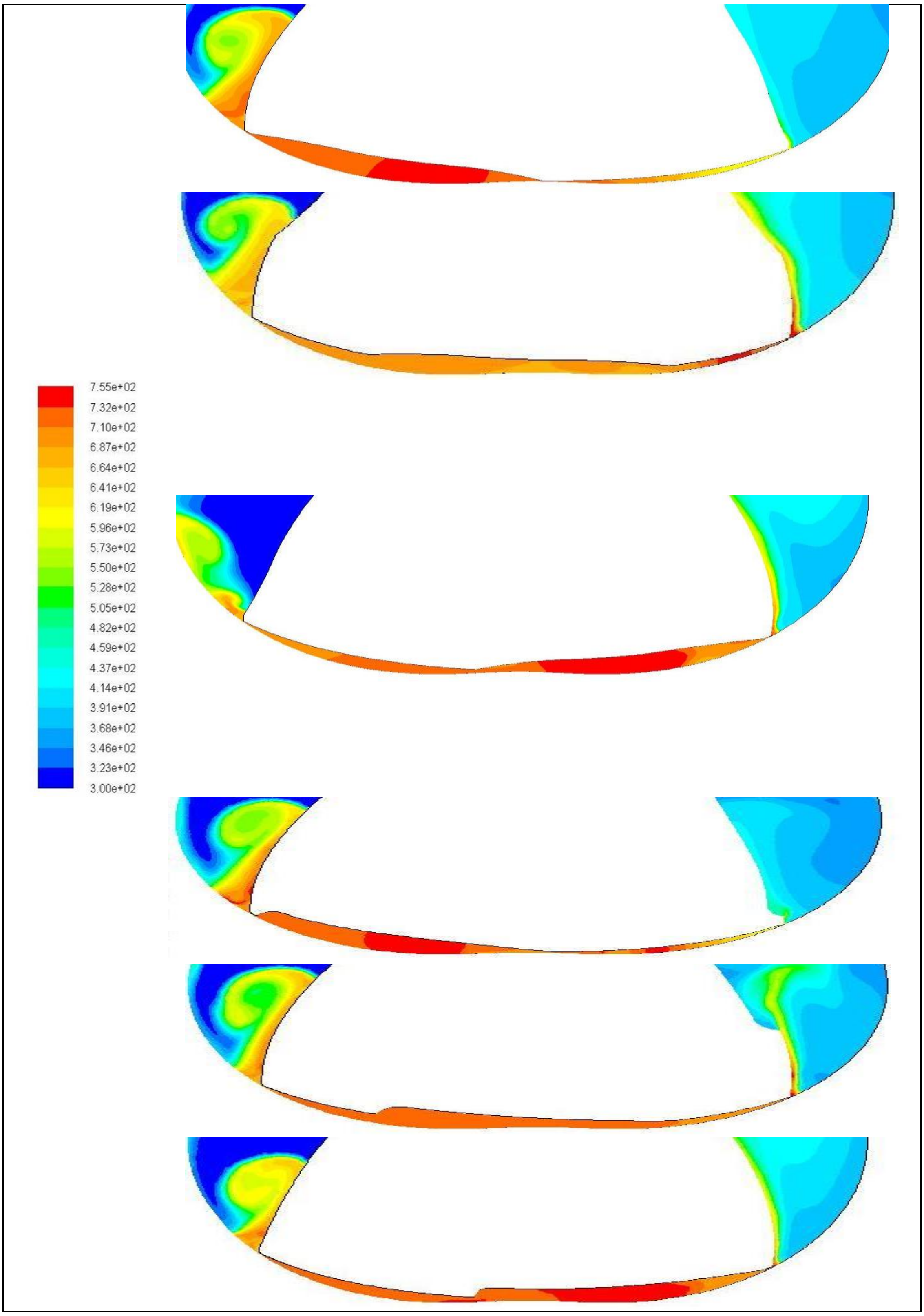

Figure 5.12 : Temperature (k) distribution, TDC, 9000 RPM models.

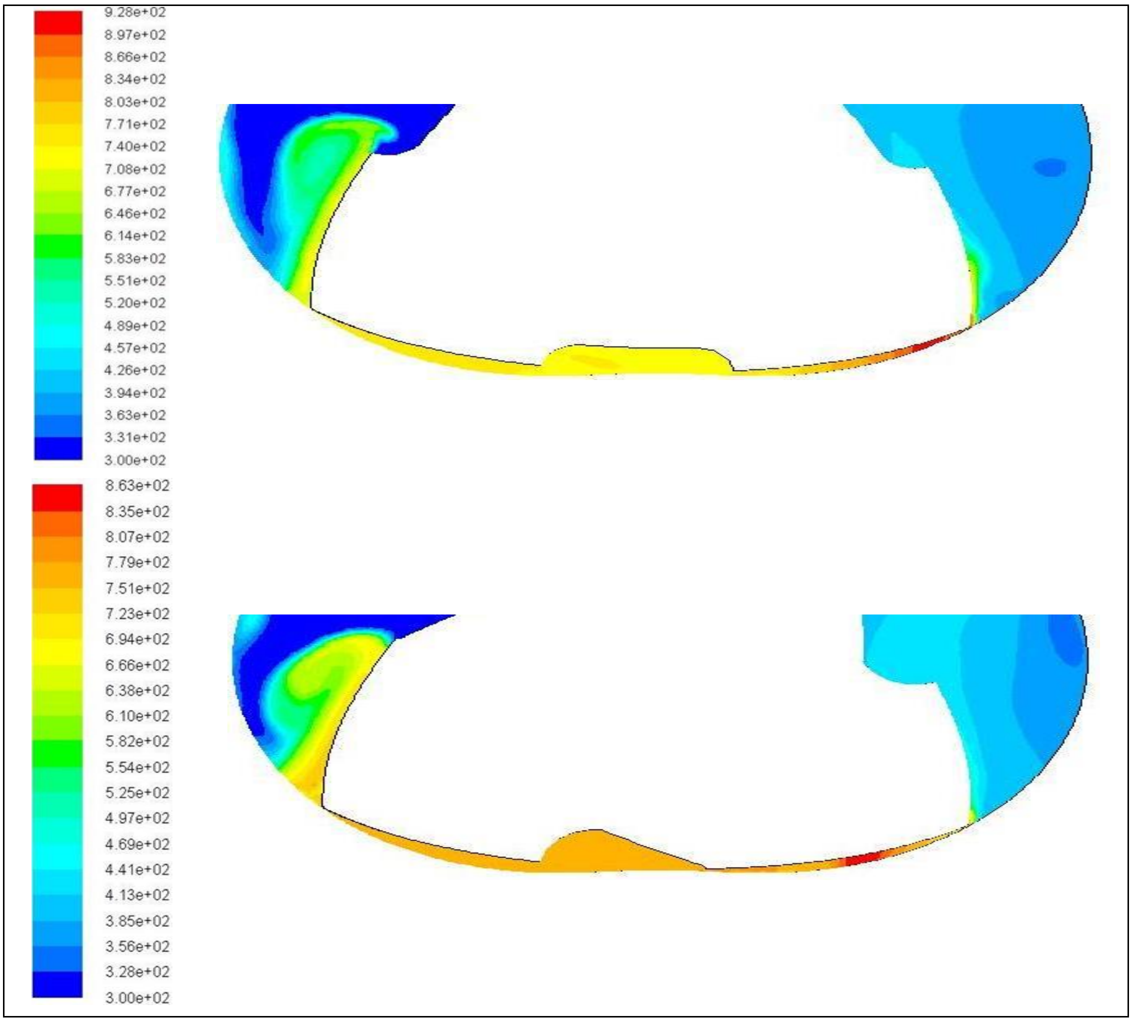

Figure 5.13 : Temperature (k) distribution, TDC, 9000 RPM deep recess models.

5.2.4 Turbulence Analysis

In this part, we would study the turbulence energy distribution for the models with various recess designs.

5.2.4.1 Swirling and increased turbulence near the intake closing

Because of the pocket geometry and the means of the straight intake pipe location, developing swirls can be seen in the figure 5-14. Turbulence also maximizes when it is close to the end of intake progression.

Air recirculation region at intake closing is clear in Figure 5-14. Some major difficulties prevent taking the advantage of the turbulence during the heavy fuel direct injection. Mainly the short ignition delay time of diesel fuel can show as a reason. It is early for diesel fuel to inject during this location of the rotor and possibly fuel will auto ignite because of the limited auto ignition time of the diesel fuel.

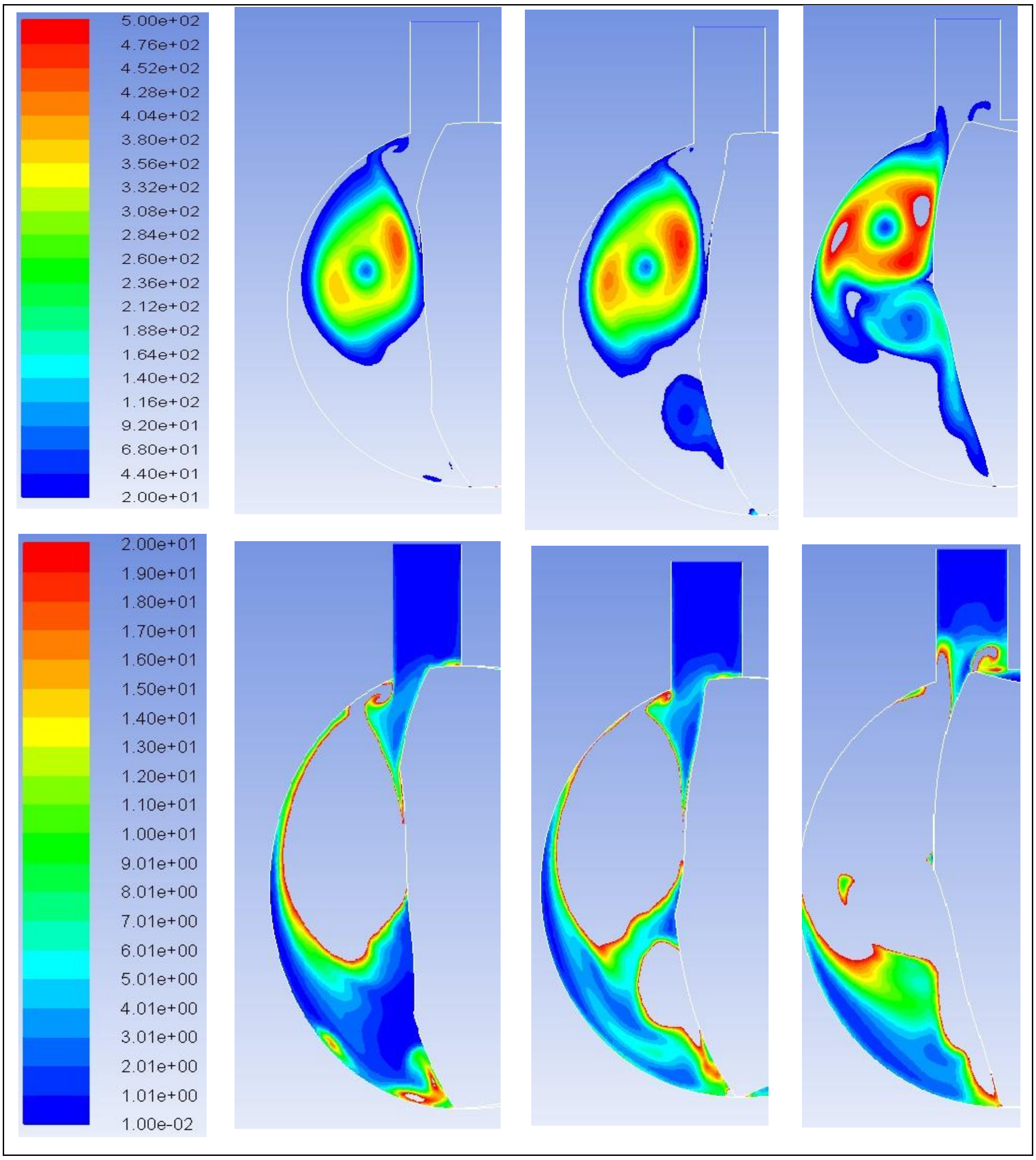

Figure 5.14 : Turbulence kinetic energy (m^2/s^2), compression phase.

As it is seen from figure above, the turbulence kinetic energy increases when the rotor tip closes to intake port end edge, and this results in higher velocity circulation inside the chamber. The difference between turbulence kinetic energy values lead to two different zones inside the chamber. As it seen from the figure, the swirling are has maximum kinetic energy 500 m^2/s^2, while for the other zones the maximum energy reaches 20 m^2/s^2. For the case with recess on its ending edge, due to the narrow area between rotor and housing, the energy is more than the case with opposite position and the turbulence kinetic energy is expanded to more area than the other models. For the model with recess on its end edge, we can see some empty zone in high scaled part, which reaches to 1080 m^2/s^2.

5.2.4.2 Turbulence close to the TDC

Figure 5-15 shows some crank step before the TDC in order to explain flow characteristics near the compression stroke. At the TDC, the combustion chamber can be divided into two parts, the end edge of the rotor and the beginning edge. At the end of the compression stroke, the beginning side starts compressing while end edge side starts expanding. Eventually this will generate a strong squish flow from the beginning edge side to the end edge side. This trend can be verified in Figure below. Meanwhile turbulence dies out and flow vectors slowly direct towards the direction of the rotor motion. Less turbulence is a disadvantage for the fuel charge improvement during the short period of direct injection. However, this strong squish flow can raise the burning speed during the combustion.

As it seen from the figure 5.15, for the case with recess on rotor right edge, there is high energetic part due to narrow area between the rotor and housing when the rotor getting near to TDC. Here, the energy is out of the scale for about 250 m2/s2 at right side and less than 1 on starting point of the empty zone. This results in higher velocity vectors in the same direction of the rotor rotation and could help to fluid flow to guide to the end edges of the rotor due to pressure difference.

5.2.4.3 Turbulence intensity close to the TDC

As it discussed in previous part, the turbulent kinetic energy and turbulent intensity are under the direct effect of velocity changes inside the chambers. For our models due to the some narrow area between the rotor and housing, velocity magnitudes became very high. The fluctuation for velocity changes could be shown by turbulence intensity in percentage. Although the scales are differs from each other, we can see the highest turbulence intensity is for the model with recess on its right side that reaches to 7000%. This value is not normal value as also we see the pressure distribution on this area. The only reason for this is the narrow area for fluid flow to passes through. Figure 5.16 shows the turbulence intensity percentage just before TDC.

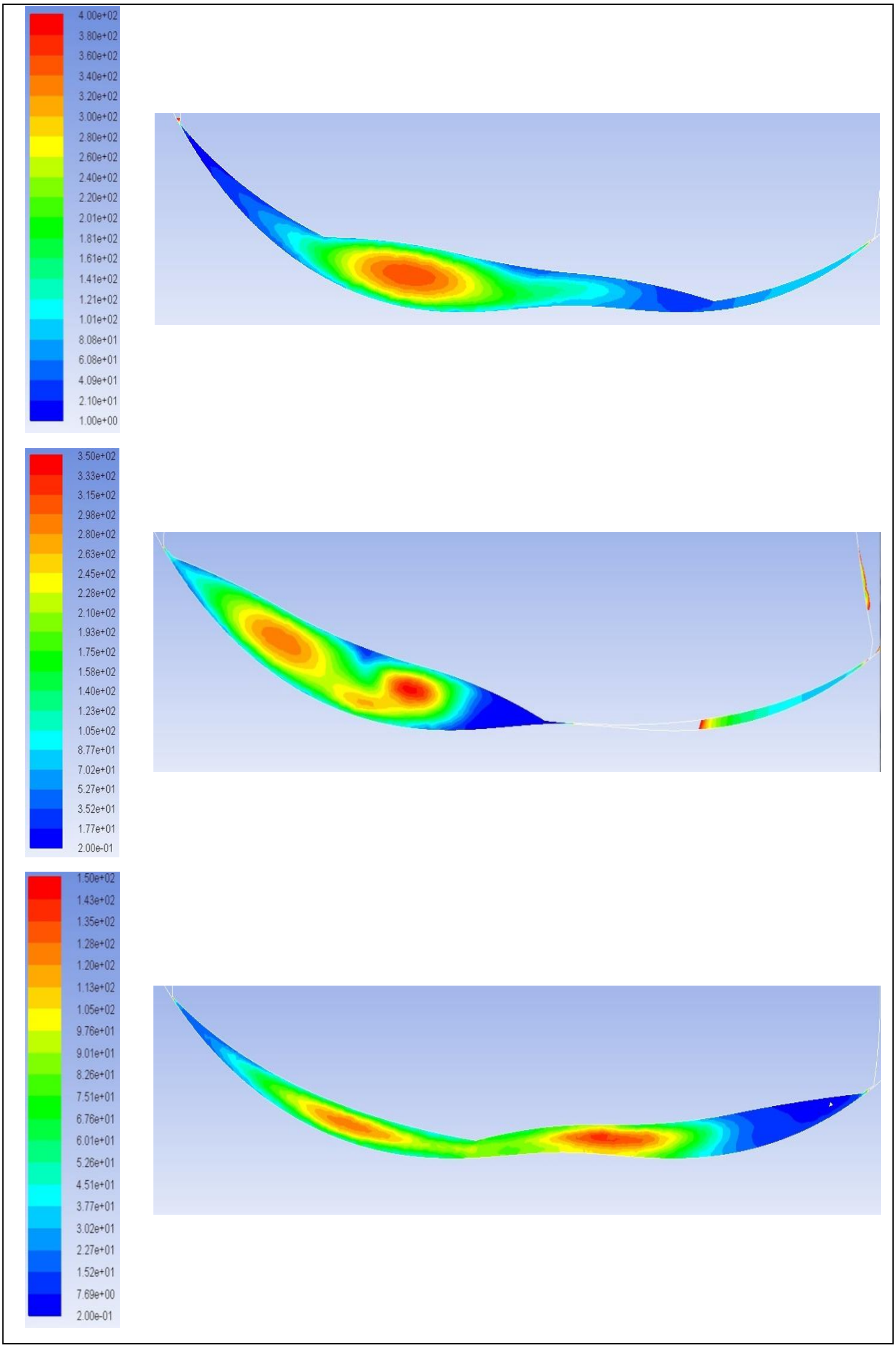

Figure 5.15 : Turbulence kinetic energy (m^2/s^2), TDC, 9000 RPM models.

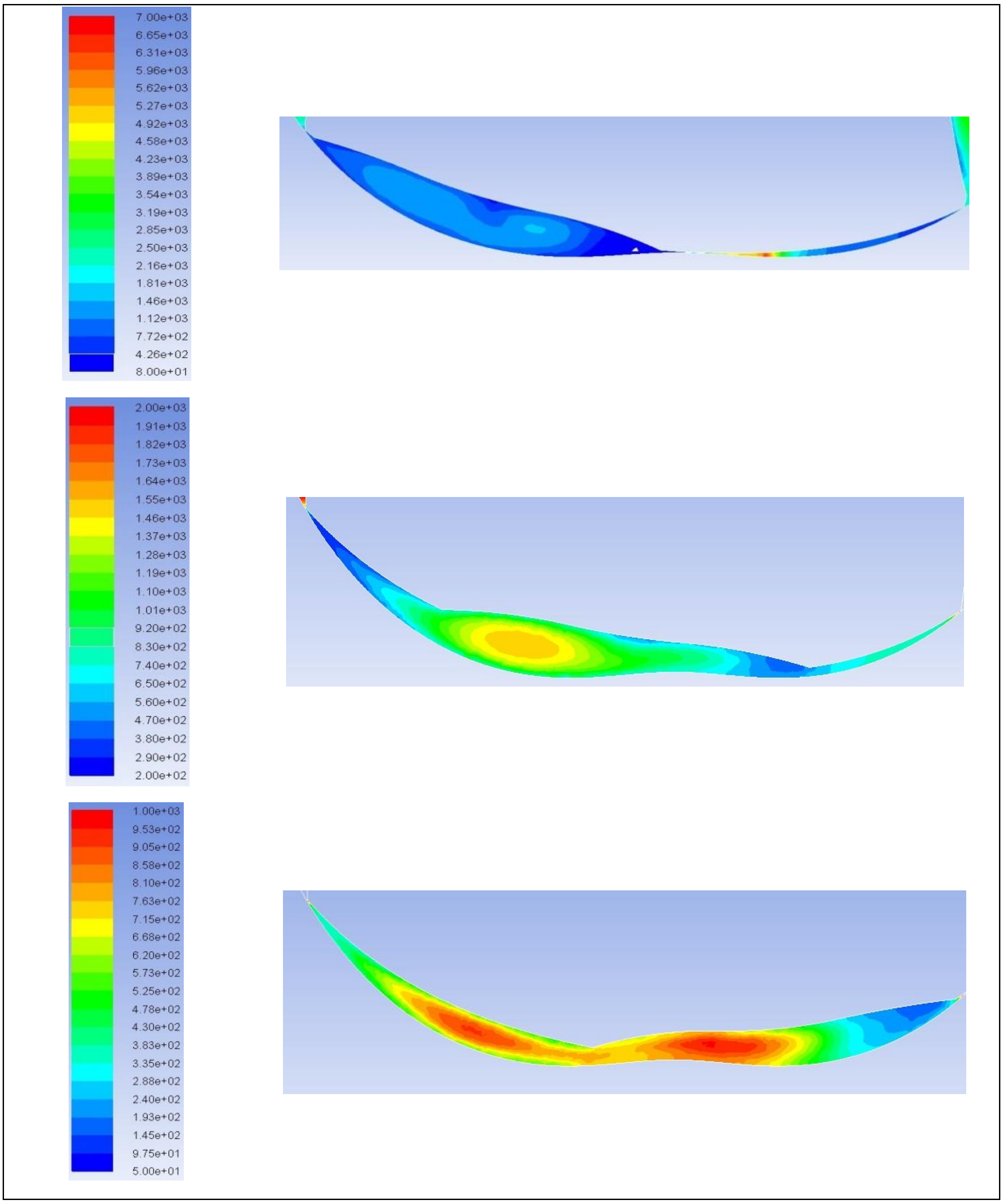

Figure 5.16 : Turbulence intensity (%) before TDC.

5.3 Comparison for the Models with Different Rotational Speed

In this part, we would like to compare the results obtained for the models with recess positioned in middle, left and right ends, while this model works under the two different rotational speeds, 1000 RPM and 3000 RPM. Then we can conclude about the effect of engine speed on fluid flow analysis especially on TDC. All the figures in this chapter, first shows the case with 1000 RPM and then the model with 3000 RPM respectively.

5.3.1 Pressure Analysis

As it is seen from figure 5-17 below, when the engine works with 3000-RPM (upper figure), and the recess positioned at right side of the rotor, pressure difference between the two region inside the chamber is about seven bars, while for the same condition when the engine is working at 9000 RPM, this value reaches at about eighteen bars. The main reason for this is the maximum pressure in first region that reaches to twenty-two bars for 9000-RPM model. This value is mainly achieved due to the narrow area at housing mid-point that creates the high pressure and velocity. Another reason that could answer this difference is the less fluid flow that ran out of the chamber due to the less time it has, in 9000-RPM model.

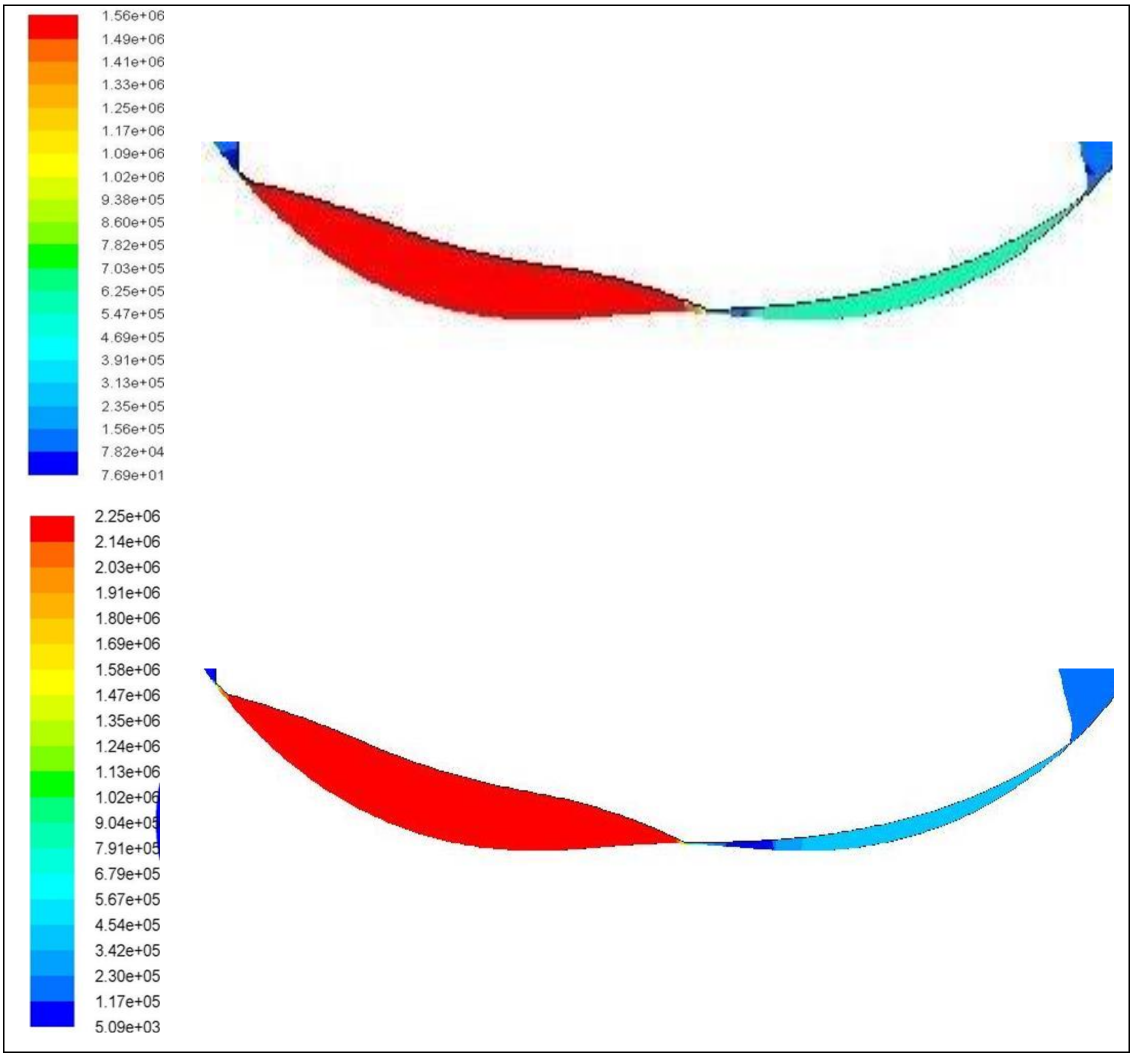

Figure 5.17 : Pressure distribution (Pa), TDC, right recess.

For the models that have recess on their middle of the rotor edge as seen at figure 5.18, the pressure distribution is almost homogeneous. The only difference between these two models is the leading region of the combustion chamber with less pressure for 9000-RPM model, which is due to the vacuum effect of the previous chamber.

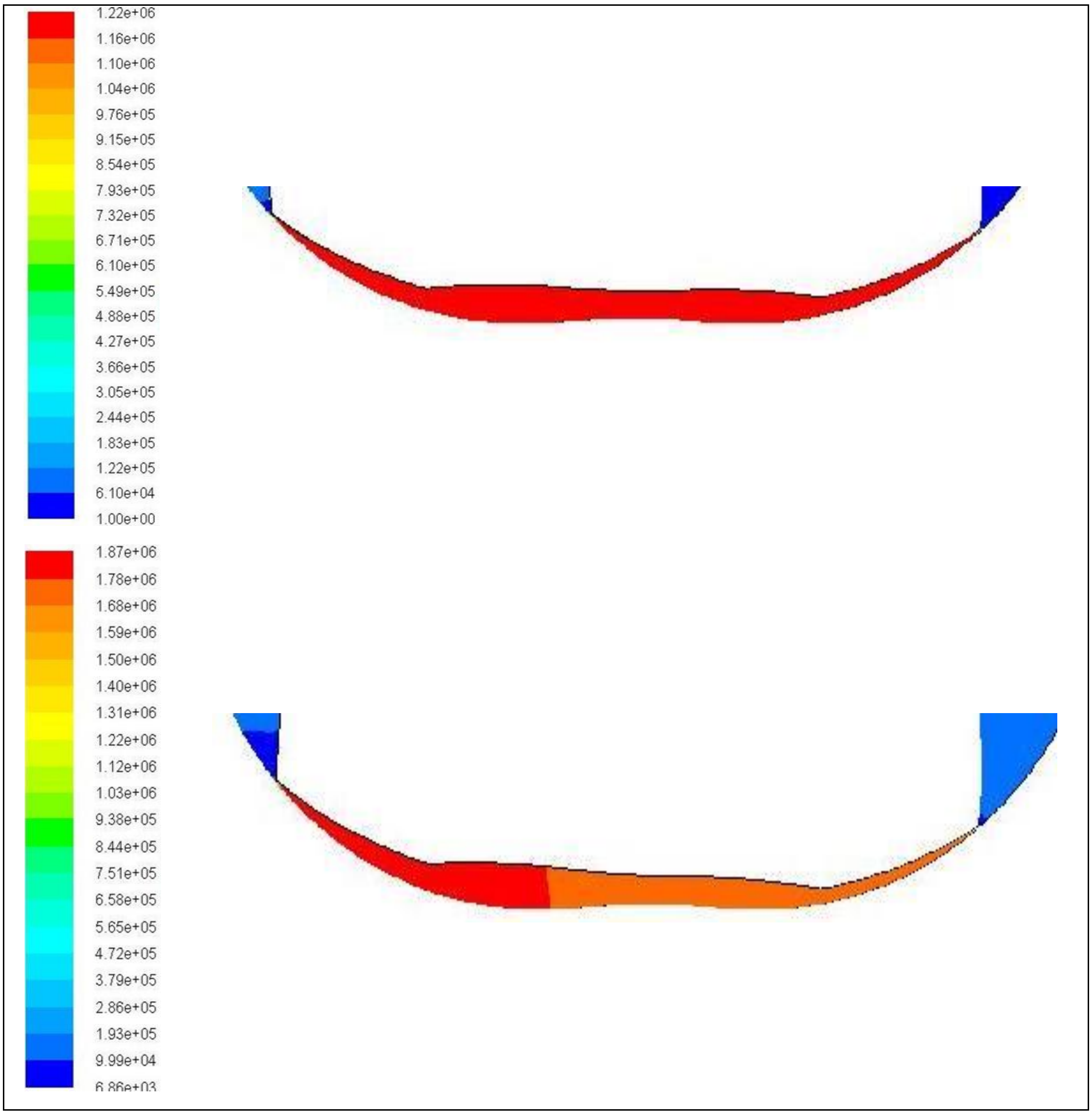

Figure 5.18 : Pressure distribution (Pa), TDC, middle recess.

Comparison between the models that have recess on their leading edge, as shown in figure 5.19, could give us the meaningful effect of the engine speed on pressure distribution. Lower engine speed leads to two different pressure zones inside the chamber. Although this difference is not that much, but the effect of lower rotational speed on velocity and pressure difference seen here.

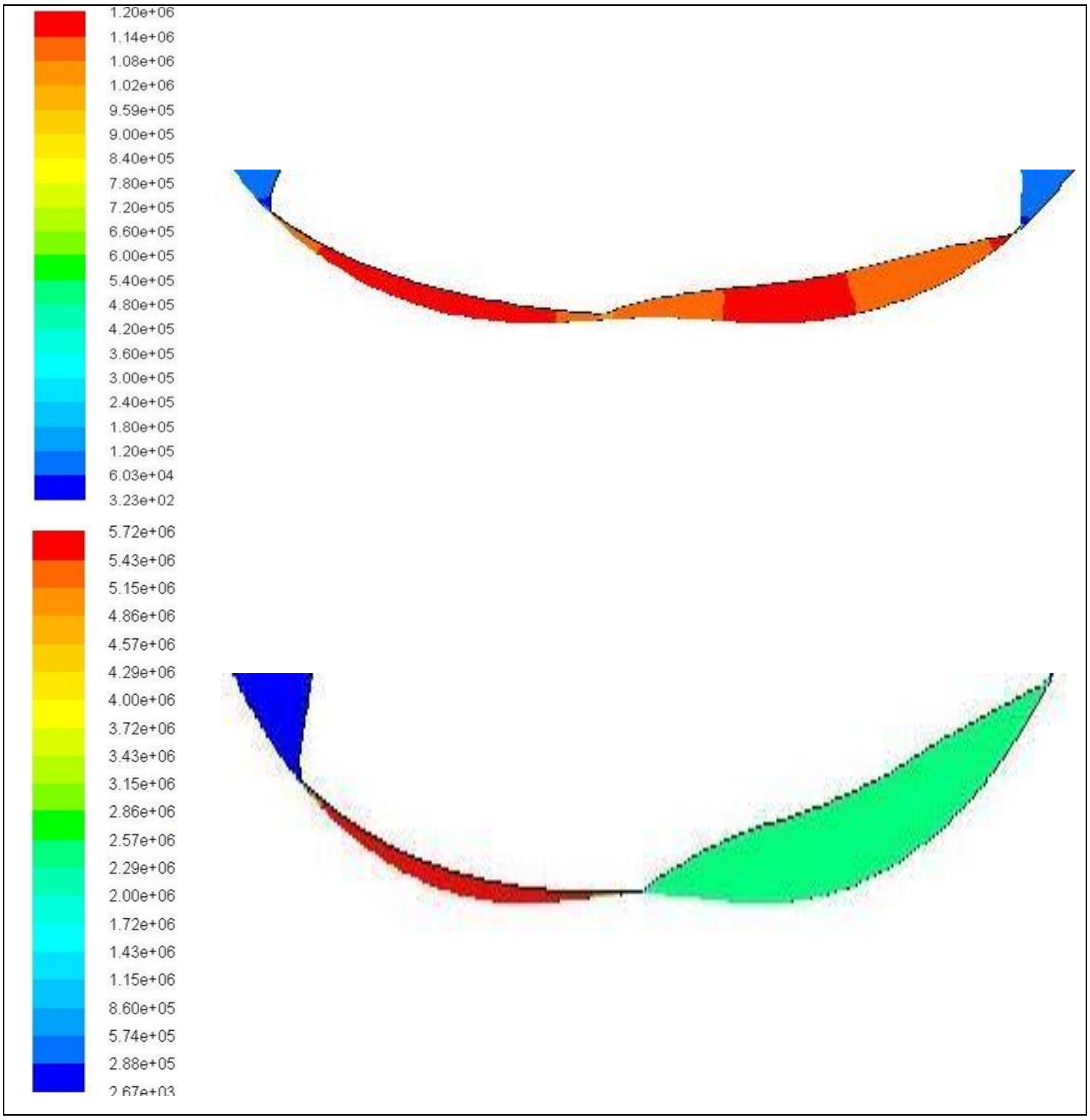

Figure 5.19 : Pressure distribution (Pa), TDC, 3000 and 9000 RPM, left recess.

5.3.2 Temperature Analysis

Different rotational speed does not affect the temperature distribution that much. Just in some cases, because of the narrow area between the rotor and the housing, and the lower flow velocity inside the chamber, the models with lower rotational speed reach to higher temperature magnitude. The effect of the flow running out of the chamber especially in front edge of the rotor concluded also from these results. Figure 5.20 shows the models that the recess positioned in right side of the rotor.

It could be concluded from the figures 5.21 and 5.22 that as like as the other cases with recess on their middle part, for temperature distribution also the rotational speed does not affect the model that much, just for the rotor end tips, we can see some differences on temperature due to high fluid flow.

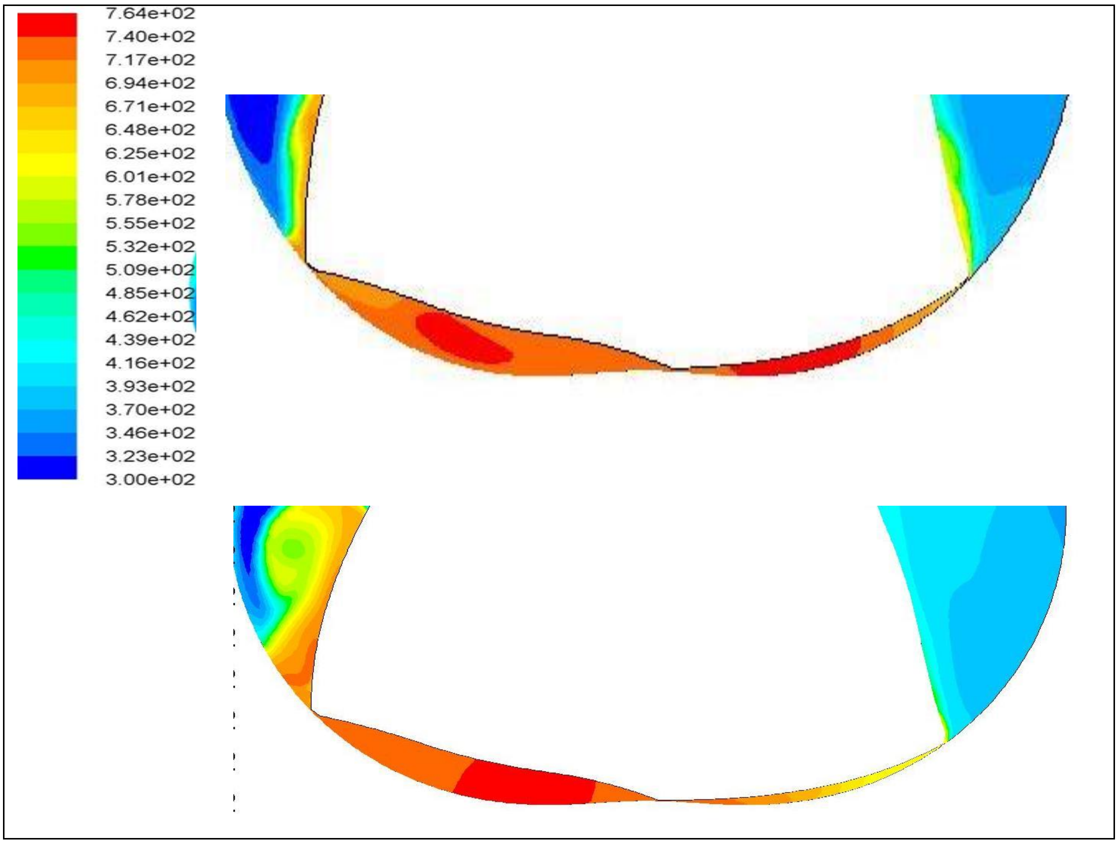

Figure 5.20 : Temperature distribution (k) , TDC, right recess.

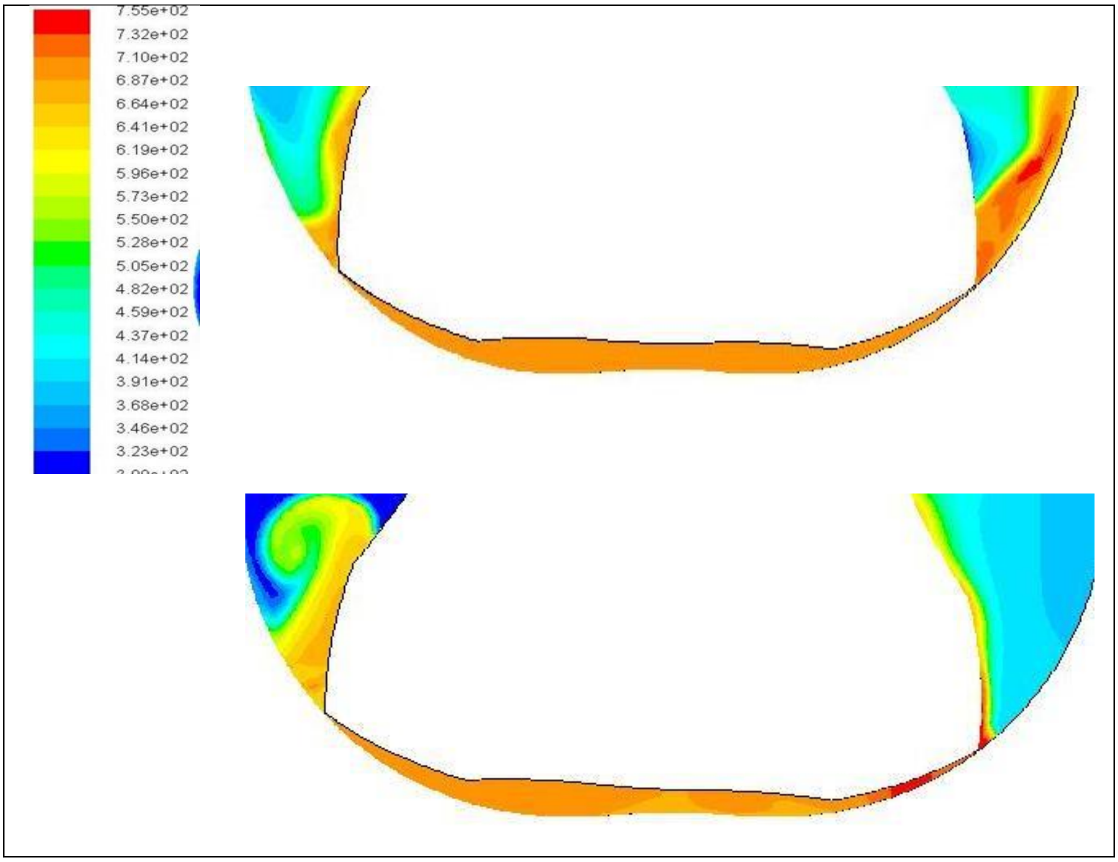

Figure 5.21 : Temperature distribution (k), TDC, middle.

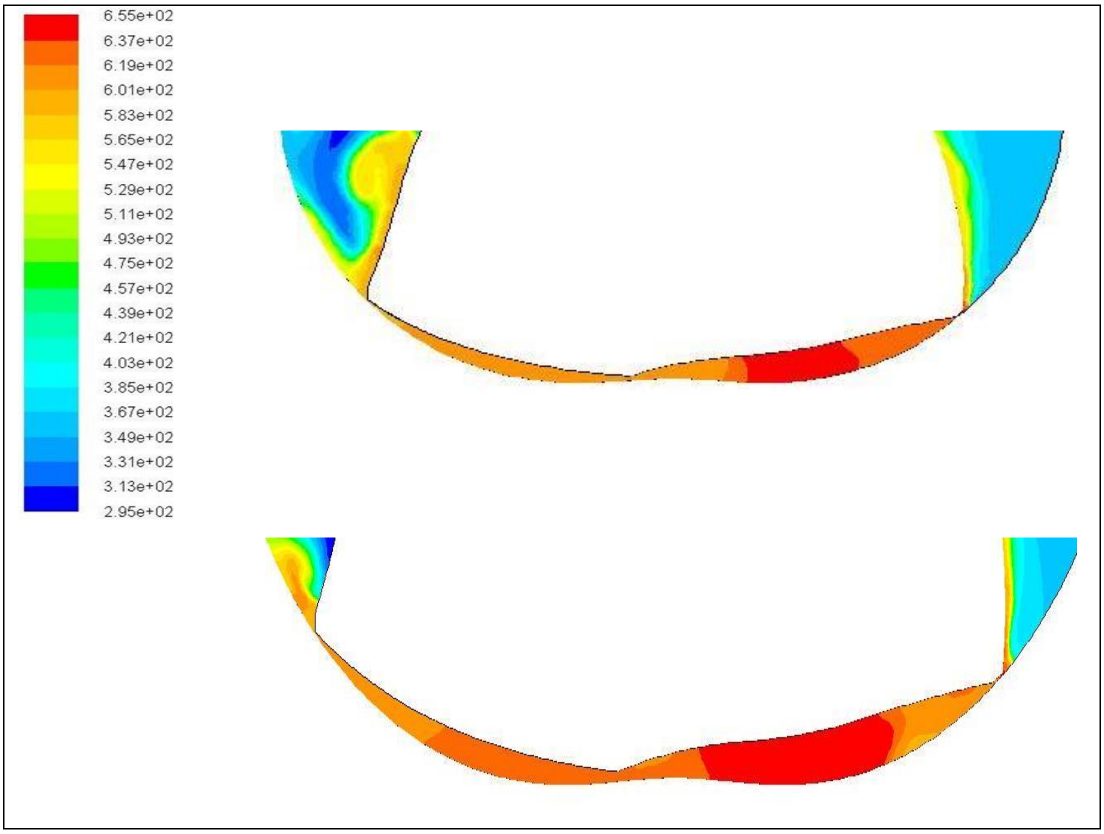

Figure 5.22 : Temperature distribution (k), TDC, left recess.

5.3.3 Velocity Analysis

Rotational speed does not affect the velocity magnitude inside the combustion chamber when the rotor is in its TDC position. The most important result in this part is referred back to high velocity fluid flows on rotor tips, that is possibly due to pressure differences between different combustion chambers. This velocity differences are critical at end tip of the rotor, since the flow is transferred in the same direction of the rotor rotation, when the rotor is at its TDC position and the fluid has less area to any circulation inside the chamber.

Figure 5.23 shows the velocity distribution at TDC for both the 3000 and 9000 ROM models. In addition, as it seen from the figure 5.24, for the following model, there is high velocity region in neighbor combustion chamber, due to the pressure difference, and since the rotation, speed is lower, the fluid has much more time to transfer between these chambers, in comparison with the model that rotates at 9000 RPM. Figure 5.25 shows the velocity distribution for the left sided recess.

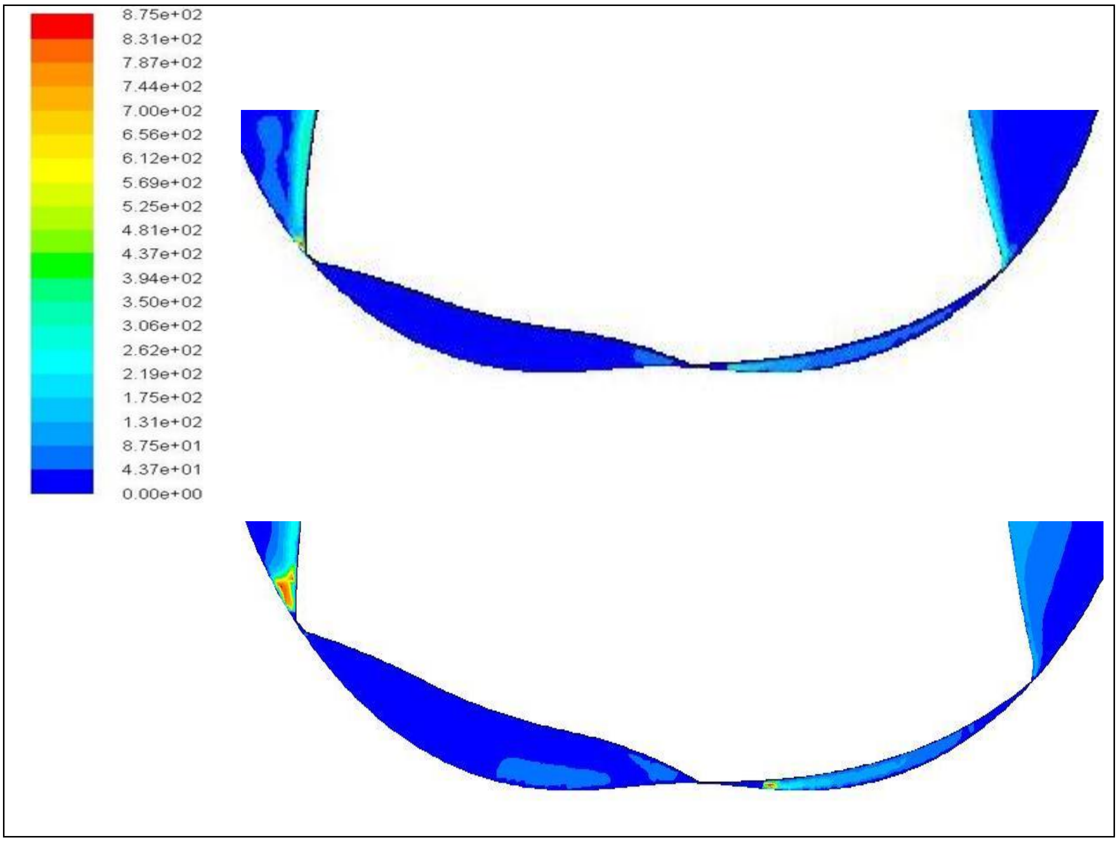

Figure 5.23 : Velocity distribution (m/s), TDC, right recess.

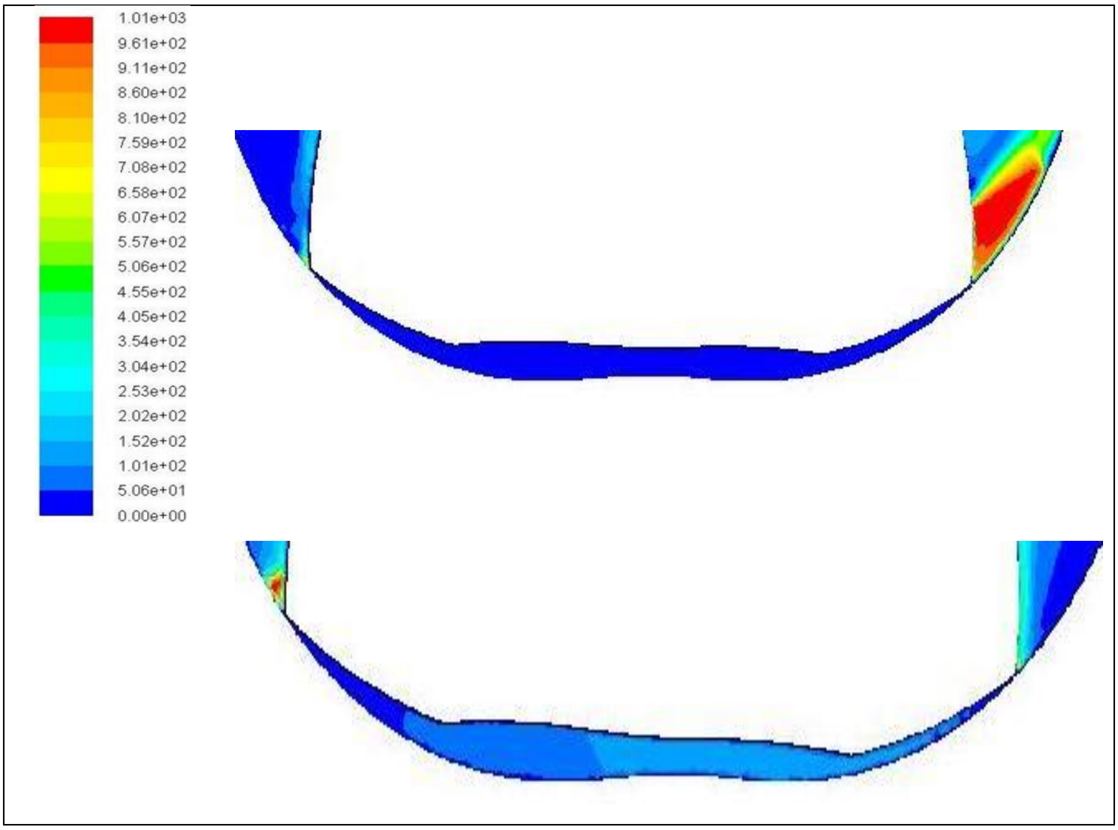

Figure 5.24 : Velocity distribution (m/s), TDC, middle recess.

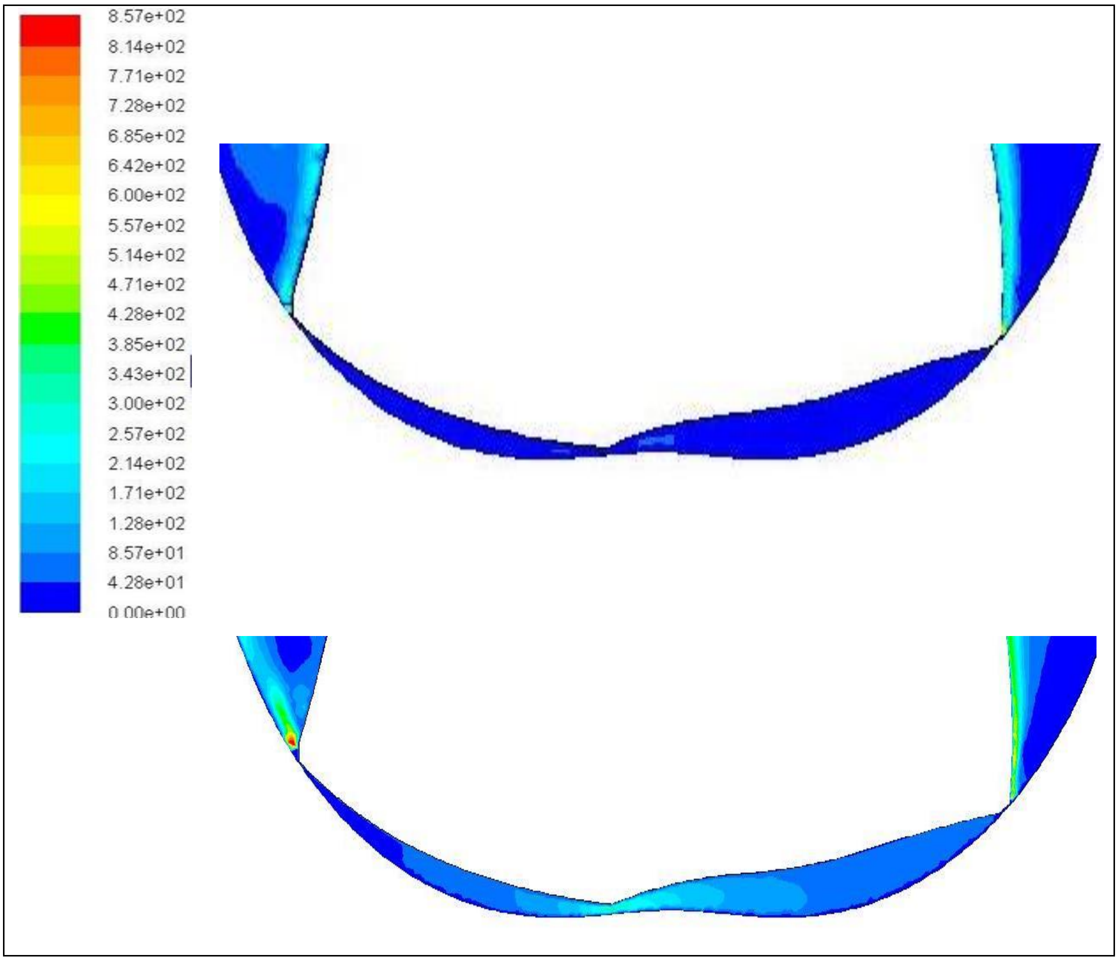

Figure 5.25 : Velocity distribution (m/s), TDC, left recess.

6. CONCLUSION AND RECOMMENDATION

In this research work, the main objectives were concentrated on Wankel engine and the fluid flow inside the engine studied. The program that made this possible in this work was ANSYS FLUENT v.15. An experience has been gained in designing and optimizing the model. To achieve such goal, it was necessary to study the engine itself, including the flow inside engine combustion chamber.

The Wankel engine fluid flow study can be summarized and concluded as follow:

- The results show that two flow vortexes formed on combustion chamber during the early stage of the intake stroke continued until the tailing rotor apex become closer to inlet port and when the port is closed.
- The rotor geometry and recess shape have affected the inlet flow, for some of the models, due to the recess position, inlet flow directed to end tip of the rotor without any recirculation.
- Positon of the recess and its symmetric or non-symmetric form, can affect the velocity and pressure distribution at TDC. Although the advantageous of this point could help the engineers to improve the combustion model, on the other hand it could result in very high values for pressure.
- The engine working speed directly affects the results on this simulation due to the non-sealed rotor tips. For pressure study, higher rotational speed of the rotor decreases the unwanted fluid flow effect on rotor tips.
- Comparison on pressure results helps the designers to place the spark plug on its optimum position, because the pressure difference between the chambers would affect the ignition process.
- Because of the 2D simulation model used in this study, the results especially for the pressure are higher than the realistic values.
- Comparing the obtained results with previous studies highlighted the non-sealed rotor tips effect on this study.
- Comparing the results obtained from non-CFD method, with the experimental works, highlighted the effect of sealing, due to the different velocity vector directions
- As it seen from the results, for the model that had not sealed, the velocity vector on rotor tips are running out of the chamber, while for the sealed

models reported in experimental works, the velocity vectors are on the direction of chamber inside.

- Turbulence intensity could be the most important factor for comparing different geometry models, that how they affect the magnitude of fluid flow that path out from the chamber.
- Since this study did not include the combustion part, it would be hard to estimate and choose the optimum model. The significant point is the differences between symmetric and non-symmetric models, that always the symmetric models have better physical distribution.
- Wider recess design may help to get the homogeneous distribution inside the chamber, but due to the smaller side length, the fluid flow has less area to circulate inside the recess chamber.
- Placing the recess position in middle of the rotor edge, could be the best choice among the other models due to the less effect on velocity magnitude when the rotor passes on the TDC.
- Because of the 2D study, the recess height does not have meaning here, and affect the results. For 3D study' or real condition, the recess height is smaller than the rotor height.

In this study, as it explained before, the aim was to simulate a 3D model of the Wankel engine. At the time of writing this thesis, because of the computer calculation RAM and some modeling problems, this aim did not achieved. Experiencing the problems and getting new ideas, now make it possible to model the engine first of all without any leakage at rotor tips, by defining the rough fluid area, and then changing the model to 3D. Placing the intake and exhaust ports on side part is another challenging issue on this way.

Working on this topic simultaneously with experimental study that is going to be ready in next few months, would help the researches to optimize the geometric model and would help the aim of changing the normal four stroke engine to two stroke one rotor engine. Ongoing projects in Automotive laboratory is experimental and theatrical research on Wankel engine and this thesis could be the starting point of these works in future.

REFERENCES

[1] **Abdul, S., Ismail, R., & Bakar, R. A**. (2009). Gas Fuel Spray Simulation of Port Injection Compressed Natural Gas Engine Using Injector Nozzle Multi Holes.*European Journal of Scientific Research*, *ISSN*, 188-193.

[2] **Heller, D.A.** (2004). International Strategic Alliance of Technology Strategy: The case of Rotary Engine Development at Mazda. Shinshu University.

[3] **URL-1:** http://experts.about.com/e/w/wa/Wankel_engine.htm**.**

[4] **Yamamoto, K.** (1981). *Rotary engine*. Sankaido.

[5] **Jones, C.** (1984). Advanced Development of Rotary Stratified Charge 750 and 1500 HP Military Multi-Fuel Engines at Curtiss-Wright (No. 840460). SAE Technical Paper.

[6] **Jones, C., & Mount, R. E.** (1984, June). Design of a high-performance rotary stratified-charge research aircraft engine. In *AIAA/SAE/ASME 20th joint propulsion conf., June 11-13, 1984. Cincinnati (Oh)* (Vol. 84, p. 1395).

[7] **Warner, M.** (2009). *Street Rotary*, Penguin, New York.

[8] **Wakisaka, T., Imamura, F., Nguyen, T. T., Takeuchi, S. I., & Chung, J. H.** (2000, June). Numerical simulation of hollow-cone sprays in gasoline direct-injection engines. In *Seoul 2000 FISITA World Automotive Congress*.

[9] **Hentschel, W.** (2000). Optical diagnostics for combustion process development of direct-injection gasoline engines. *Proceedings of the combustion institute*,*28*(1), 1119-1135.

[10] **Wang, J., Huang, Z., Zheng, J., & Miao, H.** (2009). Effect of partially premixed and hydrogen addition on natural gas direct-injection lean combustion.*international journal of hydrogen energy*, *34*(22), 9239-9247.

[11] **Nguyen, H. L.** (1987). Performance and combustion characteristics of direct-injection stratified-charge rotary engines.

[12] **Yamamoto, K.** (1971), *Rotary Engine*, Sankaido, Tokyo.

[13] **Abdul, S., Ismail, R., & Bakar, R. A.** (2009). Gas Fuel Spray Simulation of Port Injection Compressed Natural Gas Engine Using Injector Nozzle Multi Holes.*European Journal of Scientific Research*, *ISSN*, 188-193.

[14] **Sato, S., Yamashita, D., & Iida, N.** (2007). Influence of the Fuel Compositions on the Homogeneous Charge Compression Ignition Combustion (First Report)-Effect of the Variations of Fuel Compositions on the

Oxidation Reaction Processes of Pre-mixture. TRANSACTIONS-SOCIETY OF AUTOMOTIVE ENGINEERS OF JAPAN, 38(2), 113.

[15] **Wallesten, J., Lipatnikov, A., & Chomiak, J.** (2002). Modeling of stratified combustion in a direct-ignition, spark-ignition engine accounting for complex chemistry. *Proceedings of the Combustion Institute*, *29*(1), 703-709.

[16] **Bradley, D., & Head, R. A.** (2006). Engine autoignition: The relationship between octane numbers and autoignition delay times. *Combustion and flame*,*147*(3), 171-184.

[17] **Yamamoto, K.** (1981), *Rotary Engine,* Sankaido, Tokyo.

[18] **Sierens, R., Baert, R., Winterbone, D. E., & Baruah, P. C**. (1983). *A comprehensive study of Wankel engine performance* (No. 830332). SAE Technical Paper.

[19] **Hicks, Y. R., Schock, H. J., Craig, J. E., Umstatter, H. L., & Lee, D. Y.** (1986). Visualization of flows in a motored rotary combustion engine using holographic interferometry.

[20] **Semenov, E.S.,** (1958) "Studies of Turbulent Gas Flow in Piston Engines," Otdelenie Tekh- nicheskikh Nauk, No. 8, 1958 (NASA Technical Translation F97).

[21] **Bracco, F. V., & Sirignano, W. A.** (1973). Theoretical analysis of Wankel engine combustion. *Combustion Science and Technology*, *7*(3), 109-123.

[22] **Danieli, G. A., Ferguson, C. R., Heywood, J. B., & Keck, J. C.** (1974).*Predicting the emissions and performance characteristics of a Wankel engine*(No. 740186). SAE Technical Paper.

[23] **Shih, T. P., Yang, S. L., & Schock, H. J.** (1986). *A two-dimensional numerical study of the flow inside the combustion chamber of a motored rotary engine*(No. 860615). SAE Technical Paper.

[24] **Boni, A.A. and Nakayaraa, P.I. (**1975**),** "Two-Dimensional Computer Simulation of Combustion in a Divided-Chamber Stratified Charge Engine," Fifth International Colloquium on Gas Dynamics of Explosions and Reactive Systems.

[25] **Grasso, F., Wey, M. J., Bracco, F. V., & Abraham, J**. (1987). *Three-dimensional computations of flows in a stratified-charge rotary engine* (No. 870409). SAE Technical Paper.

[26] **Amsden, A. A., Ramshaw, J. D., O'Rourke, P. J., & Dukowicz, J. K**. (1985).*KIVA: A computer program for two-and three-dimensional fluid flows with chemical reactions and fuel sprays* (No. LA-10245-MS). Los Alamos National Lab., NM (USA).

[27] **Steinthorsson, E., Shih, T. I., Schock, H. J., & Stegeman, J.** (1988).*Calculations of the unsteady, three-dimensional flow field inside a motored wankel engine* (No. 880625). SAE Technical Paper.

[28] **Abraham, J., & Bracco, F. V.** (1988). *Comparisons of computed and measured mean velocity and turbulence intensity in a motored rotary engine* (No. 881602). SAE Technical Paper.

[29] **Hamady, F., Stuecken, T., & Schock, H.** (1990). *Airflow Visualization and LDV Measurements in a Motored Rotary Engine Assembly Part 1: Flow Visualization* (No. 900030). SAE Technical Paper.

[30**] Li, Z., Steinthorsson, E., Shih, T. I., & Nguyen, H. L.** (1990). *Modelling and simulation of wankel engine flow fields* (No. 900029). SAE Technical Paper.

[31] **Chen, H. C., & Patel, V. C.** (1988). Near-wall turbulence models for complex flows including separation. *AIAA journal, 26*(6), 641-648.

[32] **Abraham, J., Bracco, F. V., & Epstein, P.** (1993). *3-D Computations to Improve Combustion in a Stratified-Charge Rotary Engine Part IV: Modified Geometries*(No. 930679). SAE Technical Paper.

[33] **Jeng, D. Z., Hsieh, M. J., Lee, C. C., & Han, Y.** (2013). *The Numerical Investigation on the Performance of Rotary Engine with Leakage, Different Fuels and Recess sizes* (No. 2013-32-9160). SAE Technical Paper.

[34] **Danieli, G. A., Keck, J. C., & Heywood, J. B.** (1978). *Experimental and theoretical analysis of Wankel engine performance* (No. 780416). SAE Technical Paper.

[35] **Abraham, J., Wey, M. J., & Bracco, F. V.** (1988). Pressure Non-Uniformity and Mixing Characteristics in a Stratified Charge Rotary Engine. *SAE Paper,880604*.

[36**] Abraham, J., & Bracco, F. V.** (1989). *Comparisons of computed and measured pressure in a premixed-charge natural-gas-fueled rotary engine* (No. 890671). SAE Technical Paper.

[37] **Amsden, A. A., Ramshaw, J. D., O'Rourke, P. J., & Dukowicz, J. K.**(1985). *KIVA: A computer program for two-and three-dimensional fluid flows with chemical reactions and fuel sprays* (No. LA-10245-MS). Los Alamos National Lab., NM (USA).

[38] **Abraham, J., & Bracco, F. V.** (1992). *3-D Computations to Improve Combustion in a Stratified-Charge Rotary Engine-Part III: Improved Ignition Strategies* (No. 920304). SAE Technical Paper.

[39] **Shih, T.I., Yang, S.L., and Schock, H.J.** (1986). A Two-Dimension Numerical Study of the Flow Inside the Combustion Chamber of a Motored Rotary Engine. SAE Paper 860615.

[40] **Steinthorsson, E., Shih, T. I., Schock, H. J., & Stegeman, J.** (1988).*Calculations of the unsteady, three-dimensional flow field inside a motored wankel engine* (No. 880625). SAE Technical Paper.

[41] **Hamady, F., Schock, H., and Stueckon, T.,** (1989) Air Flow Visualization and LDV Measurements in a Motored Rotary Engine Assemply-Part 1. Flow Visualization, SAE Paper 900030.

[42**] Izweik, H. T.** (2009). CFD investigations of mixture formation, flow and combustion for multi-fuel rotary engine. *Technischen Universität Cottbus*.

[43] **Brahmadevan, V. P.** (2004). *Numerical Modelling and Simulation of Rotary Engine* (Doctoral dissertation, MSc Thesis, Cranfield University).

APPENDICES

APPENDIX A: Boundary Wall Lengths for Non-CFD Grids
APPENDIX B: Velocity Calculated with Non-CFD Method

APPENDIX A

Boundary Wall Lengths for Non-CFD Grids

Table A.1 : Wall lengths for different recess positions on rotor

Length	ortalama			122.5-120	125-122.5	127.5-125	130-127.5	132.5-130	135-132.5	137.5-135	140-137.5	142.5-140	145-142.5	147-145	150-147	152-150
X1-X2				23.904895	23.78725	23.650025	23.432525	23.13123385	22.74233385	22.26162351	21.71782351	21.04408	20.23832	19.36317	18.38754	17.31591
X2-x3				43.24395	43.1387	42.953325	42.645825	42.2132974	41.6531504	40.9626159	40.16171292	39.20541	38.09284	36.86674	35.50552	34.01124
X3-x4				56.01995	55.9106	55.67855	55.3023	54.7743859	54.0943564	53.26848112	52.30719562	51.18648	49.90853	48.50118	46.95496	45.2741
X4-x5				63.81665	63.6836	63.40045	62.95745	62.35515	61.59537285	60.68059579	59.61961294	58.40585	57.0443	55.55117	53.92736	52.17966
X5-x6				64.259045	64.094945	63.76785	63.27945	62.63246838	61.83050413	60.87802485	59.7802591	58.54374	57.17548	55.68284	54.07425	52.35837
X6-x7				57.76415	57.57715	57.22845	56.728045	56.0801835	55.2897755	54.3625315	53.3011945	52.12096	50.8298	49.42878	47.93071	46.34525
X7-x8				49.86065	49.67445	49.342135	48.877875	48.28709655	47.5755269	46.7490074	45.808817	44.77414	43.6528	42.44209	41.15597	39.80413
X8-x9				37.13695	36.98835	36.7231	36.355885	35.89267372	35.33892942	34.6995876	33.9751469	33.18442	32.33391	31.41916	30.45227	29.44213
X9-x10				20.2804	30.208425	30.065475	19.86165	19.60230145	19.29138445	18.93200071	18.52430271	18.08166	17.60816	17.09968	16.56362	16.00664

Length	155-152	157-155	160-157	162-160	165-162	167-165	170-167	172-170	175-172	177-175	180-177	182-180
X1-X2	16.156	14.92202	13.63497	12.32512	11.03222	9.803305	8.688558	7.730296	6.951508	6.347302	5.889236	5.537848
X2-x3	32.38629	30.63626	28.76858	26.79423	24.72901	22.5947	20.42169	18.25071	16.13819	14.15819	12.39924	10.94745
X3-x4	43.46289	41.52745	39.47398	37.30981	35.04368	32.68588	30.24897	27.74695	25.19871	22.62956	20.0726	17.57484
X4-x5	50.31505	48.34145	46.26651	44.09807	41.84425	39.51334	37.11403	34.65423	32.14309	29.59136	27.01033	24.4143
X5-x6	50.5441	48.64047	46.65637	44.60043	42.48097	40.30592	38.08293	35.81859	33.5195	31.19238	28.8432	26.47825
X6-x7	44.682	42.94997	41.15846	39.31615	37.43115	35.51091	33.56221	31.59126	29.60353	27.60389	25.59678	23.58602
X7-x8	38.39561	36.93817	35.44054	33.91058	32.35545	30.78155	29.19442	27.59983	26.00225	24.40496	22.81167	21.22503
X8-x9	28.39591	27.31884	26.21816	25.10007	23.97003	22.83274	21.69197	20.55282	19.41854	18.29058	17.17206	16.06469
X9-x10	15.433	14.84431	14.24528	13.63971	13.03071	12.42054	11.81067	11.2054	10.6064	10.01296	9.427483	8.850818

Length	185-182	187-185	190-187	192-190	195-192	197-195	200-197	202-200	205-202	207-205	210-207
X1-X2	5.257715	5.027745	4.846419	4.732608	4.713225	4.804215	4.998324	5.273062	5.604675	5.976327	6.37739
X2-x3	9.848665	9.070212	8.514424	8.086441	7.757326	7.586985	7.674136	8.044348	8.627529	9.343138	10.14126
X3-x4	15.20286	13.04765	11.22128	9.820074	8.84659	8.179097	7.709556	7.54564	7.887675	8.696243	9.773711
X4-x5	21.82194	19.25871	16.76118	14.38303	12.20208	10.32284	8.853875	7.827043	7.173208	7.051117	7.696978
X5-x6	24.10437	21.72968	19.36429	17.02184	14.7216	12.49167	10.37358	8.427942	6.738424	5.403454	4.568484
X6-x7	21.57524	19.56815	17.56849	15.58051	13.60968	11.66359	9.752834	7.892799	6.106719	4.430423	2.921833
X7-x8	19.64743	18.08114	16.52802	14.9897	13.46813	11.96591	10.48627	9.033584	7.6147	6.2403	4.927112
X8-x9	14.97004	13.88963	12.82448	11.77532	10.74295	9.728474	8.733019	7.75792	7.095214	6.169101	4.985058
X9-x10	8.283763	7.727079	7.181243	6.646526	6.123245	5.61184	5.112651	4.626059	4.152783	3.693987	3.251345

APPENDIX B

Velocity Calculated with Non-CFD Method

Table B.1 : Transfer velocities for middle recess modeled rotor

Harekat			122.5-120	125-122.5	127.5-125	130-127.5	132.5-130	135-132.5	137.5-135	140-137.5	142.5-140	145-142.5	147-145	150-147	152-150	155-152	157-155	160-157	162-160
Area	(mm2)	New																	
X1-X2			1628.392	1618.98	1608.002	1590.602	1566.499	1535.387	1496.93	1453.426	1399.527	1335.066	1265.054	1187.003	1101.273	1008.48	909.7615	806.7973	702.0093
X2-x3			2978.716	2970.296	2955.466	2930.866	2896.264	2851.452	2796.209	2732.137	2655.633	2566.627	2468.539	2359.642	2240.099	2110.103	1970.101	1820.686	1662.738
X3-x4			4279.996	4271.248	4252.684	4222.584	4180.351	4125.949	4059.878	3982.976	3893.318	3791.083	3678.494	3554.797	3420.328	3275.431	3120.596	2956.319	2783.185
X4-x5			5106.132	5095.488	5072.836	5037.396	4989.212	4928.43	4855.248	4770.369	4673.268	4564.344	4444.893	4314.989	4175.172	4026.004	3868.116	3702.121	3528.646
X5-x6			5322.324	5309.196	5283.028	5243.956	5192.197	5128.04	5051.842	4964.021	4865.099	4755.638	4636.227	4507.54	4370.269	4225.128	4072.837	3914.11	3749.635
X6-x7			5101.132	5086.172	5058.276	5018.244	4966.415	4903.182	4829.003	4744.096	4649.677	4546.384	4434.302	4314.457	4187.62	4054.56	3915.998	3772.677	3625.292
X7-x8			4292.852	4277.956	4251.371	4214.23	4166.968	4110.042	4043.921	3968.705	3885.932	3796.224	3699.368	3596.477	3488.331	3375.649	3259.054	3139.243	3016.846
X8-x9			2970.956	2959.068	2937.848	2908.471	2871.414	2827.114	2775.967	2718.012	2654.753	2586.712	2513.533	2436.182	2355.37	2271.672	2185.507	2097.453	2008.005
X9-x10			1622.432	2416.674	2405.238	1588.932	1568.184	1543.311	1514.56	1481.944	1446.533	1408.653	1367.974	1325.089	1280.531	1234.64	1187.545	1139.622	1091.177
Delta(x)	(Cm3)																		
X1-X2			0.018201	0.000576	-0.00011	-0.00254	-0.00158	-0.02903	0.033583	0.00864	0.023989	0.027244	0.040608	0.051854	0.073981	0.092242	0.122122	0.154546	0.203161
X2-x3			0.003762	-0.02028	-0.02562	-0.02686	-0.02601	0.697131	-0.7461	-0.01716	0.005241	0.007591	0.022226	0.038233	0.058982	0.079794	0.107007	0.137996	0.174646
X3-x4			-0.00322	-0.0264	-0.02654	-0.02468	-0.02041	-0.07121	0.043579	-0.00315	0.022107	0.027525	0.045374	0.06447	0.08862	0.111986	0.140116	0.172342	0.207895
X4-x5			0.004701	-0.01314	-0.00629	0.001194	0.01122	-0.04339	0.09559	0.047804	0.077285	0.089759	0.114523	0.141554	0.172722	0.203164	0.239018	0.279929	0.323608
X5-x6			0.015093	0.001301	0.008509	0.015994	0.025298	-0.03466	0.145865	0.028465	0.085069	0.096584	0.118029	0.141755	0.168994	0.193895	0.22451	0.257388	0.291909
X6-x7			0.027134	0.017402	0.023342	0.028815	0.036844	-0.03158	0.120102	0.06184	0.07419	0.081876	0.094624	0.109615	0.124625	0.138803	0.15413	0.170931	0.185654
X7-x8			0.033444	0.029982	0.033145	0.035228	0.036099	-0.042	0.109721	0.043214	0.033812	0.033424	0.029583	0.027167	0.020505	0.012873	0.002686	-0.01126	-0.03061
X8-x9			0.02072	0.022834	0.012906	0.00131	-0.017	-0.11618	0.014213	-0.07003	-0.13409	-0.16082	-0.20674	-0.2596	-0.32321	-0.38521	-0.46485	-0.5564	-0.66004
X9-x10			-0.04028	-0.0054	-0.02476	-0.0693	-0.1135	-0.2518	-0.14643	-0.25687	-0.42736	-0.48862	-0.61206	-0.7454	-0.90084	-1.04847	-1.22376	-1.41337	-1.60418
Delta(t)	0.000139	(Sec)																	
Velocity	(mm/sec)																		
X1-X2			131.0461	4.145318	-0.77466	-18.3136	-11.3929	-209.01	241.7948	62.2046	172.721	196.1565	292.3787	373.3516	532.6654	664.1401	879.2765	1112.734	1462.761
X2-x3			27.08372	-146.042	-184.448	-193.422	-187.25	5019.342	-5371.94	-123.539	37.73166	54.65513	160.0237	275.278	424.6683	574.5167	770.4499	993.5683	1257.454
X3-x4			-23.1941	-190.072	-191.109	-177.715	-146.975	-512.703	313.7671	-22.6577	159.1685	198.1772	326.6959	464.1874	638.0658	806.2981	1008.837	1240.862	1496.845
X4-x5			33.8505	-94.5895	-45.2698	8.594454	80.78435	-312.437	688.25	344.1898	556.453	646.2679	824.563	1019.19	1243.602	1462.782	1720.926	2015.487	2329.975
X5-x6			108.668	9.365052	61.26396	115.1591	182.143	-249.587	1050.231	204.9472	612.4983	695.4017	849.8094	1020.635	1216.756	1396.046	1616.471	1853.193	2101.743
X6-x7			195.3649	125.2926	168.0597	207.466	265.274	-227.391	864.7367	445.2448	534.1711	589.5061	681.2902	789.2258	897.2984	999.3787	1109.738	1230.707	1336.709
X7-x8			240.7981	215.8675	238.6468	253.6431	259.9129	-302.4	789.9947	311.1417	243.4461	240.6525	212.9959	195.6043	147.634	92.68748	19.33586	-81.0426	-220.405
X8-x9			149.1853	164.4034	92.92278	9.431543	-122.435	-836.51	102.3334	-504.197	-965.427	-1157.91	-1488.56	-1869.11	-2327.09	-2773.54	-3346.89	-4006.05	-4752.27
X9-x10			-289.987	-38.9064	-178.27	-498.977	-817.194	-1812.94	-1054.28	-1849.49	-3076.98	-3518.09	-4406.86	-5366.86	-6486.02	-7549.01	-8811.08	-10176.3	-11550.1

Harekat			165-162	167-165	170-167	172-170	175-172	177-175	180-177	182-180	185-182	187-185	190-187	192-190	195-192	197-195	200-197	202-200	205-202	207-205	210-207
Area	(mm2)	New																			
X1-X2			598.5779	500.2644	411.0846	334.4236	272.1207	223.7841	187.1389	159.0278	136.6172	118.2196	103.7135	94.60866	93.05796	100.3372	115.8659	137.845	164.374	194.1061	226.1912
X2-x3			1497.521	1326.776	1152.935	979.2569	810.2555	651.8549	511.1393	394.9959	307.0932	244.817	200.3539	166.1153	139.7861	126.1588	133.1309	162.7478	209.4023	266.6511	330.5008
X3-x4			2601.894	2413.27	2218.317	2018.156	1814.297	1608.765	1404.208	1204.387	1014.628	842.2117	696.1023	584.0059	506.1272	452.7277	415.1645	402.0512	429.414	494.0994	580.2969
X4-x5			3348.34	3161.867	2969.923	2773.138	2572.247	2368.109	2161.626	1953.944	1746.555	1541.497	1341.694	1151.443	976.9662	826.6274	709.11	626.9634	574.6566	564.8893	616.5582
X5-x6			3580.077	3406.074	3228.235	3047.087	2863.16	2676.99	2489.056	2299.86	2109.95	1919.975	1730.743	1543.347	1359.328	1180.933	1011.486	855.8353	720.6739	613.8763	547.0787
X6-x7			3474.492	3320.873	3164.977	3007.301	2848.282	2688.311	2527.743	2366.882	2206.019	2045.452	1885.479	1726.44	1568.775	1413.087	1260.227	1111.424	968.5375	834.4338	713.7467
X7-x8			2892.436	2766.524	2639.554	2511.986	2384.18	2256.397	2128.934	2002.002	1875.794	1750.492	1626.241	1503.176	1381.45	1261.273	1142.901	1026.687	913.176	803.224	698.1689
X8-x9			1917.602	1826.619	1735.357	1644.226	1553.483	1463.247	1373.765	1285.175	1197.604	1111.17	1025.959	942.0254	859.4357	778.2779	698.6415	620.6336	567.6171	493.528	398.8046
X9-x10			1042.457	993.643	944.8537	896.4316	848.5124	801.037	754.1987	708.0654	662.701	618.1663	574.4995	531.7221	489.8596	448.9472	409.0121	370.0847	332.2226	295.5189	260.1076
Delta(x)	(Cm3)																				
X1-X2			0.2583	0.33888	0.431718	0.574173	0.706708	0.886579	1.042763	1.183867	1.287195	1.335796	1.266773	1.031	0.590363	0.043404	-0.46668	-0.84898	-1.11261	-0.92669	-1.58652
X2-x3			0.217915	0.270147	0.331013	0.413535	0.504841	0.629412	0.773605	0.933711	1.056278	1.079428	0.910855	0.490372	-0.29439	-1.46305	-2.54642	-3.10315	-3.19254	-2.48949	-3.21366
X3-x4			0.246021	0.288485	0.333798	0.384139	0.435122	0.490478	0.54677	0.598823	0.638179	0.644903	0.580485	0.393888	0.03778	-0.50443	-1.20261	-1.95488	-2.48666	-2.1239	-3.02171
X4-x5			0.370785	0.418876	0.471465	0.526018	0.579057	0.632009	0.68307	0.726941	0.757784	0.7646	0.733679	0.638277	0.440147	0.083827	-0.46946	-1.20777	-2.04593	-1.90826	-3.6351
X5-x6			0.32777	0.361485	0.396425	0.428027	0.454347	0.473538	0.483446	0.478449	0.451444	0.395189	0.299303	0.150143	-0.07021	-0.37597	-0.78628	-1.29047	-1.83207	-1.51698	-3.01515
X6-x7			0.199571	0.207657	0.212995	0.210869	0.198426	0.174547	0.137128	0.08116	0.004628	-0.09714	-0.22023	-0.36276	-0.50907	-0.62962	-0.66778	-0.54966	-0.19532	0.885891	0.660249
X7-x8			-0.05701	-0.08816	-0.13047	-0.18377	-0.25107	-0.32433	-0.4128	-0.50836	-0.59949	-0.66999	-0.69023	-0.61971	-0.40616	-0.02733	0.508519	1.144459	1.78891	2.79651	2.237977
X8-x9			-0.77749	-0.90571	-1.04626	-1.19401	-1.33981	-1.46675	-1.55449	-1.56947	-1.47462	-1.23813	-0.85352	-0.33533	0.269403	0.919912	1.585268	2.251624	2.787728	3.721031	3.591428
X9-x10			-1.78559	-1.94094	-2.05134	-2.11541	-2.03448	-1.89551	-1.63694	-1.28294	-0.86624	-0.41567	0.048652	0.519516	0.999021	1.503396	2.015095	2.532403	3.041375	-4.51599	12.72111
Delta(t)	0.000139	(Sec)																			
Velocity	(mm/sec)																				
X1-X2			1859.76	2439.934	3108.371	4134.047	5088.3	6383.367	7507.891	8523.839	9267.807	9617.733	9120.762	7423.197	4250.615	312.5066	-3360.07	-6112.67	-8010.78	-6672.18	-11422.9
X2-x3			1568.986	1945.055	2383.293	2977.451	3634.853	4531.768	5569.953	6722.722	7605.198	7771.88	6558.159	3530.678	-2119.58	-10533.9	-18334.2	-22342.6	-22986.3	-17924.3	-23138.4
X3-x4			1771.349	2077.094	2403.347	2765.8	3132.879	3531.445	3936.744	4311.523	4594.888	4643.298	4179.495	2835.993	272.0164	-3631.88	-8658.76	-14075.1	-17903.9	-15292.1	-21756.3
X4-x5			2669.649	3015.908	3394.547	3787.329	4169.209	4550.464	4918.102	5233.975	5456.048	5505.118	5282.491	4595.592	3169.058	603.5538	-3380.11	-8695.92	-14730.7	-13739.5	-26172.7
X5-x6			2359.945	2602.693	2854.259	3081.797	3271.297	3409.477	3480.814	3444.836	3250.394	2845.358	2154.985	1081.028	-505.502	-2706.97	-5661.2	-9291.38	-13190.9	-10922.2	-21709.1
X6-x7			1436.91	1495.132	1533.566	1518.257	1428.664	1256.737	987.3182	584.3512	33.31887	-699.385	-1585.62	-2611.84	-3665.33	-4533.26	-4808.02	-3957.56	-1406.33	6378.414	4753.79
X7-x8			-410.464	-634.783	-939.371	-1323.17	-1807.69	-2335.21	-2972.19	-3660.18	-4316.34	-4823.95	-4969.66	-4461.89	-2924.32	-196.77	3661.334	8240.107	12880.15	20134.87	16113.44
X8-x9			-5597.95	-6521.15	-7533.06	-8596.86	-9646.63	-10560.6	-11192.3	-11300.2	-10617.2	-8914.52	-6145.34	-2414.41	1939.703	6623.367	11413.93	16211.69	20071.64	26791.42	25858.28
X9-x10			-12856.2	-13974.8	-14769.6	-15230.9	-14648.3	-13647.7	-11786	-9237.13	-6236.89	-2992.79	350.296	3740.513	7192.954	10824.45	14508.69	18233.3	21897.9	-32515.1	91591.99

Table B.2 : Transfer velocities for left recess modeled rotor

Harekat			122.5-120	125-122.5	127.5-125	130-127.5	132.5-130	135-132.5	137.5-135	140-137.5	142.5-140	145-142.5	147-145	150-147	152-150	155-152	157-155	160-157	162-160
Area	(mm2)	New																	
X1-X2			1628.392	1618.98	1608.002	1590.602	1566.499	1535.387	1496.93	1453.426	1399.527	1335.066	1265.054	1187.003	1101.273	1008.48	909.7615	806.7973	702.0093
X2-x3			2978.716	2970.296	2955.466	2930.866	2896.264	2851.452	2796.209	2732.137	2655.633	2566.627	2468.539	2359.642	2240.099	2110.103	1970.101	1820.686	1662.738
X3-x4			4137.996	4271.248	4252.684	4222.584	4180.351	4125.949	4059.878	3982.976	3893.318	3791.083	3678.494	3554.797	3420.328	3275.431	3120.596	2956.319	2783.185
X4-x5			4865.732	5095.488	5072.836	5037.396	4989.212	4928.43	4855.248	4770.369	4673.268	4564.344	4444.893	4314.989	4175.172	4026.004	3868.116	3702.121	3528.646
X5-x6			5221.524	5309.196	5283.028	5243.956	5192.197	5128.04	5051.842	4964.021	4865.099	4755.638	4636.227	4507.54	4370.269	4225.128	4072.837	3914.11	3749.635
X6-x7			5101.532	5086.172	5058.276	5018.244	4966.415	4903.182	4829.003	4744.096	4649.677	4546.384	4434.302	4314.457	4187.62	4054.56	3915.998	3772.677	3625.292
X7-x8			4383.652	4277.956	4251.371	4214.23	4166.968	4110.042	4043.921	3968.705	3885.932	3796.224	3699.368	3596.477	3488.331	3375.649	3259.054	3139.243	3016.846
X8-x9			3210.956	2959.068	2937.848	2908.471	2871.414	2827.114	2775.967	2718.012	2654.753	2586.712	2513.533	2436.182	2355.37	2271.672	2185.507	2097.453	2008.005
X9-x10			1774.432	2416.674	2405.238	1588.932	1568.184	1543.311	1514.56	1481.944	1446.533	1408.653	1367.974	1325.089	1280.531	1234.64	1187.545	1139.622	1091.177
Delta(x)	(Cm3)																		
X1-X2			0.018201	0.000576	-0.00011	-0.00254	-0.00158	-0.02903	0.033583	0.00864	0.023989	0.027244	0.040608	0.051854	0.073981	0.092242	0.122122	0.154546	0.203161
X2-x3			0.003762	-0.02028	-0.02562	-0.02686	-0.02601	0.697131	-0.7461	-0.01716	0.005241	0.007591	0.022226	0.038233	0.058982	0.079794	0.107007	0.137996	0.174646
X3-x4			-0.00427	-0.02866	-0.03033	-0.03003	-0.02742	-0.07846	0.031703	-0.01569	0.007577	0.010718	0.026091	0.042403	0.063467	0.083981	0.108303	0.136116	0.166596
X4-x5			0.001917	-0.02029	-0.01828	-0.01576	-0.01096	-0.06635	0.058056	0.008208	0.031533	0.036998	0.054204	0.072841	0.094839	0.11705	0.142013	0.170589	0.20049
X5-x6			0.012689	-0.00528	-0.00253	0.000375	0.004865	-0.05582	0.111277	-0.00802	0.04293	0.048029	0.062581	0.078685	0.09765	0.115218	0.136174	0.158228	0.180817
X6-x7			0.026489	0.015801	0.020655	0.025012	0.031866	-0.03674	0.111671	0.052945	0.063917	0.070042	0.081116	0.094262	0.107277	0.1197	0.132724	0.146961	0.158882
X7-x8			0.0335	0.031885	0.036342	0.039757	0.042031	-0.03585	0.119789	0.053847	0.046104	0.047596	0.045774	0.045585	0.04133	0.035818	0.028407	0.017551	0.001559
X8-x9			0.023549	0.034626	0.032733	0.02943	0.019889	-0.07787	0.077068	-0.00349	-0.05697	-0.07168	-0.10462	-0.14307	-0.19102	-0.23909	-0.30046	-0.37162	-0.45289
X9-x10			-0.02855	0.009677	0.000534	-0.01554	-0.04294	-0.1785	-0.0261	-0.12941	-0.27955	-0.31767	-0.41607	-0.52164	-0.6469	-0.76767	-0.90779	-1.05818	-1.20604
Delta(t)	0.000139	(Sec)																	
Velocity	(mm/sec)																		
X1-X2			131.0461	4.145318	-0.77466	-18.3136	-11.3929	-209.01	241.7948	62.2046	172.721	196.1565	292.3787	373.3516	532.6654	664.1401	879.2765	1112.734	1462.761
X2-x3			27.08372	-146.042	-184.448	-193.422	-187.25	5019.342	-5371.94	-123.539	37.73166	54.65513	160.0237	275.278	424.6683	574.5167	770.4499	993.5683	1257.454
X3-x4			-30.7478	-206.327	-218.361	-216.252	-197.394	-564.931	228.2586	-112.998	54.55311	77.16958	187.8535	305.3014	456.9593	604.6665	779.7841	980.0332	1199.495
X4-x5			13.80101	-146.088	-131.618	-113.501	-78.8886	-477.698	418.0017	59.09545	227.0353	266.3852	390.2699	524.4544	682.8385	842.7625	1022.491	1228.244	1443.525
X5-x6			91.35733	-38.0258	-18.235	2.701989	35.0291	-401.877	801.1928	-57.7458	309.0971	345.8103	450.5813	566.5324	703.0827	829.5709	980.4522	1139.242	1301.881
X6-x7			190.7211	113.7665	148.7137	180.0853	229.4386	-264.501	804.0339	381.2008	460.2044	504.3034	584.0356	678.6863	772.3938	861.8394	955.6128	1058.122	1143.952
X7-x8			241.1968	229.5712	261.6647	286.2476	302.6234	-258.128	862.4822	387.6984	331.9503	342.6918	329.5717	328.2113	297.5775	257.8888	204.5294	126.3656	11.22822
X8-x9			169.5502	249.3101	235.6767	211.8987	143.1979	-560.674	554.8918	-25.1217	-410.216	-516.116	-753.246	-1030.11	-1375.37	-1721.46	-2163.33	-2675.65	-3260.81
X9-x10			-205.582	69.67718	3.844898	-111.899	-309.191	-1285.19	-187.94	-931.776	-2012.74	-2287.19	-2995.74	-3755.82	-4657.65	-5527.21	-6536.11	-7618.87	-8683.5

Harekat			165-162	167-165	170-167	172-170	175-172	177-175	180-177	182-180	185-182	187-185	190-187	192-190	195-192	197-195	200-197	202-200	205-202	207-205	210-207
Area	(mm2)	New																			
X1-X2			598.5779	500.2644	411.0846	334.4236	272.1207	223.7841	187.1389	159.0278	136.6172	118.2196	103.7135	94.60866	93.05796	100.3372	115.8659	137.845	164.374	194.1061	226.1912
X2-x3			1497.521	1326.776	1152.935	979.2569	810.2555	651.8549	511.1393	394.9959	307.0932	244.817	200.3539	166.1153	139.7861	126.1588	133.1309	162.7478	209.4023	266.6511	330.5008
X3-x4			2601.894	2413.27	2218.317	2018.156	1814.297	1608.765	1404.208	1204.387	1014.628	842.2117	696.1023	584.0059	506.1272	452.7277	415.1645	402.0512	429.414	494.0994	580.2969
X4-x5			3348.34	3161.867	2969.923	2773.138	2572.247	2368.109	2161.626	1953.944	1746.555	1541.497	1341.694	1151.443	976.9662	826.6274	709.11	626.9634	574.6566	564.8893	616.5582
X5-x6			3580.077	3406.074	3228.235	3047.087	2863.16	2676.99	2489.056	2299.86	2109.95	1919.975	1730.743	1543.347	1359.328	1180.933	1011.486	855.8353	720.6739	613.8763	547.0787
X6-x7			3474.492	3320.873	3164.977	3007.301	2848.282	2688.311	2527.743	2366.882	2206.019	2045.452	1885.479	1726.44	1568.775	1413.087	1260.227	1111.424	968.5375	834.4338	713.7467
X7-x8			2892.436	2766.524	2639.554	2511.986	2384.18	2256.397	2128.934	2002.002	1875.794	1750.492	1626.241	1503.176	1381.45	1261.273	1142.901	1026.687	913.176	803.224	698.1689
X8-x9			1917.602	1826.619	1735.357	1644.226	1553.483	1463.247	1373.765	1285.175	1197.604	1111.17	1025.959	942.0254	859.4357	778.2779	698.6415	620.6336	567.6171	493.528	398.8046
X9-x10			1042.457	993.643	944.8537	896.4316	848.5124	801.037	754.1987	708.0654	662.701	618.1663	574.4995	531.7221	489.8596	448.9472	409.0121	370.0847	332.2226	295.5189	260.1076
Delta(x)	(Cm3)																				
X1-X2			0.2583	0.33888	0.431718	0.574173	0.706708	0.886579	1.042763	1.183867	1.287195	1.335796	1.266773	1.031	0.590363	0.043404	-0.46668	-0.84898	-1.11261	-0.92669	-1.58652
X2-x3			0.217915	0.270147	0.331013	0.413535	0.504841	0.629412	0.773605	0.933711	1.056278	1.079428	0.910855	0.490372	-0.29439	-1.46305	-2.54642	-3.10315	-3.19254	-2.48949	-3.21366
X3-x4			0.198735	0.234188	0.271031	0.311107	0.349536	0.389243	0.425621	0.452333	0.459144	0.425201	0.313041	0.078608	-0.31426	-0.87274	-1.56332	-2.26881	-2.71042	-2.3263	-2.98847
X4-x5			0.231903	0.262241	0.294265	0.325133	0.35089	0.372068	0.385613	0.38566	0.364674	0.310904	0.209228	0.033877	-0.24918	-0.6786	-1.26767	-1.96867	-2.67792	-2.57737	-3.51683
X5-x6			0.203226	0.222067	0.240116	0.25273	0.257802	0.253058	0.235755	0.200437	0.139435	0.045925	-0.09052	-0.28222	-0.54524	-0.88768	-1.32283	-1.82494	-2.31526	-2.10734	-2.88736
X6-x7			0.169671	0.17434	0.175848	0.169485	0.152392	0.123392	0.080299	0.018218	-0.0649	-0.17352	-0.3036	-0.45281	-0.60498	-0.72926	-0.76812	-0.64555	-0.27909	0.784695	0.683071
X7-x8			-0.02109	-0.04817	-0.08593	-0.13423	-0.19607	-0.26339	-0.34533	-0.43395	-0.51772	-0.58074	-0.59357	-0.51628	-0.29725	0.084303	0.619159	1.248267	1.877759	2.901638	2.214646
X8-x9			-0.54531	-0.64612	-0.7559	-0.86961	-0.97809	-1.06397	-1.10636	-1.07267	-0.92571	-0.63551	-0.19686	0.37199	1.019652	1.695245	2.360965	2.987582	3.400326	4.454305	3.416374
X9-x10			-1.3395	-1.44251	-1.49436	-1.49397	-1.3428	-1.12704	-0.78439	-0.34115	0.169812	0.715697	1.273463	1.828341	2.373799	2.907222	3.398967	3.821462	4.134544	-3.23697	12.44078
Delta(t)	0.000139	(Sec)																			
Velocity	(mm/sec)																				
X1-X2			1859.76	2439.934	3108.371	4134.047	5088.3	6383.367	7507.891	8523.839	9267.807	9617.733	9120.762	7423.197	4250.615	312.5066	-3360.07	-6112.67	-8010.78	-6672.18	-11422.9
X2-x3			1568.986	1945.055	2383.293	2977.451	3634.853	4531.768	5569.953	6722.722	7605.198	7771.88	6558.159	3530.678	-2119.58	-10533.9	-18334.2	-22342.6	-22986.3	-17924.3	-23138.4
X3-x4			1430.89	1686.157	1951.424	2239.97	2516.656	2802.552	3064.47	3256.8	3305.836	3061.445	2253.895	565.9746	-2262.67	-6283.75	-11255.9	-16335.4	-19515	-16749.3	-21517
X4-x5			1669.702	1888.135	2118.711	2340.956	2526.406	2678.891	2776.415	2776.751	2625.65	2238.511	1506.444	243.9167	-1794.09	-4885.93	-9127.23	-14174.5	-19281	-18557.1	-25321.2
X5-x6			1463.227	1598.88	1728.834	1819.654	1856.174	1822.016	1697.436	1443.146	1003.932	330.6611	-651.74	-2031.95	-3925.72	-6391.29	-9524.39	-13139.6	-16669.9	-15172.9	-20789
X6-x7			1221.629	1255.246	1266.105	1220.291	1097.223	888.4208	578.1562	131.1703	-467.305	-1249.36	-2185.91	-3260.23	-4355.83	-5250.66	-5530.46	-4647.99	-2009.47	5649.803	4918.113
X7-x8			-151.86	-346.83	-618.67	-966.447	-1411.73	-1896.39	-2486.38	-3124.41	-3727.59	-4181.31	-4273.68	-3717.19	-2140.18	606.984	4457.947	8987.519	13519.87	20891.79	15945.45
X8-x9			-3926.24	-4652.05	-5442.48	-6261.22	-7042.24	-7660.57	-7965.79	-7723.24	-6665.11	-4575.68	-1417.36	2678.326	7341.493	12205.77	16998.95	21510.59	24482.35	32071	24597.89
X9-x10			-9644.41	-10386.1	-10759.4	-10756.5	-9668.14	-8114.72	-5647.61	-2456.3	1222.646	5153.017	9168.933	13164.05	17091.35	20932	24472.56	27514.52	29768.72	-23306.2	89573.64

Table B.3 : Transfer velocities for right recess modeled rotor

Harekat			122.5-120	125-122.5	127.5-125	130-127.5	132.5-130	135-132.5	137.5-135	140-137.5	142.5-140	145-142.5	147-145	150-147
Area	(mm2)	New												
X1-X2			1912.3916	1902.98	1892.002	1874.602	1850.49871	1819.38671	1780.92988	1737.42588	1683.526782	1619.065982	1549.05377	1471.00297
X2-x3			3459.516	3451.096	3436.266	3411.666	3377.06379	3332.25203	3277.009274	3212.937034	3136.432856	3047.427216	2949.339151	2840.441991
X3-x4			4481.596	4472.848	4454.284	4424.184	4381.95087	4327.54851	4261.478489	4184.575649	4094.918148	3992.68278	3880.094381	3756.396949
X4-x5			5105.332	5094.688	5072.036	5036.596	4988.412	4927.62983	4854.447663	4769.569035	4672.467652	4563.544212	4444.0932	4314.18904
X5-x6			5140.7236	5127.5956	5101.428	5062.356	5010.59747	4946.44033	4870.241988	4782.420728	4683.499308	4574.038148	4454.62684	4325.94
X6-x7			4621.132	4606.172	4578.276	4538.2436	4486.41468	4423.18204	4349.00252	4264.09556	4169.676952	4066.383792	3954.302381	3834.457141
X7-x8			3988.852	3973.956	3947.3708	3910.23	3862.96772	3806.04216	3739.920592	3664.70536	3581.931509	3492.224109	3395.367506	3292.477306
X8-x9			2970.956	2959.068	2937.848	2908.4708	2871.4139	2827.11435	2775.967008	2718.011752	2654.75336	2586.71244	2513.53277	2436.18169
X9-x10			1622.432	2416.674	2405.238	1588.932	1568.18412	1543.31076	1514.560057	1481.944217	1446.532936	1408.653056	1367.974279	1325.089239
Delta(x)	(Cm3)													
X1-X2			0.01752683	0.006568981	0.007358088	0.009829915	0.01436437	-0.00709104	0.053895129	0.035634567	0.053073067	0.0624461	0.076891729	0.094139994
X2-x3			0.00748209	-0.005208114	-0.00601685	0.00196005	0.01045931	0.63232837	-0.582864095	0.044199725	0.072608063	0.087414022	0.107508663	0.136145389
X3-x4			6.418E-05	-0.015354221	-0.01428644	-0.00504478	0.00473652	-0.04070169	0.080393898	0.040285793	0.071083046	0.086343859	0.106901133	0.136691986
X4-x5			0.00534456	-0.009205805	-0.00594343	0.004982879	0.01617703	-0.03583549	0.101555747	0.056659653	0.087521412	0.104282051	0.125316957	0.15693402
X5-x6			0.014988	0.002309226	0.003596471	0.012798347	0.02128125	-0.03837613	0.140272747	0.020722055	0.078168753	0.09163219	0.106433617	0.13239372
X6-x7			0.02691099	-0.003096912	0.027820647	0.013840556	0.01717277	-0.07499935	0.108771712	0.026388014	0.033634865	0.017714724	0.058255321	0.049302432
X7-x8			0.03231289	0.025866697	0.017517942	0.016121123	0.01029744	-0.07216549	0.066993701	-0.004744027	-0.023010631	-0.0293992	-0.049947529	-0.060377119
X8-x9			0.01940607	0.022333658	0.004616328	-0.00650129	-0.02725307	-0.12390592	-0.006174457	-0.08851023	-0.155507221	-0.18239115	-0.238294425	-0.291966524
X9-x10			-0.0402759	-0.003311964	-0.02685117	-0.06930242	-0.11349912	-0.24853958	-0.149697381	-0.256874071	-0.427358249	-0.48515623	-0.615524536	-0.745397377
Delta(t)	0.000139	(Sec)												
Velocity	(mm/sec)													
X1-X2			126.193185	47.29666009	52.97823488	70.77538546	103.423431	-51.0554939	388.0449283	256.5688846	382.1260801	449.6119219	553.6204495	677.8079555
X2-x3			53.8710589	-37.49842112	-43.3212929	14.11235739	75.3070134	4552.76423	-4196.621483	318.2380235	522.7780558	629.3809619	774.0623747	980.2468021
X3-x4			0.46209334	-110.5503944	-102.86238	-36.3223874	34.1029577	-293.052173	578.8360691	290.0577092	511.7979337	621.6757817	769.6881604	984.1823013
X4-x5			38.4808303	-66.28179459	-42.7927261	35.87673103	116.474644	-258.015532	731.2013817	407.9494996	630.1541667	750.8307636	902.2820935	1129.924941
X5-x6			107.913573	16.626426	25.89459437	92.14809722	153.225035	-276.308105	1009.963781	149.1987979	562.815019	659.7517655	766.3220417	953.234781
X6-x7			193.759123	-22.29776676	200.3086566	99.65200305	123.643959	-539.995289	783.1563255	189.9936989	242.1710293	127.5460162	419.4383127	354.9775074
X7-x8			232.652803	186.2402181	126.1291815	116.0720822	74.1415887	-519.591543	482.3546482	-34.15699409	-165.6765433	-211.674222	-359.622207	-434.7152544
X8-x9			139.7237	160.8023411	33.23755878	-46.8093233	-196.222116	-892.122594	-44.45609193	-637.2736526	-1119.651993	-1313.21631	-1715.71986	-2102.15897
X9-x10			-289.98661	-23.84614055	-193.328449	-498.977417	-817.193658	-1789.48499	-1077.821146	-1849.49331	-3076.97939	-3493.12482	-4431.776657	-5366.861114

Harekat	152-150	155-152	157-155	160-157	162-160	165-162	167-165	170-167	172-170	175-172	177-175	180-177
Area												
X1-X2	1385.272936	1292.48004	1193.761524	1090.797336	986.0092612	882.5779012	784.264372	695.084616	618.423644	556.120664	507.7841288	471.1389088
X2-x3	2720.899184	2590.903392	2450.900686	2301.486478	2143.538444	1978.320804	1807.57609	1633.73517	1460.05686	1291.055468	1132.654908	991.9393
X3-x4	3621.927846	3477.031462	3322.196265	3157.918649	2984.784896	2803.494416	2614.870412	2419.917292	2219.756322	2015.896602	1810.364788	1605.807708
X4-x5	4174.372461	4025.204101	3867.31602	3701.3207	3527.845759	3347.539639	3161.067389	2969.122789	2772.338188	2571.447376	2367.309111	2160.826323
X5-x6	4188.66937	4043.52795	3891.23748	3732.50974	3568.03464	3398.47744	3224.473794	3046.634554	2865.487412	2681.560337	2495.390313	2307.456188
X6-x7	3707.619636	3574.559917	3435.997737	3292.676656	3145.2922	2994.49228	2840.872905	2684.977177	2527.300712	2368.28224	2208.31118	2047.74258
X7-x8	3184.33054	3071.64866	2955.05354	2835.24302	2712.846091	2588.435771	2462.523796	2335.553716	2207.986468	2080.17978	1952.396512	1824.93364
X8-x9	2355.370136	2271.672444	2185.507492	2097.453184	2008.005398	1917.60247	1826.619494	1735.357222	1644.2256	1553.483028	1463.246608	1373.76466
X9-x10	1280.530955	1234.640115	1187.544524	1139.622128	1091.176755	1042.456591	993.6430012	944.8537212	896.43164	848.512396	801.0370312	754.1986752
Delta(x)												
X1-X2	0.119605822	0.1445812	0.174539375	0.212490431	0.261217509	0.317186604	0.380494842	0.455642276	0.548825888	0.629691691	0.706737812	0.775270661
X2-x3	0.168070584	0.201212899	0.236679933	0.285048	0.338147264	0.403430457	0.46877229	0.555723574	0.658905401	0.77732332	0.899500781	1.046847961
X3-x4	0.169771716	0.203889608	0.237123946	0.284244197	0.33341259	0.391085368	0.444113401	0.514510302	0.589884386	0.676504998	0.75597828	0.862056241
X4-x5	0.190158473	0.225598433	0.257616061	0.30442136	0.351192439	0.405960068	0.449957898	0.511189683	0.571061326	0.63605926	0.684465523	0.749800329
X5-x6	0.158977168	0.186867612	0.210058876	0.245682729	0.279564412	0.319000874	0.343293477	0.381464058	0.411721247	0.442064972	0.447092664	0.459241075
X6-x7	0.056785836	0.045298317	0.090221728	0.078145159	0.081740189	0.059738269	0.09870728	0.063408776	0.039872517	-0.02807618	-0.025253213	-0.131366877
X7-x8	-0.079655988	-0.09512515	-0.12757922	-0.155232708	-0.194184031	-0.239183432	-0.304283317	-0.37277951	-0.461378606	-0.565062934	-0.694880922	-0.833905992
X8-x9	-0.359924666	-0.42238604	-0.51389247	-0.607722832	-0.717578698	-0.838380547	-0.981378435	-1.126913177	-1.284117171	-1.436923491	-1.581935603	-1.678973163
X9-x10	-0.900836447	-1.0450139	-1.22718891	-1.413371157	-1.604181267	-1.782515595	-1.94396401	-2.051339607	-2.11540947	-2.032566017	-1.89737981	-1.636937629
Delta(t)												
Velocity												
X1-X2	861.1619196	1040.984643	1256.683498	1529.931102	1880.766065	2283.743552	2739.562859	3280.624386	3951.546392	4533.780178	5088.512245	5581.948757
X2-x3	1210.108202	1448.73287	1704.09552	2052.345604	2434.660297	2904.699292	3375.160489	4001.209735	4744.118887	5596.727901	6476.405625	7537.305321
X3-x4	1222.356352	1468.005177	1707.292415	2046.558215	2400.570649	2815.814652	3197.616486	3704.474174	4247.167579	4870.835985	5443.043619	6206.804933
X4-x5	1369.141005	1624.308717	1854.835642	2191.833794	2528.585564	2922.912491	3239.696866	3680.565718	4111.641547	4579.62667	4928.151769	5398.562365
X5-x6	1144.635611	1345.446804	1512.423908	1768.915646	2012.863764	2296.806295	2471.713031	2746.541215	2964.392982	3182.867802	3219.06718	3306.535737
X6-x7	408.8580208	326.1478822	649.5964415	562.6451451	588.5293626	430.1155368	710.6924173	456.5431889	287.0821217	-202.1484947	-181.8231305	-945.8415122
X7-x8	-573.5231148	-684.901053	-918.570365	-1117.675496	-1398.125021	-1722.120713	-2190.839882	-2684.012472	-3321.925964	-4068.453122	-5003.142641	-6004.123142
X8-x9	-2591.457592	-3041.17947	-3700.0258	-4375.604388	-5166.566623	-6036.33994	-7065.924733	-8113.774876	-9245.643632	-10345.84913	-11389.93634	-12088.60677
X9-x10	-6486.022416	-7524.1001	-8835.76012	-10176.27233	-11550.10512	-12834.11228	-13996.54087	-14769.64517	-15230.94818	-14634.47532	-13661.13463	-11785.95093

Harekat	182-180	185-182	187-185	190-187	192-190	195-192	197-195	200-197	202-200	205-202	207-205	210-207
Area												
X1-X2	443.0278166	420.6172269	402.2195843	387.713494	378.6086642	377.0579642	384.3371844	399.8659244	421.8449953	448.3739909	478.1061339	510.19122
X2-x3	875.795885	787.8932386	725.6169685	681.1539029	646.9152716	620.5860624	606.9587928	613.930854	643.547801	690.202317	747.4510785	811.30083
X3-x4	1405.986982	1216.228424	1043.81175	897.702324	785.60594	707.727172	654.3277414	616.7644774	603.6511689	631.0140205	695.6994191	781.8969
X4-x5	1953.143725	1745.754805	1540.697076	1340.894435	1150.64253	976.1662027	825.8273656	708.3100336	626.1634204	573.8566124	564.0893432	615.75821
X5-x6	2118.259735	1928.349935	1738.37456	1549.14348	1361.747264	1177.727936	999.3332515	829.8861236	674.2353248	539.0738936	432.2763208	365.47869
X6-x7	1886.881735	1726.019199	1565.452176	1405.479272	1246.440416	1088.774535	933.08686	780.2267568	631.423926	488.53753	354.4338154	233.74668
X7-x8	1698.002424	1571.794312	1446.491525	1322.241357	1199.17568	1077.450304	957.272798	838.9013816	722.6867328	609.1759669	499.2239697	394.16893
X8-x9	1285.17492	1197.603513	1111.170445	1025.958772	942.025388	859.435696	778.27794	698.641504	620.6336082	567.6171378	493.5280416	398.80464
X9-x10	708.0654068	662.7010068	618.1663	574.49946	531.7221076	489.8595876	448.9471764	409.0120524	370.084716	332.2226488	295.51892	260.1076
Delta(x)												
X1-X2	0.823193433	0.857192327	0.845752249	0.819032748	0.743953113	0.627626011	0.436747992	0.239286526	0.02178569	-0.185641	-0.174151986	-0.7411879
X2-x3	1.182531367	1.294403428	1.316850198	1.300949084	1.201686543	1.035392187	0.718771711	0.369769103	-0.043460861	-0.42762554	-0.395423328	-1.3990287
X3-x4	0.967721641	1.084588877	1.15118452	1.201690969	1.142191437	0.960424033	0.553678091	0.070428836	-0.544254071	-1.11794237	-1.006855469	-2.3320254
X4-x5	0.803513563	0.855711368	0.856366973	0.851351576	0.7738397	0.613676763	0.233758813	-0.291464428	-1.039102865	-1.87755574	-1.790164683	-3.6662737
X5-x6	0.449137957	0.423195103	0.337712041	0.232914826	0.055993187	-0.194173742	-0.600969455	-1.110707692	-1.796119697	-2.57302343	-2.381326274	-4.4687533
X6-x7	-0.236565825	-0.415879808	-0.513508162	-0.774782265	-1.03702722	-1.392447649	-1.528806291	-1.773187568	-1.690888284	-1.25001384	1.26273429	2.3147396
X7-x8	-0.992094913	-1.147032472	-1.299474547	-1.381090513	-1.35714907	-1.140737129	-0.699597609	0.018079101	0.965757645	2.095700367	3.730414704	4.1489862
X8-x9	-1.707464555	-1.624860354	-1.407713976	-1.035926643	-0.53181303	0.062701876	0.702819002	1.369796499	2.04719103	2.624579732	3.50966106	3.6400545
X9-x10	-1.282935082	-0.865606597	-0.416279892	0.048652217	0.519515709	1.000439907	1.501976789	2.015095173	2.532402819	3.049549007	-4.524737414	12.72111
Delta(t)												
Velocity												
X1-X2	5926.992716	6171.784753	6089.416192	5897.035783	5356.46241	4518.90728	3144.58554	1722.86299	156.8569675	-1336.61522	-1253.894301	-5336.5525
X2-x3	8514.22584	9319.70468	9481.321424	9366.833403	8652.143113	7454.823749	5175.15632	2662.337542	-312.918197	-3078.90388	-2847.04796	-10073.007
X3-x4	6967.595815	7809.039916	8288.528544	8652.174976	8223.778349	6915.053041	3986.482253	507.0876194	-3918.629308	-8049.18506	-7249.359379	-16790.583
X4-x5	5785.297656	6161.121846	6165.842205	6129.731348	5571.645844	4418.472695	1683.063455	-2098.543883	-7481.540631	-13518.4013	-12889.18572	-26397.171
X5-x6	3233.793291	3047.004745	2431.526695	1676.98675	403.1509446	-1398.050941	-4326.980078	-7997.095381	-12932.06182	-18525.7687	-17145.54917	-32175.024
X6-x7	-1703.273938	-2994.334614	-3697.258767	-5578.432306	-7466.59599	-10025.62308	-11007.4053	-12766.95049	-12174.39565	-9000.09963	9091.686888	16666.125
X7-x8	-7143.083374	-8258.633802	-9356.216737	-9943.851694	-9771.4733	-8213.30733	-5037.102786	130.1695264	6953.455045	15089.04264	26858.98587	29872.701
X8-x9	-12293.7448	-11698.99455	-10135.54063	-7458.671827	-3829.05379	451.4535062	5060.296815	9862.534791	14739.77542	18896.97407	25269.55963	26208.393
X9-x10	-9237.132593	-6232.367497	-2997.215226	350.2959614	3740.513102	7203.167332	10814.23288	14508.68524	18233.3003	21956.75285	-32578.10938	91591.993

CURRICULUM VITAE

Name Surname: Amin Farzadi

Place and Date of Birth: Iran, Tabriz, 1987

E-Mail: amin.farzadi@ymail.com

EDUCATION:

B.Sc.: Mechanical Engineering, Solid Design, Tabriz Azad University, Iran.

M.Sc.: Mechanical Engineering, Automotive program, Istanbul Technical University, Istanbul, Turkey.